The Computation of Winding Eddy Losses in Power Transformers Using Analytical and Numerical Methods

Mluleki Cyril Hlatshwayo

A dissertation submitted to the Faculty of Engineering and the Built Environment, University of the Witwatersrand, in fulfilment of the requirements for the degree of Master of Science in Engineering.

Johannesburg, 2013

Declaration

I declare that this dissertation is my own unaided work except where otherwise acknowledged. It is being submitted for the degree of Master of Science in Engineering in the University of the Witwatersrand, Johannesburg. It has not been submitted before for any degree or examination in any other university.

Signed this…… day of …..………..2013

…………………………………

Mluleki Cyril Hlatshwayo

Abstract

This dissertation presents the implementation of analytical and numeral methods in computing the winding eddy losses of power transformers. It is appreciated that the computation of any component of stray losses of a transformer is intricate and involves a multitude of variables. The eddy current losses of a single conductor are treated using the rectangular and cylindrical coordinates of the differential form of Maxwell’s equations. The governing equations have limited use when the conductor thickness is increased; this is observed when thicknesses exceed 5mm. The analytical method, known as Rabins’ method is implemented in Mathematica to evaluate local flux density quantities. The analytical method is compared to the two-dimensional finite element method (FEM) approach. The FEM methodology is found to be robust, flexible and fast to compute flux density components. The leakage flux distribution around the circumference of concentric windings is studied. The windings of a three-phase, three limb transformer that are subject to the non-homogenous distribution of the field due to the presence of the core yokes and adjacent winding influence are modelled. The developed three-dimensional model shows that this effect can introduce an error in the region of 32% to the radial leakage field component. The results of the computational methods are compared to the experimental results of the measured stray losses. The test data of the same design that has been produced eleven times are presented. The stray losses in metal parts are evaluated and subtracted from the net measured stray losses to give measured winding eddy losses. A large error is observed between the calculated and measured winding eddy losses. It is further commented that the benefits of rigorous methods in computing any stray loss component can be suppressed by the variance of measured results of the same transformer design.

Acknowledgements

I wish to thank Professor Ivan Hofsajer for his insightful and illuminating discussions, without his patience, stimulating criticism, assistance and encouragement this work would not have been completed. My colleagues (Matshediso Phoshoko and Mercy Tshivhilinge) who assisted with the review of the dissertation chapters from the very beginning deserve a special mention.

I want to thank my partner Nonhle Wanda for her unconditional support. She remained patient with me, and at times assisted with the review of the text.

I would like to sincerely thank my father, sisters and brothers for their support and encouragement. I am indebted to my two adorable nieces Nosipho and Nokwanda Hlatshwayo whom I draw lots of inspiration from. The help of friends and colleagues who directly or indirectly supported me is also recognised.

Lastly, this work is supported in part by Powertech Transformers who provided resources and funding, it is gratefully acknowledged.

Contents

List of Figures

Figure Page

List of Tables

Table Page

List of Symbols

a	Homogenous solution first constant	
A	Magnetic vector potential	W/m
b	Homogenous solution second constant	
$\vec{B}$	Flux density vector	T
B	Flux density	T
B_r	Radial flux density	T
B_z	Axial flux density	T
BY	Bottom yoke	
C_n	Modified Bessel function solution constant	
D_n	Modified Bessel function solution constant	
$\vec{E}$	Electric field vector	V/m
E_s	Tangential electric field of the surface	V/m
h	Height of the strand	mm
$\vec{H}$	Magnetic field	A/m
H_s	Tangential magnetic field of the surface	A/m
I	Region between the core and the first winding	
II	Region within the first winding section	
III	The region after the first winding onwards	
I_0	Modified Bessel Function of the first kind of order zero	
I_1	Modified Bessel Function of the first kind of order one	

$\vec{J}$	Current density vector	A/m²
J_0, J_n	Current densities as Fourier series coefficients	A/m²
J_{exp}	Peak complex current density	W/m^2
K_0	Modified Bessel Function of the second kind of order zero	
K_1	Modified Bessel Function of the second kind of order one	
L	Core window height	
LLC	Load loss cost	R/kW
$n_{a,}$ n_r	Local number of axial and radial strands respectively	
n_{eT}, n_{rT}	Total number of axial and radial strands respectively	
NLC	No-load loss cost	R/kW
P_v	Losses	W
P_s	Surface loss density	W/m^2
P_e	Eddy current losses	kW
P_{LL}	Load losses	kW
P_{I^2R}	Transformer DC losses	kW
P_{stray}	Transformer stray losses	kW
P_{ws}	Transformer winding stray losses	kW
P_{we}	Transformer winding eddy losses	kW
P_{metal}	Stray losses in metal parts	W
P_{ea}	Axial component of winding eddy losses	W
P_{er}	Radial component of winding eddy losses	W

P_{NL}	No-load losses	kW
r	Radial position of the core, winding (radius)	mm
R_{Acs}	Price of all transformer accessories	R
R_{WQN}	Works quoted net	R
t	Strand thickness	mm
TY	Top Yoke	
TX_R	Transformer total price	R
V	Scalar potential	
WH	Winding Height	mm
z	Arbitrary axial position of the winding section	
Z_{sl}	Linear surface impedance	Ω
σ	Conductivity of the material	S/m
μ_0	Permeability of free space	H/m
μ_r	Relative permeability of the material	
ω	Angular frequency	rad/s
φ	The azimuthal direction	
ρ	Resistivity of copper	Ω.m
δ_{sl}	Skin depth	mm

Chapter 1

Introduction

Transformer performance parameters such as load losses and short-circuit impedance are intrinsic to its operations. Naturally these parameters are always optimized during the design process. These parameters are driven by the inherent leakage field between transformer windings. The leakage field induces eddy current losses in conductive structures such as windings, clamps, core laminations, flitch plates and the tank. Understanding the nature of the field distribution is important in determining these losses. This chapter provides the fundamentals of transformer load loss components. It also outlines the transformer design approach and different types of windings, and associated leakage fields which become important later when the eddy current theory and flux density calculations are discussed. The problem definition, objectives and dissertation structure are presented.

1.1. Power transformer load losses

Load losses directly influence the price of the transformer, which is governed by the capitalization formula. The capitalization formula is defined as the arithmetic sum of the cost components including the load and no-load losses, design, raw material and overheads. At design stage, this expression implicitly relates the no-load loss and load loss contributions using their respective cost factors as given by the customers.

Load losses are comprised of I^2R and stray losses. The term “direct current (dc) losses” is interchangeable with the “I^2R losses” in this dissertation. This is partly because these losses are from the fundamental r.m.s current components. However, the stray losses are not measurable directly and according to IEC 60076-1 [1], they are determined as the difference between the total and dc measured losses. The stray losses can be subdivided into winding stray losses and losses in metal parts. Figure 1.1 below shows a detailed breakdown of load loss components.

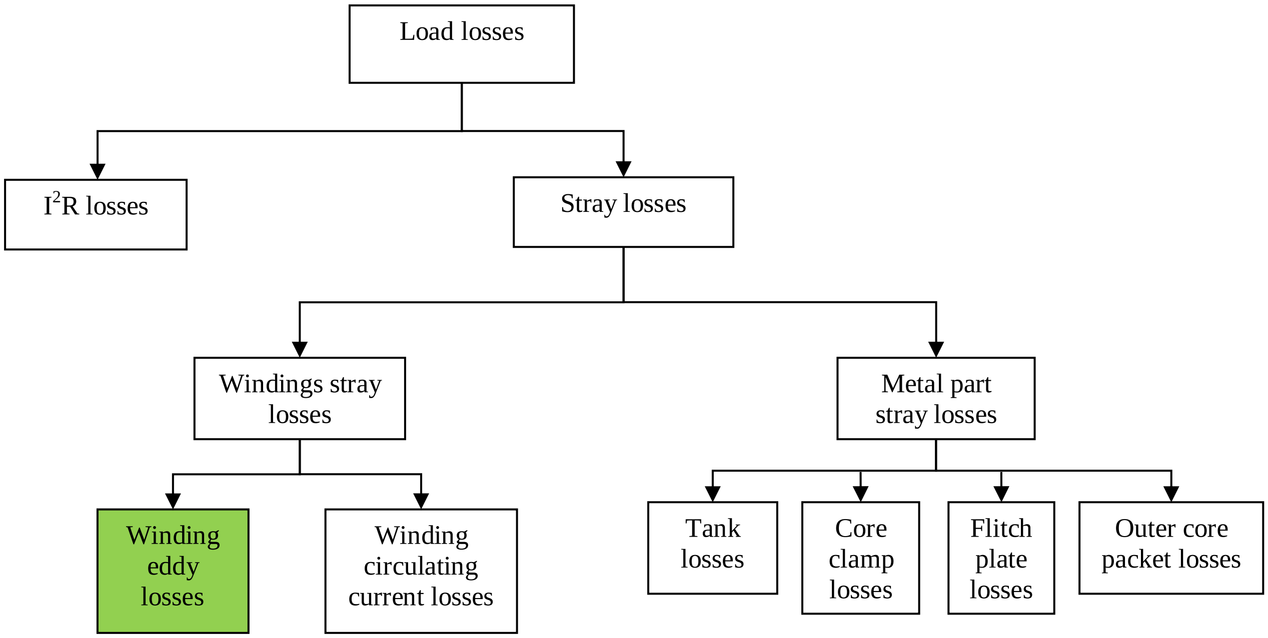

Figure 1.1: The breakdown of load losses into sub-components

The stray losses are the sum of the winding stray losses and losses in metal parts as illustrated in Figure 1.1. Firstly, there are two components that make up the winding stray losses, viz. the winding eddy losses and the circulating current losses. The winding eddy losses are a result of the axial and radial leakage flux components. The parallel connection of conductors situated in different radial positions linked by different field components cause circulating current losses. The second component, losses in metal parts constitute a significant contribution of the stray losses. The metal part losses include flitch plate, core clamp, tank wall and outer core packet losses. Furthermore, the computation of losses in metal parts is intricate due to the leakage field associated with these structures and requires advanced computation methods.

It is important that the segregation of stray loss components is understood, as Chapter 6 later refers to this breakdown. This dissertation focuses on the evaluation of winding eddy losses. They are considered to be the second largest component of the load losses following the dc losses. They also significantly affect the thermal performance of the transformer. The hot-spots in the windings are generated by the concentration of losses emanating from the leakage field. The winding hot-spot is defined as the ratio of the maximum losses in any disc to the average losses as stated in IEC 60076-7 [2]. Moreover the winding eddy losses are significant in the design of the cooling system of the transformer.

The winding eddy losses examined in this dissertation are assessed using Maxwell's equations and Poynting's theorem, that take into account the skin depth and proximity effect as detailed in Chapter 3. This analytical approach shows a dependency on the computation of the flux density. It follows that mapping the leakage field quantities presented in Chapter 4 for the winding regions is essential to the study. The computation of winding eddy losses using numerical and analytical approaches will also be vital.

1.2. Problem definition

The preceding section describes the origin of winding eddy losses. Essentially, the transformer conductors are situated in the time varying field governed by the source frequency (50Hz). The problem of winding eddy losses has in the past been solved using rectangular differential equations. This is despite the knowledge that the winding topologies which are presented in Section 1.3 are cylindrical in nature. The following complexities exist in the study of eddy currents due to the leakage field:

- Cylindrical versus flat conductor approximations.
- Conductor size versus skin depth.
- Convergence stability not always possible when dealing with analytical methods.
- Core window effect versus uniform field distribution.

The leakage flux evaluation is important in the study of winding eddy losses and possible to achieve with either an analytical or a numerical (FEM) approach. From long ago Rabins’ method has been the analytical method used by many transformer manufacturers. This dissertation focuses on its usefulness in the modern environment. The dissertation provides answers to whether this method is still relevant.

The transformer structure is naturally complex as conductors are not subject to homogenous fields. In a winding, a section of conductor is situated outside and another part inside the core window. To study this effect is not possible using the conventional two-dimensional models. In this dissertation this phenomenon is examined using 3-D FEM.

1.3. Transformer design approach

A power transformer comprises of a tank which is used to contain the active part, oil and to provide bushing interconnection paths. Transformer tank walls are made of magnetic steel, which make them susceptible to the leakage field. Considering the surface area of the tank, the losses induced are the second largest component of the stray losses after the winding eddy losses.

The core clamps and flitch plates are used to keep the core laminations intact. The core clamp design also includes the winding support feet. Interchangeably, the clamps, flitch plates and winding support feet can be constructed of magnetic and non-magnetic material. Likewise, these steel structures are prone to leakage flux penetration. Figure 1.2 shows the design of the majority of the components of the transformer that are subject to the leakage field. These components will guide the choice of simulation models presented in the following chapters.

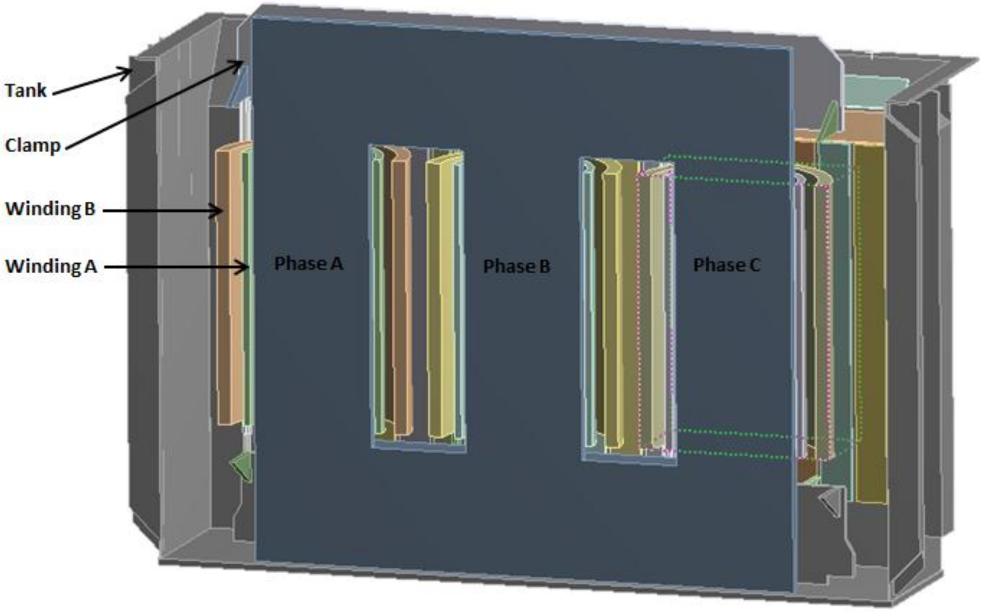

Figure 1.2: Three-dimensional geometry model showing conductive transformer components

In Figure 1.2, the windings and the core are collectively referred to as the active part, for they are pivotal components involved in the electromagnetic transfer of power. It is evident that the transformer geometry is a complex three-dimensional structure. The finite element method (FEM) packages that are able to simultaneously model all these structural components require expensive computational resources.

Now, the types of windings commonly manufactured are helical, disc and loop layer which are explained in detail below. For each winding type the application, advantages and disadvantages are outlined. This is important because the attributes of the windings are considered when modelling the full transformer for the evaluation of the overall winding eddy losses.

The characteristics of a helical winding shown in Figure 1.3 include: the pitch and multi discs with spacers in between. This winding is suitable for high current applications, it allows for the use of multi parallel conductor strands. The main problem with this winding configuration is the introduction of circulating currents between strands. If transpositions are properly done the circulating currents are reasonably eliminated.

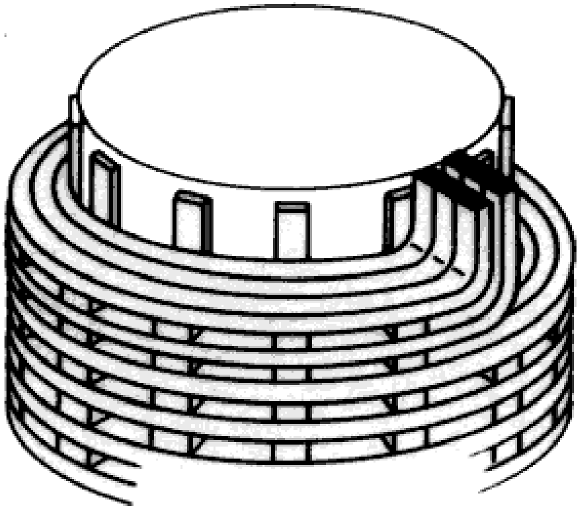

Figure 1.3: Design of a helical winding

A disc winding is depicted in Figure 1.4, this winding comprises of several conductors connected in series. Generally, the conductors are wound in the radial direction and then axially with the spacers separating the discs. The disc winding arrangement is suited for the requirement of many turns. The recommended application of a disc configuration is for the winding of the transformer‘s highest voltage system.

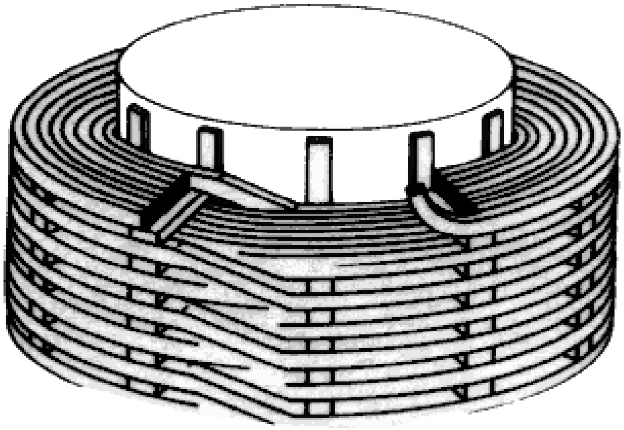

Figure 1.4: Design of a disc winding

Conductors of loop layer windings are arranged axially without spacers between consecutive turns. This winding type shown in Figure 1.5 is used for voltage regulation purposes, to provide different voltage tapings. The leads are successively connected to the tap-changing mechanism. The loop difference between conductors of this winding may result in undesired voltage stresses between conductors. The loop arrangement is customarily altered to mitigate this effect.

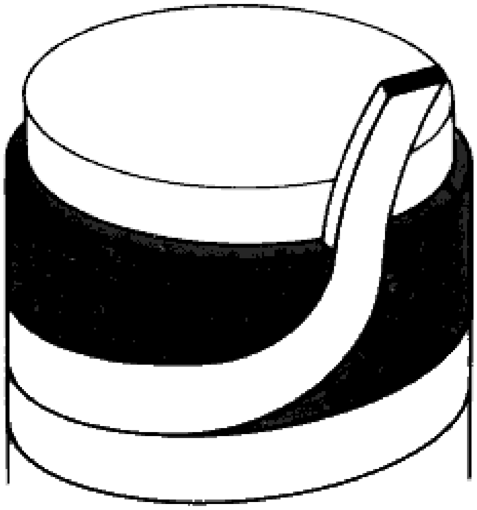

Figure 1.5: Loop Layer winding design

The variety of winding types described can be used for one transformer design with the common winding arrangement being low voltage (LV), high voltage (HV) and regulator (REG) respectively. In addition, for simulation purposes, it is impractical to model the windings including individual conductors with the configuration features defined above. Hence, in three-dimensional (3-D) and two-dimensional (2-D) FEM analyses, the windings are treated as cylindrical and rectangular objects respectively. This configuration will be seen in later chapters.

1.4. Research objectives

The main objectives of the dissertation are to:

- Assess if the one dimensional theoretical approach to estimate winding eddy losses is sufficient.
- Compute the flux density in the windings. The preferred method based on accuracy, flexibility and speed will be determined, the study focuses on 2-D FEM and Rabins' methods.
- Examine the core window effect on the calculation of winding eddy losses in terms of the field distribution inside and outside the window.
- Separate measured stray losses, with the assistance of three-dimensional techniques so as to obtain measured winding eddy losses.

1.5. Dissertation structure

In this dissertation the chapters are as follows:

Chapter 2: Eddy current losses in transformers

The review of previously applied methods of computing stray losses is conducted.

Chapter 3: Theoretical development of eddy currents

The mathematical formulation of eddy current problems for non-magnetic materials is discussed. The solutions of the differential equations describing eddy currents using Maxwell's equations are sought for both rectangular and cylindrical coordinates.

Chapter 4: Evaluation of Rabins' analytical method

The computation of the field using the analytical and 2-D FEM methods is presented. An investigation into the convergence of the Fourier series of the functions used to implement Rabins' algorithms is detailed.

Chapter 5: Core window effect

The study of the influence of the core window on the calculation of winding eddy losses is presented. The field distribution around the circumference of the windings is rigorously dealt with using the 3-D FEM solution. The overall winding eddy losses are calculated.

Chapter 6: Experimental results and discussion

The analysis of measured load losses of the tested transformers is conducted. The measured load loss results of eleven transformers of the same design are compared to the calculated results. A transformer model is prepared in 3-D FEM to calculate metal part losses to separate them from measured stray loss results.

Chapter 7: Conclusion and recommendations

A comprehensive summary involving the work of the previous chapters is entailed. The conclusion of the dissertation and recommendations of future work are provided.

Appendix A: Mathematica source code for the eddy current density calculation.

Appendix B: Rabins' method, algorithm implementation in Mathematica

Appendix C: Test transformer design data (40MVA, 132/11kV)

Appendix D: Load loss test reports

Chapter 2

Eddy current losses in transformers

The previous chapter presented briefly the transformer design approach, as well as the manufacturing of different windings. As outlined in Chapter 1 the objectives of this study are to assess the one dimensional method of eddy currents, compute the leakage field and study the core window effect to accurately predict the winding eddy losses. This chapter provides the background of stray losses in power transformers in a form of a literature survey of the past and current computational methods. It is clearly indicated earlier that the dissertation is focused on the computation of winding eddy losses. However in Chapter 6 the evaluation of losses in metal parts is essential to separate measured stray losses. Therefore, the computation of losses in structural parts is also discussed.

Stray losses are a considerable component of load losses which is indispensable due to its direct relation to transformer life. Transformer designers are constantly challenged to produce highly optimized performance, and low material volume designs to meet the customer demands. These demands elevate the need to develop numerical, analytical and empirical formulations that are able to more accurately determine performance parameters. Simultaneously, these solutions have to match the continual development of current computer technologies. In light of the above discussion, the stray loss problem should be analysed using three-dimensional FEM approaches.

This is due to the complex task of approximating the flux and current densities associated with structural components of a transformer (which are three-dimensional in nature) as presented in Chapter 1. Before the computational aspect is advanced it is important to present the typical two-dimensional model shown in Figure 2.1.

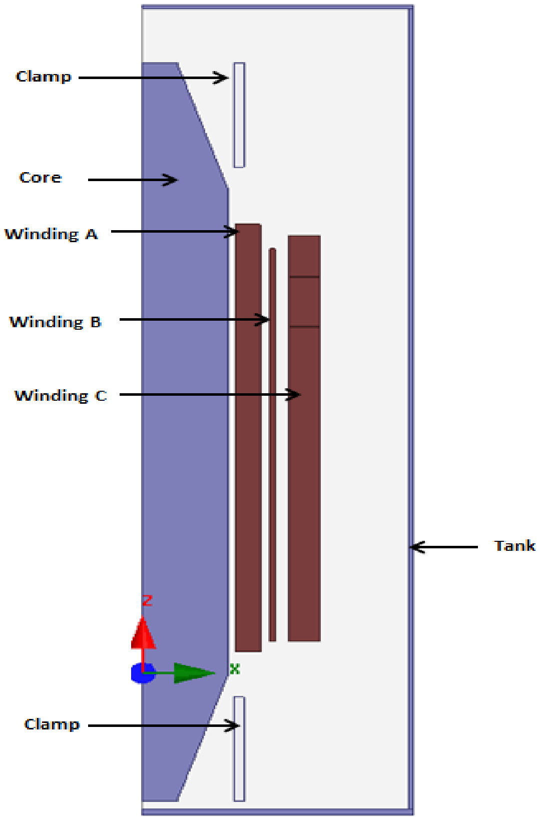

Figure 2.1: 2-D Cross sectional geometry of the transformer

It is well known that the three-dimensional simulations require extensive simulation time, thus the two-dimensional analysis of the transformer are usually the preferred solutions. Manufacturers embed this computational philosophy as part of their routine design program. In addition, the two-dimensional analysis uses an axisymmetric modelling since the windings are cylindrical in orientation. With this simplistic approach simplification errors are introduced. The field is not uniformly distributed along the winding circumference. In Chapter 5, a study of the effect of the core window on the computation of winding eddy losses is conducted. Furthermore, the winding designs shown in Chapter 1 are also different and have a geometric influence on the computation of winding eddy losses.

Despite advancing computational efforts to calculate stray losses, most manufacturers rely on hybrid methods i.e. combining numerous solutions, mainly based on experience. The use of such empirical formulations presents a gap of knowledge as they are often derived from historical design data. These methods are usually complimented by in-house rules which are driven by factory tolerances; thus their accuracy is seldom tested against computational techniques such as three-dimensional analysis. This chapter reviews the previously applied methodologies for computation of stray losses. More attention is paid to the evaluation of winding stray losses.

2.1 Winding eddy losses

The time varying field impinging upon copper conductors of the windings induces eddy current losses. Essentially the radial and axial flux density components of the field are responsible for the winding eddy losses. This section explores the previous endeavours of different researchers in trying to advance the computation of eddy currents in copper conductors, which are inherent to the normal transformer operating conditions.

In 1967 [3] Stoll presented the method of calculating eddy currents using numerical methods. The method is based on the finite difference techniques of successive over relaxation using digital computers. Stoll here outlines that numerical methods give solutions to complicated problems. The added advantage of numerical methods is the ability to test the validity of the simplifications. At large, this paper is devoted to the numerical treatment of eddy currents induced in conductors. Furthermore, he vigorously assessed the efficacy of the finite difference method based on the nodal analysis. However the finite difference method suffers from slow convergence due to the complex relationship of the current density and the magnetic vector potential. The convergence problem is stabilised by forcing the magnetic vector potential at the boundaries.

Stoll [4] in 1969 derived a formula for eddy current losses produced by a conductor of a rectangular cross sectional area. The main limitation of the formula is that the conductor dimensions must not exceed 6 times the skin depth for the formula/ solution to be valid. During the derivation, the field is assumed to be uniform and perpendicular to the conductor side. In addition, Stoll here focuses on deriving the analytical formulation of winding eddy losses by introducing the unknown exponential variables. He later simplifies the winding eddy current calculation by making it only dependent on the conductor sizes and the skin depth. In this publication, Stoll finds that the error, when the conductor dimensions are less than the skin depth, is within 2%. This comment is important in this dissertation as the conductor thickness is varied to assess the accuracy of the analytical formulation in Chapter 3.

Stoll [5] published a book focusing mainly on the theory of eddy currents. The winding eddy losses of the rectangular conductors are treated from first principles, with the application of the one- dimensional solution of the field. The field equations in differential form are simplified to yield a diffusion equation. The winding eddy loss governing equations for both radial and axial components are obtained using the simplifications that are tested in Chapter 3.

With the approximate winding eddy current known, Girgis et al in 1987[10], working for Westinghouse Electrical Corporation developed a 3-D program to calculate field quantities. They calculated the winding eddy losses and circulating current losses of the shell type transformers. The field quantities are acquired on a zone bases to improve the accuracy of the method. This demonstrates that the efforts to evaluate winding eddy losses using 3-D programs were already gaining momentum.

In other attempts, Ratomanalana describes a method to calculate the eddy current losses of transformers using the diffusion equation and boundary continuity conditions [6]. The boundary conditions involve the assumption that the tangential field component is constant on either side of the conductor. In deriving the relationship of the tangential field and the total losses, they are presented as a combination of three components: *x*-element, *y*-element and *xy*-element. The 2-D problem is decomposed into two 1-D problems to calculate the current components. In spite of the efforts, it is observed that the comparison of this method to the experimental results shows that the method seems to be accurate for higher frequency problems. The measured versus calculated results show an error above 7% at 1 kHz, which is the lowest frequency of the test.

In [8] , a shift towards the use of finite element method was witnessed; Kulkarni et al were more concerned about embedding the FEM tools in the design philosophy that is tailored to determine the leakage field quantities as part of the production line. The work presented in illustrates the evaluation of winding eddy losses using automated 2-D FEM. As it is later shown, this method is not entirely accurate as it fails to model the distribution of the leakage field around the circumference of the winding.

In trying to develop a faster method, [7] reports the results of the efforts carried out to estimate the winding eddy losses using the 3-D integral-equations for an electromagnetic field analysis package. This package simplifies the discretization of the eddy current problem by only considering the ferromagnetic zones. The equations are solved such that the field becomes available in the entire problem with the aid of the Biot-Savart law. This publication explicitly outlines that the computation of the electromagnetic field is indispensable towards the proper estimation of the leakage flux. In this instance, the radial flux density component shows that the field distribution inside the core window and outside the core window differs considerably. In observing this phenomena the authors do not comment on how this scenario affects the winding eddy losses.

A recent development on eddy current calculations was produced by Kulkarni et al [9] who derived the loss calculation formulae using the electric field approach. This yields the same results as achieved by Stoll. In addition, they briefly describe different methods of calculating the field components, namely; method of images, Roth's method, Rabins' method and 2-D FEM.

Most of the methods presented so far have proven to be pivotal in the development of the eddy current theory presented in Chapter 3. They also outline the importance of accurately determining the leakage flux quantities, which is presented in Chapter 4 of this dissertation. However, these methods fall short in taking into consideration the core window effect, except [7] which makes minimal efforts.

2.2 Circulating current losses

Parallel strands of a winding located in different radial positions generate circulating current losses. This is due to the different leakage flux linking these strands. The circulating current losses should be minimized as they can result in high hot-spot temperatures. If strands are completely transposed, using transposition schemes such as those described in [11], the circulating current losses equate to zero. In practice this is not always possible due to the extensive manufacturing time required.

Kaul [12] proposed an analytical method for computing circulating currents in stranded windings. The disadvantage with his method is that there is a higher calculation error for power transformer windings which have several strands in the radial direction. Kondo et al [13] used the equivalent circuit model to develop a numerical solution of magnetic vector and scalar potential for circulating current losses. The comparison is made to a 2-D FEM model and there is a fairly good agreement between the results obtained using both these methods. Koppikar et al [14] also covered the circulating current losses. The main problem with this method is that it is empirical in a sense that losses are computed as a percentage of I^2R losses.

2.3 Stray losses in structural parts

The computation of losses in structural parts is very important in the study of any component of transformer stray losses. The absence of the experimental approach, which separates measured stray loss components demands that all loss components be calculated rigorously. The survey of publications that deal with the calculation of stray losses was done by Kulkarni [15] in 2000, Olivares-Galván et al [16] in 2009 and Amoiralis et al [17] also in 2009. They all reveal growing interests in the computation of transformer losses particularly in Asia. This points to an increasing trend on the number of researchers using 3-D FEM techniques.

Structural parts such as tank walls, core clamps and flitch plates are manufactured from magnetic steel. Magnetic steel properties result in a relatively small skin depth as discussed in Chapter 3. During operation, this layer tends to saturate. This phenomenon leads to material becoming non-linear. Schaidtz [18] studied the losses in the tank and core clamps by introducing the saturation layer assumed to be less than the material skin depth. The variation of the saturation layer was represented as a Fourier expansion for different phase excitations. This 3-D analysis made it possible to identify localised high loss density areas.

The suppliers of most 3-D analysis tools offer comprehensive FEM packages. This simplifies computational requirements albeit simulation time and memory demands remain the same. FEM packages today have built-in mesh simplification techniques; such a package was used by Valkovic [19] and Kralj [20] who studied the losses using the surface impedance method. The method allows for the computation of losses without having to mesh or solve the inside part of the object. In both these publications the linear and nonlinear surface impedance method results are compared. The following subsections review individual metal part structures. The analytical, numerical and empirical formulations are studied.

2.3.1 Tank wall losses

Losses in the tank walls are due to the main leakage flux impinging upon the surfaces of the tank. High current carrying leads passing through the tank will also generate losses. This is the case in the tank cover where leads are passing through bushing holes. As a result, these loss components are reviewed separately in the subsections below.

In 1979 Valkovic [21] described an analytical method to calculate tank wall losses. The method takes into account the curvature, shape of the tank and 3-phase excitation. The non-linearity of the material is taken into consideration using complex permeability. In comparison to the measured stray losses, the calculated losses yielded an error less than ±20 %. This work is still the foundation of developing analytical solutions for tank wall loss calculations.

Szabados et al [22] also presented an analytical method to calculate tank wall losses. The incident field is represented as a double Fourier series function. An experimental determination of the eddy current density is conducted. A small experimental electromagnetic setup to generate an incident field was prepared and the plate losses were then measured. The main problem with this study is that it does not take into account the non-linearity of the material.

The interest in using surface impedance started as early as 1991 and was used by Holland et al when they conducted a study to calculate tank wall losses [31]. In this publication the non-linearity effect is taken into account using Aggarwal’s approximation. The test results of two transformers are presented i.e. 160 MVA and 20 MVA. In both instances the results showed reasonable agreement. This method is relied upon even today for tank wall calculations in 3-D FEM programs.

High current carrying conductors induce losses due to the field surrounding the conductor. The tank cover is a subject of this phenomenon, in particular, the bushing holes. Most studies on the other components of stray losses omit to subtract this component from measured stray losses. It is however important especially when LV currents may be significant. In 1997 Turowski [24] published a paper on eddy current losses and hot-spot evaluation in tank covers. The calculation demonstrates the use of Maxwell’s equations and analytical solutions of the field. The distance between bushings and the bushing hole diameters are investigated. The method presented in this paper was validated against approximated formulations that were previously used. It has since provided the foundation of computing cover losses. Eddy current losses have also been studied [25], [26], [27], [28], [29]. In most of these publications, the 3-D approach is prevalent.

It is noted that 3-D FEM is dominant in the computation of tank wall losses as the nature of the geometry structure is three-dimensional; other authors that have contributed to this approach include Schmidt [30] and Guérin [64]. The expectation is a rapid increase in researchers using 3-D FEM to investigate tank wall losses, a factor underpinned by the increase in the availability of computational power to researchers. The analytical methods will however continue to lay a foundation as they are easily implementable and fast.

2.3.2 Core clamp losses

Few authors have published analyses dedicated to the calculation of core clamp losses. Nonetheless, Žarko et al [33], conducted a 3-D FEM study evaluating core clamp losses of a 40 MVA distribution transformer. Linear surface impedance modelling and tetrahedral meshing methods are applied for different core clamp designs. Furthermore, losses are evaluated as a function of permeability and an insignificant variation is seen for permeability in the range of 300-700. Janic et al [32] also analysed core clamp losses using the finite element method. The investigation focused on examining the practical reduction measures for minimizing core clamp losses. The dramatic reduction is observed when changing the winding to core clamp distance. The winding support feet and core clamp design has significant influence. Kadir [34] presented experimental work; the results of the loss density measured are compared to mathematical formulation based on the assumption that the flux density of 0.75 T of the maximum B-H curve value. The generalization that from 100 MVA to 400 MVA results are fairly accurate is postulated; this study however is very generic and may not be applicable for a variety of clamp design philosophies.

2.3.3 Flitch plate and outer core packet losses

Stray flux departing radially through the inner surface of the winding impinges upon the core and surfaces such as the flitch plate [35]. The dimensions of the flitch- or tie plates are generally small in comparison to the core diameter. Practically, the flitch plate thickness ranges from 10-20 mm and they cover a small section of the core circumference. Furthermore, the flitch plate losses do not significantly contribute to the total load losses. However, localized stray losses can lead to hazardous hot-spot temperatures. The loss density distribution can be high as these plates are situated closer to the windings and have poor cooling surfaces.

Literature covering flitch plate losses is also very limited; Kulkarni et al [35] analysed flitch plate losses in 2-D and 3-D FEM. Further to that, he conducted a statistical model (ANOVA) to determine the geometry parameters that influence flitch plate losses. The reduction of losses by introducing vertical slots in flitch plate materials was also studied.

Flitch plate losses have also been calculated by Lin et al [36] using FEM. The surface impedance method is applied using the scalar magnetic potential. One such method is also found in a study by Ma et al [37] in which they presented the simulation results based on magnetic vector potential. The simulation was conducted in ANSYS. The shortcoming however is, results in both cases have not been compared with either in-service tools or experimental results. The inability to measure stray loss components separately is a major disadvantage in the computation of any stray loss component.

Different computation methods have been reviewed in the preceding sections and based on these, it is apparent that losses in metal parts is an important field of study and is fundamental to the study of winding eddy losses. The losses in metal parts are important and will be further discussed in the practical results chapter.

2.4. Conclusion

The literature review of winding eddy losses, circulating current losses and various metal part losses was presented in this chapter. Studies on winding eddy losses require that assumptions be made to simplify the behaviour of the magnetic field vector potential. The literature outlines the field quantities and conductor sizes as important parameters in the study of winding eddy losses. The derivation of eddy current losses is based on rectangular conductors, and will be essential in the theory development in Chapter 3, which is congruent to the work of Stoll.

The review of the three-dimensional methods used to determine winding eddy losses is essential. The authors [7], [10] reveal the importance of understanding the three dimensional phenomena; one such is the non-uniform distribution of the field around the winding circumference. Similarly, the results of the three-dimensional methodology are discussed in Chapter 5, although in this dissertation an advanced FEM package is used. The advantage will be the superior integration resolution in comparison to the previous studies. The field components will be integrated per mesh element as compared to integrating components of a few zones. This further minimizes calculation errors.

On the circulating current losses, the assumption is that there is a complete transposition of conductors in each winding. Subsequently, the circulating current losses become zero. In the analysis of the measured results, this component is ignored.

Different methodologies for calculating the stray losses in metal parts are reviewed. The use of numerical methods is dominant, specifically the three-dimensional finite element method. The use of a nonlinear impedance model method in the calculation of the metal part losses is widely investigated. In addition, the FEM package available for this study is known to have a deficiency in taking nonlinearity into account. Hence, in this dissertation the method of compensating for nonlinearity is sought after in Chapter 6.

Lastly, the review of individual loss components demonstrates the continuing interests in developing advanced methodologies. The next chapter deals rigorously with the eddy current formulation on non-magnetic materials. The eddy current analysis is examined from the rectangular and cylindrical perspectives.

Chapter 3

Theory development: Analysis of eddy currents

The literature review of stray losses is presented in the previous chapter. As identified the eddy current losses emanate from the leakage field. The conductors that are situated in the time varying field satisfy Maxwell's equations. The objective of this chapter is to describe the eddy current theory of a single conductor from the fundamental field equations. This developed theory then shows how it relates to the winding eddy losses of a power transformer.

A transformer under operation has its structural parts impinged upon by the leakage flux. As such, the winding conductors are subject to axial and radial flux penetrations. From the practical perspective, the eddy current phenomenon is only experienced through the terminal voltage/current measurements. It is experimentally intricate to separate the losses induced in winding conductors and metal part structures. Equally, the problems involving eddy currents induced in conducting materials by time varying field are too complicated to solve by analytical methods [3].

The use of numerical solutions has been prevalent and one such method is Finite Difference Method (FDM). In this method the Partial Differential Equations (PDEs) are replaced by finite difference equations, in discrete points [4]. The numerical tool that researchers are now interested in involves FEM. The underlying principles of FEM are premised on solving the PDEs using ordinary differential equations. In this case, the problem domain is discretized and solved by eliminating the PDEs, thus integrating the solution numerically using Euler's or Runge-Kutta's methods.

Despite these advances the problem of winding eddy losses cannot be solved in its entirety using FDM or FEM. This is because the winding construction consists of numerous stranded conductors as discussed in Chapter 1. Hence, in order to precisely calculate the winding eddy losses using FEM, the problem should include modelling all conductors individually. This has however proven to be time consuming particularly if done as part of the design routine program. Consequently, the combination of analytical and numerical solutions is inevitable.

The eddy current solution can be analytically defined using Maxwell's equations. The results provide the governing equation that explicitly defines the relations between eddy losses and the flux density components. In this chapter the problem formulation of eddy currents is discussed thoroughly, where the use of different coordinate system solutions of the differential forms is detailed. The leakage field computations related to the resultant formulae are discussed in the next chapter.

3.1. Electromagnetic formulation in time varying field

Transformer winding eddy losses inherently belong to the classical category of electromagnetic problems as the conductors are situated in the time varying field. This situation by definition satisfies the set of partial differential equations that define the behaviour of electromagnetic fields around the conductors. These equations are known as Maxwell's equations, and are comprised of Gauss's law, Gauss's law for magnetism, Faraday's law and Ampere's circuital law. In this section, the applicable equations to transformer winding eddy losses are provided in differential form. Starting with the Faraday's law:

$$\nabla \times \boldsymbol{E} = -\frac{\partial \boldsymbol{B}}{\partial t} \tag{3.1}$$

Faraday [38] discovered that the current is induced in a conducting loop when the magnetic flux linking the loop is changed. The application of this law in the case of transformer winding is profound.

Ampere's circuital law:

$$\nabla \times \boldsymbol{H} = \boldsymbol{J} \tag{3.2}$$

Equation 3.2 defines the current density as the curl of the magnetic field; it is this equation that led Maxwell in his earlier work to introduce the displacement current term accounting for the conservation of charge. Developed in the 18th century when Maxwell presented a publication entitled "A Dynamic Theory of the Electromagnetic Field" in the establishment of the theory of light [39], it first appeared in the publication "Physical lines". To date, in the application to power transformers, the displacement current has been deliberately omitted (quasi-stationary limit) as shown in Equation 3.2.

Gauss's law for magnetism:

$$\nabla . \boldsymbol{B} = 0 \tag{3.3}$$

The curl of magnetic vector potential gives the point flux density quantity:

$$\nabla \times \boldsymbol{A} = \boldsymbol{B} \tag{3.4}$$

Further to Maxwell's equations the relationship between the **B** and **H** fields for linear and isotropic materials is:

$$\boldsymbol{B} = \mu_0 \mu_r \boldsymbol{H} \tag{3.5}$$

It is also important to represent the current density in terms of the electric field, which is implicitly Ohm's law:

$$\boldsymbol{J} = \sigma \boldsymbol{E} \tag{3.6}$$

Combination of (3.1) and (3.4) yields:

$$\nabla\times \boldsymbol{E} = -\frac{\partial(\nabla\times\boldsymbol{A})}{\partial t} \tag{3.7}$$

It is useful to define the electric field in terms of the vector and scalar potentials. This is attained by integrating Equation 3.7,

$$\boldsymbol{E} = -\frac{\partial \boldsymbol{A}}{\partial t} - \nabla V \tag{3.8}$$

Further combination of (3.1) and (3.5) with (3.6) results in

$$\nabla \times \frac{\boldsymbol{J}}{\sigma} = \frac{-\mu \partial \boldsymbol{H}}{\partial t} \tag{3.9}$$

The current density has been expressed earlier on as a function of the magnetic field, therefore substituting Equation 3.2 into 3.9 and rearranging the results yields the following equation:

$$\nabla \times \nabla \times \boldsymbol{H} = \sigma\mu \frac{-\partial \boldsymbol{H}}{\partial t} \tag{3.10}$$

Considering the left hand side of Equation 3.10, the solution of the curl of the curl of the field is simplified according to the relationship between the curl and the dot product.

$$\nabla \times \nabla \times \boldsymbol{H} = \nabla \times (\nabla . \boldsymbol{H}) - \nabla^2 \boldsymbol{H} \tag{3.11}$$

The properties of the vector operator of Equation 3.11 are well known in the mathematics fraternity, one such is covered by G James [40]. Combining the expressions given in (3.11) and (3.10) the term containing $\nabla . \vec{H}$ becomes zero satisfying Equation 3.3

Hence:

$$-\nabla^2 \boldsymbol{H} = -\sigma\mu \frac{\partial \boldsymbol{H}}{\partial t} \tag{3.12}$$

∇^2 is called the Laplacian operator. In addition, Equation 3.12 is known as a second order diffusion equation. The solution of this equation becomes the cornerstone of the derivation of the formula for eddy losses. The relations in Equation 3.12 describe the magnetic field expression, notwithstanding that the electric field similarly yields the same form of diffusion equation given as:

$$\nabla^2 \boldsymbol{E} = \mu\sigma \frac{-\partial \boldsymbol{E}}{\partial t} \tag{3.13}$$

In the analysis of eddy currents the solution of the diffusion equation can be solved from two perspectives that is, magnetic field or electric field. For an instance, Kulkarni et al chose to use the electric field approach [9]. In the next section the Cartesian coordinate solution of the Laplacian operator is provided and this chapter uses the magnetic field approach.

3.2. Analytical solution of the diffusion equation

This section is devoted to solving the diffusion Equation 3.12 presented in the preceding section. The eddy current problem is treated using the Cartesian coordinates. This configuration has generally permitted the assumption that the eddy currents due to the perpendicular field flow only in the *x*-direction as in Figure 3.2. Stoll dedicated a chapter in his book published in 1974 [5] to explain this treatment which he termed one-dimensional eddy-current flow. The derivation shows later that the material properties, conductivity and permeability are significant for this assumption. However, this approach has been widely accepted and the results thereof.

The typical layout of conductors of few turns is depicted in Figure 3.1 below. It should be borne in mind that the windings are made up of several conductor strands as shown in Chapter 1 where different winding types are presented. Moreover, the validity of the one-dimensional approach is critically assessed later in this chapter.

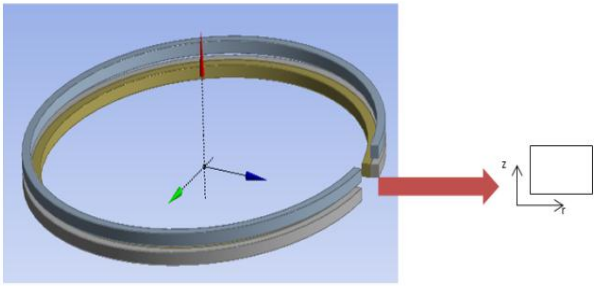

Figure 3.1: Transformer winding coil

Figure 3.1 confirms the problem orientation in cylindrical coordinates, this means the definition and assumptions above are not free from errors, as they do not take the curvature into account. In light of deficiencies of the one-dimensional analysis which were chosen for this section, the magnetic field is further assumed to possess only the *z*-component.

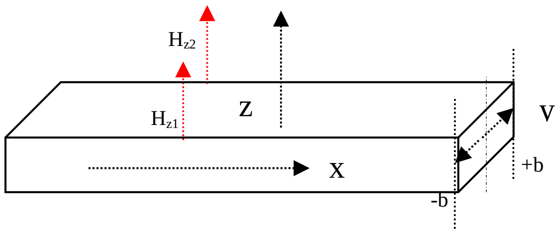

Figure 3.2: Field penetrating a conductor

Figure 3.2 illustrates the field components penetrating the winding conductor. Since there is only a *z*–component of the magnetic field, the eddy current density will be induced in the *x*- direction.

The information presented above allows for the recall of Equation 3.2. The expansion of the field with the associated unit vectors produces:

$$\begin{vmatrix} i & j & k \\ \frac{d}{dx} & \frac{d}{dy} & \frac{d}{dz} \\ H_x & H_y & H_z \end{vmatrix} = \left(\frac{dH_z}{dy} - \frac{dH_y}{dz}\right) i - \left(\frac{dH_z}{dx} - \frac{dH_x}{dz}\right) j + \left(\frac{dH_y}{dx} - \frac{dH_x}{dy}\right) k \quad (3.14)$$

According to the description of the one-dimensional approach, it is deduced that certain components of the field become zero, namely:

$H_x, H_y, J_y, J_z = 0$

Substituting the zero field components in 3.14 result in:

$$\frac{dH_z}{dy} = J_x \qquad (3.15)$$

Now, the combination of Equation 3.9 and 3.15 becomes:

$$\frac{dJ_x}{dy} = \mu\sigma \frac{dH_z}{dt} \qquad (3.16)$$

It is essential that Equation 3.16 is represented in the frequency domain as follows:

$$\frac{dJ_x}{dy} = j\omega\mu\sigma H_z \qquad (3.17)$$

Let,

$$\gamma^2 = j\omega\mu\sigma \to \gamma = \sqrt{j}\,\sqrt{\omega\mu\sigma} \qquad (3.18)$$

From first principles the complex definition is:

$$\sqrt{j} = \sqrt{e^{j45}} = \cos 45 + j\sin 45 = \left(\frac{1+j}{\sqrt{2}}\right) \tag{3.19}$$

Hence, $\gamma = \left(\frac{1+j}{\sqrt{2}}\right)\sqrt{\omega\mu\sigma}$

From 3.19, the term containing the root is defined as:

$$\delta = \sqrt{\frac{2}{\omega\mu\sigma}} \tag{3.20}$$

This term is known as the skin depth and according to [41] the formal definition is:

"For a given frequency, the depth at which the electric field strength of an incident plane wave, penetrating into a lossy medium, is reduced to 1/e of its value just beneath the surface of the lossy medium". Using the material properties of copper, the skin depth at 50 Hz is 0.00933 m according to the calculation done later in Equation 3.43. From the combination of Equation 3.16 and 3.15 the magnetic field is simplified as:

$$\frac{d^2H_z}{dy^2} = \mu\sigma\frac{dH_z}{dt} \tag{3.21}$$

The general solution of the simplified diffusion equation in 3.21 is:

$$H_z = K_1e^{\gamma y} + K_2e^{-\gamma y} \tag{3.22}$$

Where:

K_1 and K_2 are solution constants and can be found using the field boundary conditions. Also the current density is reduced to:

$$J_x = \frac{dH_z}{dy} = \frac{d}{dy}(K_1e^{\gamma y} + K_2e^{-\gamma y}) \tag{3.23}$$

From Figure 3.2 consider the following boundary conditions:

At y =b , $H_z = H_{z1}$

At y =-b , $H_z = H_{z2}$

Using the boundary conditions and solving the system of two simultaneous equations, the constants become:

$$K_1 = \frac{H_{z1}e^{\gamma b} + H_{z2}e^{-\gamma b}}{e^{2\gamma b} - e^{-2\gamma b}} \tag{3.24}$$

$$K_2 = \frac{H_{z2}e^{\gamma b} - H_{z1}e^{-\gamma b}}{e^{2\gamma b} - e^{-2\gamma b}} \tag{3.25}$$

If it is assumed that the field on the left side of the conductor equals to the field on the right side, the constants are:

$$K_1 = K_2 = \frac{H_{z0}(e^{\gamma b} + e^{-\gamma b})}{e^{2\gamma b} + e^{-2\gamma b}} = \frac{H_{z0}}{e^{\gamma b} + e^{-\gamma b}} \tag{3.26}$$

This assumption suggests the field is homogenous in the *y*-direction of the conductor. For simplicity this assumption is accepted as the thickness of the strands is normally small. Substituting constants and using trigonometric manipulation results in:

$$H_z = \frac{H_{z0}}{e^{\gamma b} + e^{-\gamma b}}(e^{\gamma y} + e^{-\gamma y}) = \frac{H_{z0} cosh\gamma y}{cosh\gamma b} \tag{3.27}$$

The result presented in Equation 3.27 is of utmost importance; it represents an analytical solution of the field inside the conductor. Hence, the effort is made to illustrate and understand the behaviour of the field in a conductor. A conductor of the configuration shown in Figure 3.2 is analysed. It has a thickness of 2.4 mm, and this size was chosen because it is equivalent to that of the first winding of the transformer presented in Chapter 5.

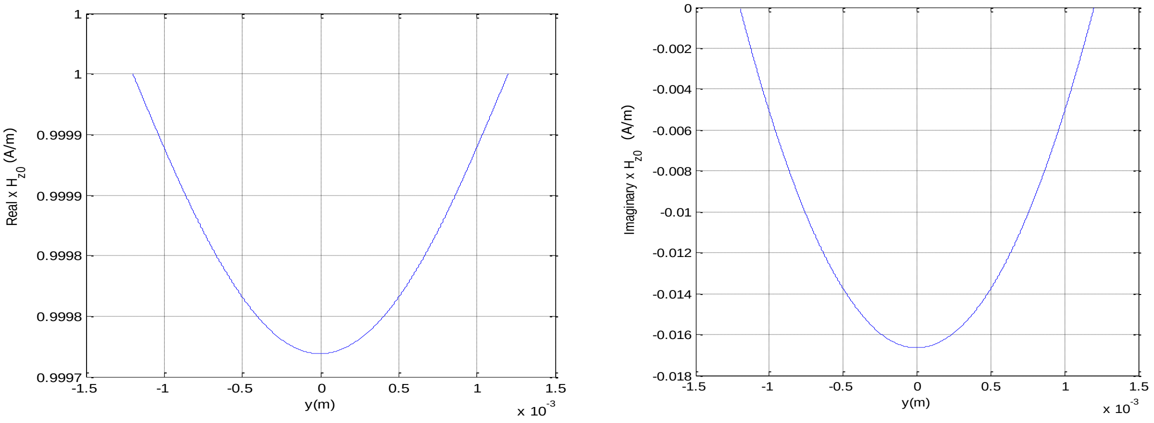

Figure 3.3: The real and imaginary components of H_z

Figure 3.3 above depicts the results obtained from the calculation of the trigonometric functions in Equation 3.27. The limits of the y dimensions are -1.2 mm to 1.2 mm. Thus the real and imaginary components show a hyperbolic distribution at different positions of the conductor, changing from the minimum to the maximum size. Furthermore, an important observation from Figure 3.3 is that the magnitude of the real and imaginary components differs substantially. Again at y equals to zero the extreme values are observed from both curves, the real showing the minimum and the imaginary showing the maximum field.

Lastly, the resultant magnetic field expression in Equation 3.27 is principal to the calculation of losses when combined with results of Poynting's theorem detailed in the next section.

3.3. Power loss density

The theory encompassing the computation of the losses due to the time varying field has been sufficiently developed. The physical definition of electromagnetic losses relies on Poynting's theorem. This theorem is widely applied to the cases of transmission lines. However according to Franklin [42] the use of this theorem started long before it was formally defined as Poynting's theorem. In this publication he discusses the simplistic representation of the theorem using current and voltage. Nonetheless, in this section the derivation of the theorem is provided. According to Poynting's vector, the loss density can be represented as the cross product of the electric field and magnetic field.

$$\boldsymbol{S} = (\boldsymbol{E} \times \boldsymbol{H}) \tag{3.28}$$

The representation in Equation 3.28 is known as Poynting's vector, which defines the loss density according to the electromagnetic field quantities. The surface integral over the enclosed surface of the same equation results in Equation 3.29.

The power losses are now:

$$P = -\oint_s (\boldsymbol{E} \times \boldsymbol{H}).nds \tag{3.29}$$

Therefore the mathematical representation of Poynting‘s theorem is:

$$\oint_s (\boldsymbol{E} \times \boldsymbol{H}).nds + \oint_v H.\frac{\partial B}{\partial t} dv = -\oint_v J.Edv \tag{3.30}$$

According to Equation 3.30, the total power equals to the sum of Ohmic losses and power absorbed by the magnetic field. Hence, using the magnetic field and current density Equation 3.30 can be grouped in terms of the volume integral:

$$\oint_v J.\frac{J}{\sigma}dv + \oint_v H.\frac{\partial \mu_0 \mu_r H}{\partial t}dv = -\oint_s (E \times H).nds \tag{3.31}$$

The average power loss density is given by:

$$S = \frac{1}{2}(\mathbf{E} \times \mathbf{H}^*)\ W/m^2 \tag{3.32}$$

Where, $\mathbf{H}^*$ is the complex conjugate of **H**. This relationship is illustrated in Equation 3.33 below.

$$H = Re\left[He^{jwt}\right] = \frac{1}{2}\left(\mathbf{H}e^{jwt} + \boldsymbol{H}^* e^{-jwt}\right) \tag{3.33}$$

Incorporating Equation 3.33, Poynting's theorem in complex form becomes:

$$\frac{1}{2\sigma}\oint_v |J|^2 dv + j2\omega\mu_0\mu_r \oint_v |\mathbf{H}|^2 dv = -\oint_s S.nds \tag{3.34}$$

On the basis of the one-dimensional approach, there exists only the *x*-component of the current density and taking the real component of Equation 3. 34, the loss equation is:

$$P_e = \frac{1}{2\sigma}\int_{-b}^{+b} |J_x|^2 dy \tag{3.35}$$

This integral equation is vigorously applied in the next section. It is combined with the analytical solution of the current density of the previous section.

3.4. One dimensional solution application

Using the diffusion equation and a solution from the boundary conditions of Equation 3.12, a better definition of the current density is established. This current density is combined with the integral equation of the Ohmic losses. In summary, the current density involves intricate trigonometric functions. Thus, appropriate identities are applied to simplify the equation.

$$J_x = \frac{dH_z}{dy} = \gamma\frac{H_{z0} sinh\gamma y}{cosh\gamma b} \tag{3.36}$$

Using Equation 3.36, the current density distribution in a conductor is studied in the same manner as Section 3.2. The conductor of the same size is considered and the current density is calculated as a function of H_{z0} as shown in Figure 3.4. Similarly, the equation is evaluated at different points along the y-axis.

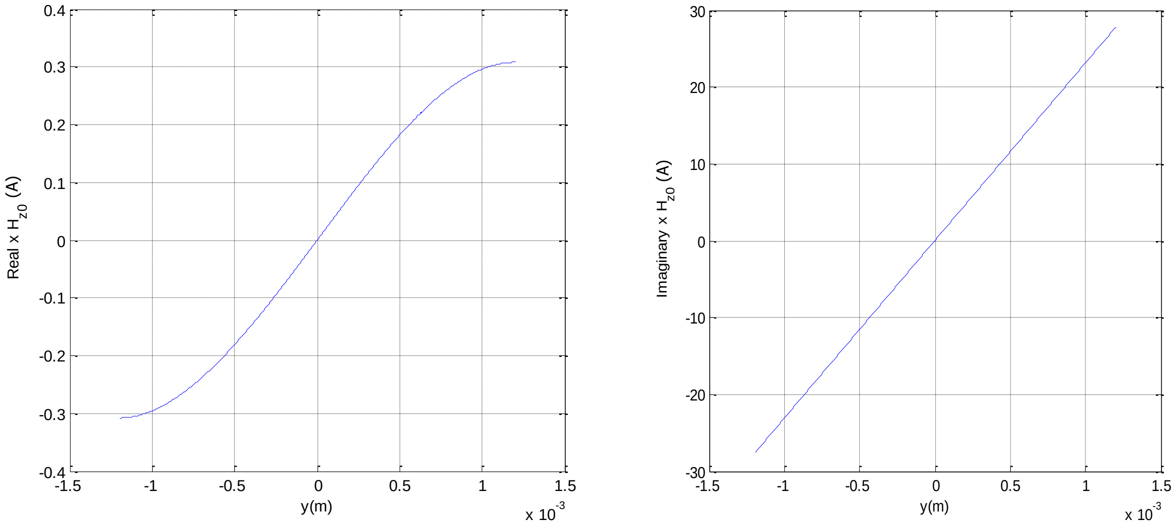

Figure 3.4: Real and imaginary components of the current density inside a conductor

In Figure 3.4, the real and imaginary components of the current density are plotted. The distribution of the two components yields different profiles. The imaginary component is two orders larger than the real component. Hence, the imaginary component is dominant in the complex expression.

Now, recalling the loss density described in Equation 3.35 and substituting J_x the losses become:

$$P_e = \frac{1}{2\sigma}\int_{-b}^{+b}\left|\gamma\frac{H_{z0}sinh\gamma y}{cosh\gamma b}\right|^2 dy \qquad (3.37)$$

Rearranging Equation 3.37 to include only the y integrand yields:

$$P_e = \frac{\gamma^2 {H_{z0}}^2}{2\sigma cosh^2\gamma b}\int_{-b}^{+b}|sinh\gamma y|^2 dy \qquad (3.38)$$

In order to integrate 3.38, trigonometric identities given in [43] are helpful. However before they are given, it is important to define the reciprocal of the skin depth to relax the mathematical complexity.

$$k = 1/\delta = \sqrt{\frac{\omega\mu\sigma}{2}} \tag{3.39}$$

From Equation 3.38 and 3.39, the trigonometric functions are simplified as follows:

$$|sinh\gamma y|^2 = \frac{1}{2}[coshky - cosky] \tag{3.40}$$

$$|cosh\gamma b|^2 = \frac{1}{2}[coshkb + coskb] \tag{3.41}$$

Integrating (3.38) and substituting (3.40) and (3.41) the loss expression becomes

$$P_e = \frac{H_{z0}{}^2[sinh2kb - sin2kb]}{\sigma\delta[cosh2kb + cos2kb]} \tag{3.42}$$

Equation 3.42 is the loss density for both non-magnetic and magnetic materials. The relative permeability of copper is 1 therefore copper can be treated as a non-magnetic material. To analyse the relationship between the skin depth and strand sizes, it is important to simplify the trigonometric functions. For the practical analysis, the conductor size limitations from the manufacturers will constrain the dimensions. These limitations are the maximum and minimum dimensions that the copper suppliers can manufacture. Hence, the data from three suppliers have been displayed in Table 3.1. Before the assessment of Equation 3.42 is performed, the types of conductors are described to enhance the understanding of the manufacturing limits.

Transformer windings are manufactured of copper strands insulated with paper or enamel. The strands are laid out as edge wound or flat wound. The explanation of the two topologies follows.

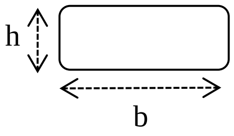

Figure 3.5: Edge wound strand

Figure 3.5 shows the edge wound strand, from the transformer manufacturing perspective this conductor configuration can only be used in a regulator winding. The latter applies specifically for layer windings, due to the difficulties associated with the winding processes. The main characteristic of this arrangement is that the *b* dimension is greater than the *h* dimension.

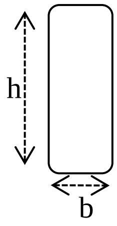

Figure 3.6: Flat wound strand

The flat wound strand is presented in Figure 3.6. This type of strand is not limited to applications of any winding type. Its attribute as depicted in Figure 3.6 is that the b dimension is always smaller than the h dimension. It has already been seen that the field in the conductor is influenced by its thickness; in this section a meaningful assessment of the overall loss equation is presented.

The main aim of the above discussion is to introduce the mechanical constraints surrounding the conductor dimensions. Hence, the influence of the above configurations is assessed. Furthermore, the comparison of a multitude of strand sizes and skin depth is presented.

Table 3.1: Supplier’s maxima and minima conductor dimensions

		ASTA (mm)	**BTEW (mm)**	**Aberdare (mm)**
b	Max	23	8	8
	Min	2	0.8	1.5
h	Max	7.5	21	35
	Min	0.8	3.5	4

Courtesy of ASTA, BTEW and Aberdare

Consider the calculation of the skin depth of copper:

f = 50 Hz

$\mu_0\mu_r$ = $4\pi e-7$ H/m

σ = $5.814e07$ S/m

Substituting the above parameters in Equation 3.20 gives:

$$\delta = \sqrt{\frac{2}{\omega\mu\sigma}} = \sqrt{\frac{2}{2\pi f\mu\sigma}} = \sqrt{\frac{2}{2\pi\times 50\times 4\pi e{-}7\times 5.814e07}} = 9.33 \text{ mm} \qquad (3.43)$$

The knowledge of the skin depth provides the critical thickness that becomes important as the radial dimension of a conductor is changed.

Further assessing the skin depth relations to the conductor size the two extreme cases are considered.

When $\delta \ll 2b$ the losses are:

$$P_e = \frac{{H_{z0}}^2}{\sigma\delta} \qquad (3.44)$$

When $\delta \gg 2b$ the losses are:

$$P_e = \frac{{H_{z0}}^2(2kb)^3}{6\sigma\delta} \qquad (3.45)$$

Using the dimensions provided in Table 3.1, it is important to assess the validity of this assumption before the final governing equations are derived. This is done by evaluating Equation 3.42, where the distribution of the trigonometric functions is obtained from different conductor thickness as shown in Figure 3.7.

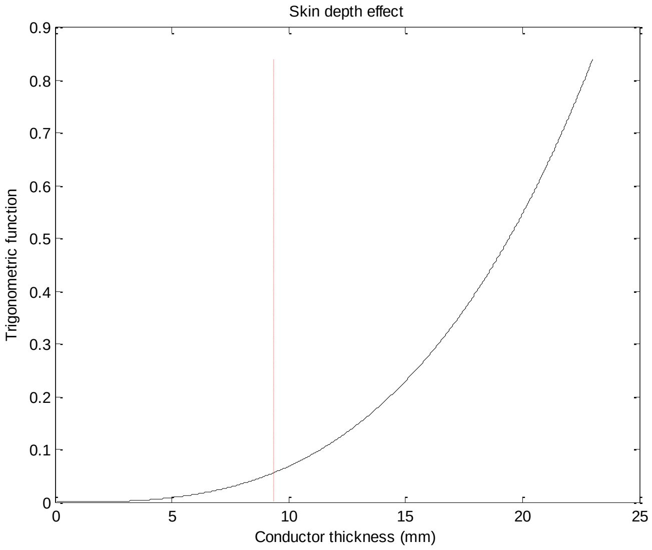

Figure 3.7: Trigonometric function ratio of Equation 3.42 versus conductor size

Figure 3.7 presents the solution of the trigonometric part of Equation 3.42. Of this equation only the trigonometric part is evaluated as it directly affects the earlier assumption. The maximum size of 23mm of the conductor that can be supplied by ESTA as provided in Table 3.1 is used as a guideline. The conductor size is then varied from 0.1 mm in steps of 0.001mm to assess the trigonometric function. A total of 2291 points are obtained and plotted in Figure 3.7 against the trigonometric function.

From Figure 3.7, there is a small variation of the function when the size of the conductor is less than 5mm. From 5mm onwards the curve shows a rapid increase, roughly exponential. However the critical point of this distribution is the cut-off between the plotted function and the skin depth size that occurs at trigonometric function of 0.0551. The real meaning is that the losses are enhanced by approximately $0.0551\frac{{H_{z0}}^2}{\sigma\delta}$ when the thickness of the conductor is equal to the skin depth. Nonetheless, from the practical perspective this case can only occur on the regulator winding when the edge wound conductor is used. If the regulator is designed using edge wound and situated outside of the main field i.e. after the HV winding, the assumptions may still be appropriate as a low quantity of winding eddy losses is expected.

The above analysis has shown that the assumption works well with small conductor thicknesses, once the conductor size becomes larger than 5mm the losses can be overestimated. This assumption is therefore limited to small conductor sizes.

Proceeding with the derivation, let t=2b be a conductor thickness, and substitute t into Equation 3.45 to get:

$$P_e = \frac{{H_{z0}}^2\left(\frac{\sqrt{\omega\mu\sigma}}{\sqrt{2}}t\right)^3}{6\sigma\sqrt{\frac{2}{\omega\mu\sigma}}} \qquad (3.46)$$

The above expression can be represented in terms of the flux density and as losses per unit volume according to:

$$P_e = \frac{{B_0}^2\omega^2\sigma t^2}{24} \qquad (3.47)$$

B_0 is the peak flux density.

The flux density has axial and radial components, if that is taken into account, Equation 3.47 above can be split into the respective components and perpendicular surface as:

$$P_a = \frac{{B_z}^2 \omega^2 \sigma t^2}{24} \tag{3.48}$$

$$P_r = \frac{{B_r}^2 \omega^2 \sigma h^2}{24} \tag{3.49}$$

In Equation 3.48 and 3.49, B_z is the axial flux density and B_r is the radial flux density component respectively.

Before Equation 3.48 and 3.49 are accepted and used to evaluate the winding eddy losses of the transformer, it is important that at this stage their local accuracy requirement is understood. As a result, a 2-D FEM simulation of a single conductor is performed in Ansoft Maxwell. The aim is to determine the winding eddy losses in twofold, those are to:

a) Use the mid-flux density value and apply Equation 3.48 and 3.49.

b) Use the flux density per mesh element, integrate and apply Equation 3.48 and 3.49.

With the geometry, boundary and current density values provided in Appendix A, losses are calculated using the two methods a) and b). For the purposes of the calculation of losses, the copper conductivity of 47.303 MS/m is used. This is the conductivity of the copper material as obtained at a reference temperature of 75°C as discussed in Chapter 6.

The results of the simulation are as follows:

- Using the first option a) the losses are: P_a = 3.4214 W and P_r = 0.210 W
- Using the first option b) the losses are: P_a= 3.483 W and P_r = 0.7997 W

From the simulation results presented above the difference obtained when comparing the axial component is 1.78%, meanwhile the radial component difference is 73.69%. It can be deduced that the simplification of Equation 3.49 is not adequate for the evaluation of the radial winding eddy losses. In addition, to understand this further a parametric study of how the field varies with the thickness of the conductor is shown in Figure 3.8. The table of the input values of the parameters that changed during the study is shown in Appendix A.

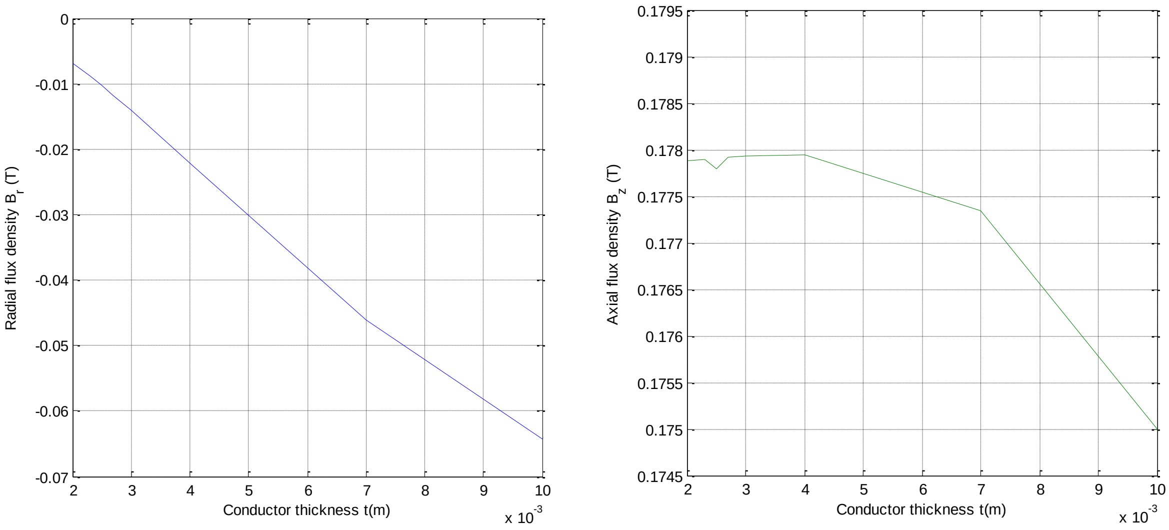

Figure 3.8: Mid flux density quantities for different conductor thicknesses

Figure 3.8 illustrates the flux density components obtained at the centre of the conductor when the thickness is changed. The first figure shows the radial flux density component as the conductor size is increased from 2 mm to 10 mm. The insignificant and abnormal dip seen at 2.5 mm is due to the uneven meshing of the model. It is observed that the radial flux is sensitive to the thickness of the conductor resulting in the flux density changing from -0.0069T to -0.0643 T. On the other hand, the axial flux changed slightly from 0.1779T to 0.1750T as observed in the second figure.

The analysis of eddy current losses using the rectangular coordinates has shown that the governing equations have limitations. The axial component of the winding eddy losses is computed with a higher accuracy when using the mid-flux density. However the radial component can have a large error, hence a large discretization is required for the radial component. In the next section the solution of the cylindrical coordinates is presented to assess if the use of rectangular coordinates is adequate in the first place.

3.5. Laplacian operations

In the preceding section the winding eddy loss equations have been established, which are founded on the rectangular coordinates of the one-dimensional solution. To assess the sufficiency of this solution, in the next sections the cylindrical solution is explored. This analysis is governed by the cylindrical representation of the Laplacian operator. The difference between the scalar and vector Laplacian is not recognized through many textbooks [44]. The lack of understanding thereof leads to many assuming that these two are easily transformed from the rectangular coordinate system to the cylindrical coordinate system. Nevertheless the vector Laplacian operation is not as comprehensible as the scalar potential; hence the fundamental differences are explicitly outlined. In addition, the eddy current problems demand that the former is properly understood; accordingly this section provides the distinction of the two expansions in differential form as contained in [44].

The cylindrical scalar Laplacian:

$$\nabla^2 V = \frac{\partial^2 V}{\partial r^2} + \frac{1}{r}\frac{\partial V}{\partial r} + \frac{1}{r^2}\frac{\partial^2 V}{\partial \varphi^2} + \frac{\partial^2 V}{\partial z^2} \tag{3.50}$$

The cylindrical vector Laplacian:

$$\begin{aligned} & a_r \left[\frac{\partial^2 A_r}{\partial r^2} + \frac{1}{r}\frac{\partial A_r}{\partial r} - \frac{A_r}{r^2} + \frac{1}{r^2}\frac{\partial^2 A_r}{\partial \varphi^2} - \frac{2}{r^2}\frac{\partial A_r}{\partial \varphi} + \frac{\partial^2 A_r}{\partial z^2}\right] \\ \nabla^2 \bar{A} = & +a_\varphi \left[\frac{\partial^2 A_\varphi}{\partial r^2} + \frac{1}{r}\frac{\partial A_\varphi}{\partial r} - \frac{A_r}{r^2} + \frac{1}{r^2}\frac{\partial^2 A_\varphi}{\partial \varphi^2} + \frac{2}{r^2}\frac{\partial A_r}{\partial \varphi} + \frac{\partial^2 A_\varphi}{\partial z^2}\right] \\ & +a_z \left[\frac{\partial^2 A_z}{\partial r^2} + \frac{1}{r}\frac{\partial A_z}{\partial r} + \frac{1}{r^2}\frac{\partial^2 A_z}{\partial \varphi^2} + \frac{\partial^2 A_z}{\partial z^2}\right] \end{aligned} \tag{3.51}$$

3.6. Eddy current solution in cylindrical coordinates

The traditional one-dimensional solution presented in preceding sections is based on rectangular coordinates and does not take the curvature into consideration. In this section Maxwell's equations are solved using the cylindrical description of the field. The work presented is derived from first principles; in addition the cylindrical solution has been presented in [3] when dealing with conducting tubes to screen the solenoid conductors. Furthermore, Figure 3.9 illustrates the winding conductor orientation in cylindrical coordinates. It is clear that the curvature needs to be accounted for with minimal assumptions. The consideration of the curvature may however lead to an intricate mathematical solution of the diffusion equation.

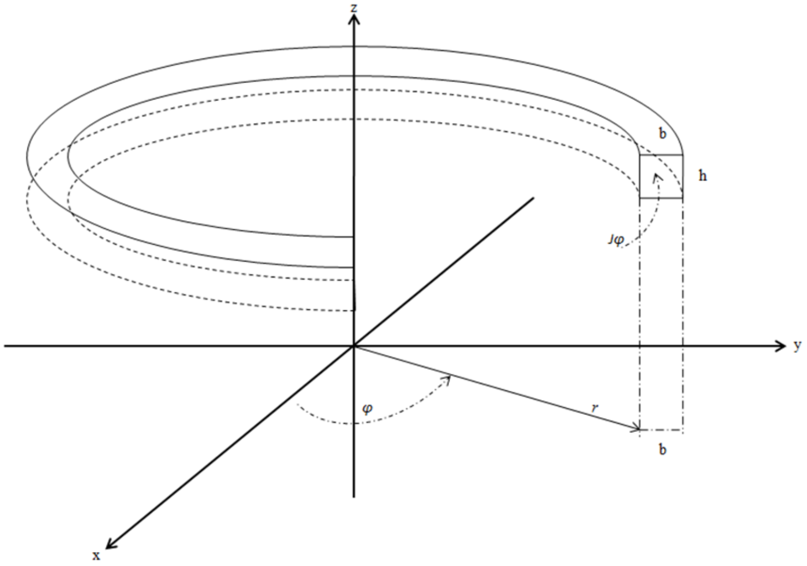

Figure 3.9: Cylindrical setup of the conductor, placed in the magnetic field

Consider Equation 3.51:

$$\begin{gathered} a_r\left[\frac{\partial^2 H_r}{\partial r^2}+\frac{1}{r}\frac{\partial H_r}{\partial r}-\frac{H_r}{r^2}+\frac{1}{r^2}\frac{\partial^2 H_r}{\partial \varphi^2}-\frac{2}{r^2}\frac{\partial H_r}{\partial \varphi}+\frac{\partial^2 H_r}{\partial z^2}\right] \\ +a_\varphi\left[\frac{\partial^2 H_\varphi}{\partial r^2}+\frac{1}{r}\frac{\partial H_\varphi}{\partial r}-\frac{H_r}{r^2}+\frac{1}{r^2}\frac{\partial^2 H_\varphi}{\partial \varphi^2}+\frac{2}{r^2}\frac{\partial H_r}{\partial \varphi}+\frac{\partial^2 H_\varphi}{\partial z^2}\right]=\sigma\mu_0\frac{\partial \bar{H}}{\partial t} \\ +a_z\left[\frac{\partial^2 H_z}{\partial r^2}+\frac{1}{r}\frac{\partial H_z}{\partial r}+\frac{1}{r^2}\frac{\partial^2 H_z}{\partial \varphi^2}+\frac{\partial^2 H_z}{\partial z^2}\right] \end{gathered} \tag{3.52}$$

The diffusion equation appears complex, in this equation the magnetic field is applied in cylindrical form using the Laplacian operation explained in Section 3.7.

However, from Figure 3.9, similar to the rectangular coordinates, it is established that the eddy current flows in the φ direction such that;$J = J_\varphi$.

It is further assumed that the magnetic field has only the z-component changing in the r-direction. Hence, it is deduced that:

$$a_z\left[\frac{\partial^2 H_z}{\partial r^2}+\frac{1}{r}\frac{\partial H_z}{\partial r}\right]=\sigma\mu_0\frac{\partial H_z}{\partial t} \tag{3.53}$$

The partial definition can be dropped since there is only the z-component of the field, rewriting 3.53 results in:

$$\frac{d^2 H_z}{dr^2}+\frac{1}{r}\frac{dH_z}{dr}=\sigma\mu_0\frac{dH_z}{dt} \tag{3.54}$$

The solution of the above diffusion equation does not have a simple general equation. For simplicity, it is essential to express this equation in the frequency domain as follows:

$$\frac{d^2H_z}{dr^2}+\frac{1}{r}\frac{dH_z}{dr}=\sigma\mu_0 j\omega H_z \qquad (3.55)$$

Let $\beta^2=j\omega\sigma\mu_0$

$$\frac{d^2H_z}{dr^2}+\frac{1}{r}\frac{dH_z}{dr}-\beta^2H_z=0 \qquad (3.56)$$

The solution of this equation satisfies modified Bessel functions of zero order [45], thus the solution becomes:

$$H_z=AI_0(\beta r)+BK_0(\beta r) \qquad (3.57)$$

A and B are arbitrary constants determined using the knowledge of boundary conditions. To explain the boundary values, Figure 3.10 is presented.

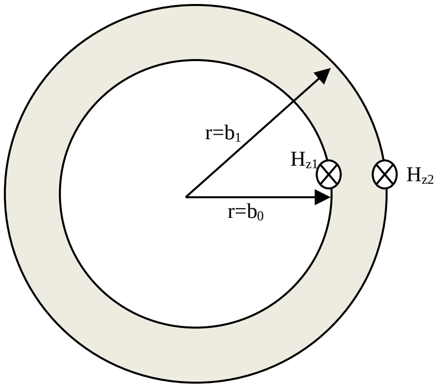

Figure 3.10: Top view of the cylindrical layout of the winding

From Figure 3.10 the boundary conditions result in Equations 3.58 and 3.59 below

$$H_{z1}=AI_0(\beta b_0)+BK_0(\beta b_0) \qquad (3.58)$$

$$H_{z2}=AI_0(\beta b_1)+BK_0(\beta b_1) \qquad (3.59)$$

Given the small thickness of the winding strands, it makes sense to assume H_{z1} equals to H_{z2} to become H_{z0}. Hence, solving Equation 3.58 and 3.59 simultaneously yields:

$$A=\frac{H_{z0}-BK_0(\beta b_0)}{I_0(\beta b_0)} \qquad (3.60)$$

Substituting 3.60 into 3.59 yields:

$$B \ = \frac{H_{z0}\ [I_0(\beta b_0) - I_0(\beta b_1)]}{K_0(\beta b_1) I_0(\beta b_0) - K_0(\beta b_0) I_0(\beta b_1)} \tag{3.61}$$

Now, it is important to obtain the solution of A:

$$A = \frac{H_{z0})}{I_0(\beta b_0)} - \frac{K_0(\beta b_0)}{I_0(\beta b_0)} \times \frac{H_{z0}\ [I_0(\beta b_0) - I_0(\beta b_1)]}{K_0(\beta b_1) I_0(\beta b_0) - K_0(\beta b_0) I_0(\beta b_1)} \tag{3.62}$$

Simplifying 3.62 results in:

$$A = \frac{H_{z0}\ [K_0(\beta b_1) - K_0(\beta b_0)]}{K_0(\beta b_1) I_0(\beta b_0) - K_0(\beta b_0) I_0(\beta b_1)} \tag{3.63}$$

Both solution constants are now shown as only dependent on Modified Bessel functions. So it becomes practical to replace them back into Equation 3.57, yielding:

$$H_{z0} = \left[\frac{H_{z0}\ [K_0(\beta b_1) I_0(\beta r) - K_0(\beta b_0) I_0(\beta r)]}{K_0(\beta b_1) I_0(\beta b_0) - K_0(\beta b_0) I_0(\beta b_1)}\right] +$$

$$\left[\frac{H_{z0}\ [I_0(\beta b_0) K_0(\beta r) - I_0(\beta b_1) K_0(\beta r)]}{K_0(\beta b_1) I_0(\beta b_0) - K_0(\beta b_0) I_0(\beta b_1)}\right] \tag{3.64}$$

Now that the solution of the field is simplified, it is required to represent Equation 3.2 in cylindrical coordinates, and solve the determinant as shown in Equation 3.65:

$$\frac{1}{r}\begin{vmatrix} i & j & k \\ \frac{d}{dr} & \frac{d}{d\varphi} & \frac{d}{dz} \\ H_r & H_\varphi & H_z \end{vmatrix} = J_r i + J_\varphi j + J_z k \tag{3.65}$$

The solution from the problem definition explained above results in the current density of:

$$\frac{1}{r}\frac{dH_z}{dr} k = J_\varphi j \tag{3.66}$$

At this stage the magnetic field solution is known. It is therefore substituted back into Equation 3.66. This solution is now in differential form and the current density is attainable.

$$J_\varphi = \frac{1}{r}\frac{d}{dr}\begin{bmatrix} \left[\frac{H_{z0}\ [K_0(\beta b_1) I_0(\beta r) - K_0(\beta b_0) I_0(\beta r)]}{K_0(\beta b_1) I_0(\beta b_0) - K_0(\beta b_0) I_0(\beta b_1)}\right] \\ + \\ \left[\frac{H_{z0}\ [I_0(\beta b_0) K_0(\beta r) - I_0(\beta b_1) K_0(\beta r)]}{K_0(\beta b_1) I_0(\beta b_0) - K_0(\beta b_0) I_0(\beta b_1)}\right] \end{bmatrix} \tag{3.67}$$

The derivative of Equation 3.67 cannot be calculated using conventional methods, hence the identities are recalled:

$$I'_v(x) = \frac{v}{x} I_v(x) + I_{v+1}(x) \tag{3.68}$$

$$K'_v(x) = \frac{v}{x} K_v(x) + K_{v+1}(x) \tag{3.69}$$

Equation 3.68 and 3.69 are derivatives of the first and second kind of the Modified Bessel functions found in [46]. The order of these expressions is represented by *v*; substituting the actual order they are:

$$I'_0(x) = I_1(x) \tag{3.70}$$

$$K'_0(x) = K_1(x) \tag{3.71}$$

It is apparent that the derivative of the zero order is equal to the first order of the Modified Bessel function for both the first and second kind.

Taking the derivative of Equation 3.67 through the combination of identities presented above yields:

$$J_\varphi(r) = H_{z0} \frac{1}{r} \begin{bmatrix} \left(\frac{[K_0(\beta b_1) I_1(\beta r) - K_0(\beta b_0) I_1(\beta r)]}{K_0(\beta b_1) I_0(\beta b_0) - K_0(\beta b_0) I_0(\beta b_1)} \right) + \\ \left(\frac{[I_0(\beta b_0) K_1(\beta r) - I_0(\beta b_1) K_1(\beta r)]}{K_0(\beta b_1) I_0(\beta b_0) - K_0(\beta b_0) I_0(\beta b_1)} \right) \end{bmatrix} \tag{3.72}$$

With the purpose of understanding the true meaning of expression 3.72, the current density is assessed with respect to *r*. This parameter is constrained within the inner radius and the thickness of the conductor. Evoking the material properties of copper that have been provided, the terms containing *r* are evaluated. Furthermore, *β* is a complex function with real and imaginary components. For the computational purposes both real and imaginary components are considered during the evaluation of the Modified Bessel functions. Now, using a Matlab calculation routine, the current density distributions illustrated in Figure 3.11 and Figure 3.12 are obtained.

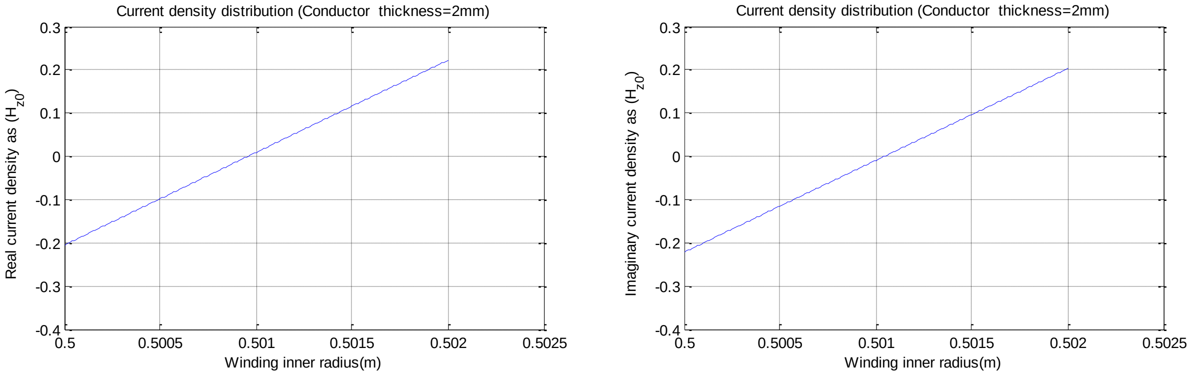

Figure 3.11: Current density distribution within a 2mm conductor

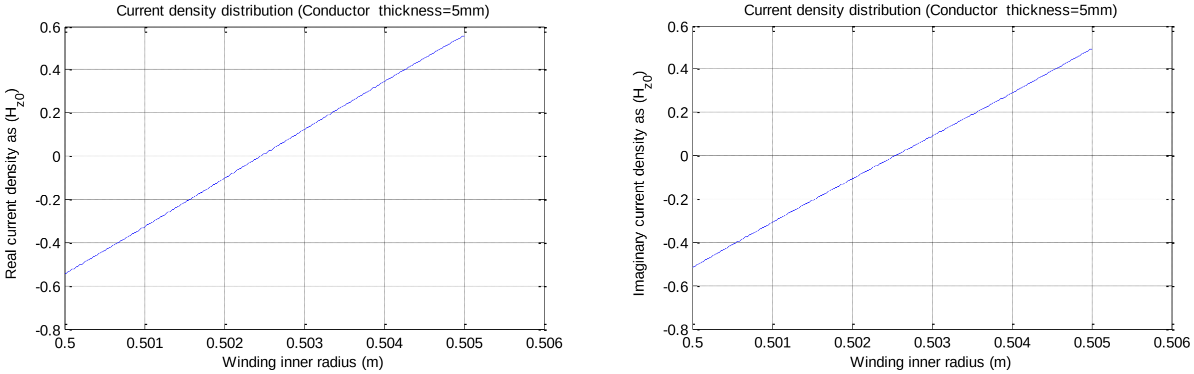

Figure 3.12: Current density distribution within a 5mm small conductor

The results presented in Figure 3.11 and Figure 3.12 are based on a 500mm winding inner radius; it is also separately proved that there is no change of the distribution when a smaller inner radius of 200mm is considered. The choice of the inner radius is due to average practical dimensions of transformer windings.

The direct proportionality between the magnetic field and the current density allows for an assessment of the current density as a function of magnetic field. Thus the 2mm and 5mm conductor sizes are analysed and the results show a linear distribution of the current density across the thickness of the conductor. The current density distribution is symmetrical and almost zero at the centre of the conductor.

The smaller conductor sizes have shown a linear distribution, however a larger sized conductor of 23mm derived from the Table 3.1 shows a periodic distribution. The latter was amplified arbitrarily by considering a 50 mm thick conductor where the distribution is obviously periodic as shown in Figure 3.13 and Figure 3.14.

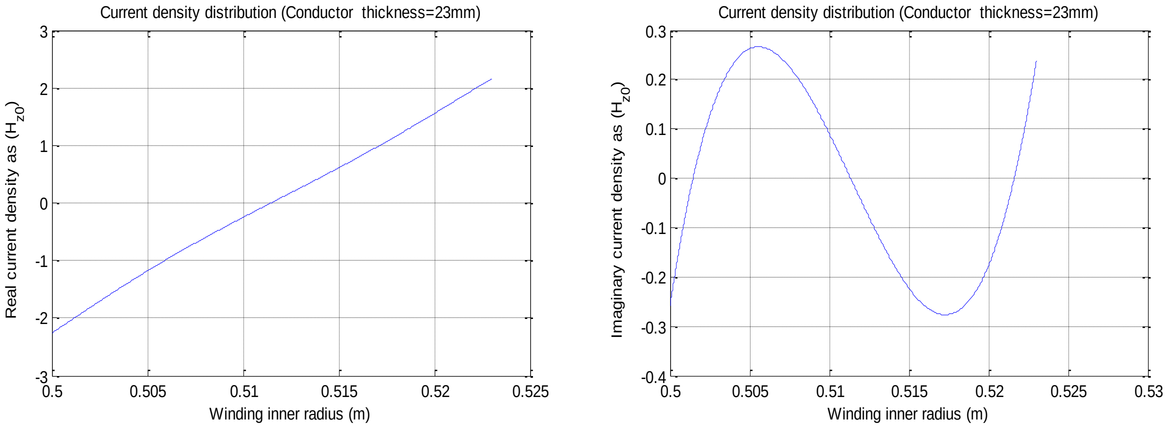

Figure 3.13: Current density distribution within large conductors (23mm)

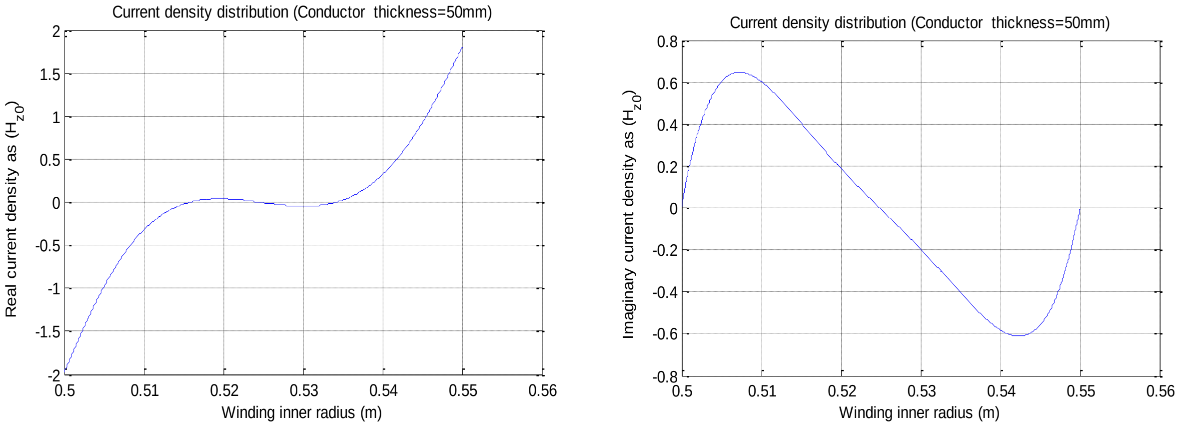

Figure 3.14: Current density distribution within large conductors (50mm)

The analysis of the different conductor sizes shows that the imaginary component decreases as the conductor thickness is increased. The real component of the larger conductor shows a rapid reduction of the current density at the centre of the conductor. This is due to the inherent skin effect of the conductor. With the complete understanding of the distribution of the current density in Figure 3.11, Figure 3.12, Figure 3.13 and Figure 3.14, the focus shifts to its relation to the formulation of the Ohmic losses defined in Section 3.3. Thus, recalling Equation 3.7 and substituting the new current density yields:

$$P_e = \frac{1}{2\sigma}\int_{b_0}^{b_1}\left|\frac{H_{z0}}{r}\left[\begin{matrix}\left(\frac{[K_0(\beta b_1)I_1(\beta r)-K_0(\beta b_0)I_1(\beta r)]}{K_0(\beta b_1)I_0(\beta b_0)-K_0(\beta b_0)I_0(\beta b_1)}\right)+\\ \left(\frac{[I_0(\beta b_0)K_1(\beta r)-I_0(\beta b_1)K_1(\beta r)]}{K_0(\beta b_1)I_0(\beta b_0)-K_0(\beta b_0)I_0(\beta b_1)}\right)\end{matrix}\right]\right|^2 dr \qquad (3.73)$$

The above equation looks tedious; to simplify it the following constants are defined:

$$C_0 = \left(\frac{K_0(\beta b_1) - K_0(\beta b_0)}{K_0(\beta b_1) I_0(\beta b_0) - K_0(\beta b_0) I_0(\beta b_1)}\right) \tag{3.74}$$

$$D_0 = \left(\frac{I_0(\beta b_0) - I_0(\beta b_1)}{K_0(\beta b_1) I_0(\beta b_0) - K_0(\beta b_0) I_0(\beta b_1)}\right) \tag{3.75}$$

Rearranging the like terms, the losses become:

$$P_e = \frac{{H_{z0}}^2}{2\sigma}\left[C_0 \int_{b_0}^{b_1} \left|\frac{I_1(\beta r)}{r}\right|^2 dr + D_0 \int_{b_0}^{b_1} \left|\frac{K_1(\beta r)}{r}\right|^2 dr\right] \tag{3.76}$$

It appears that the solution of Equation 3.76 is transcendental in a sense that it requires laborious mathematical manipulations. An attempt is made to solve it using computational platforms such as Matlab and Mathematica. This is done by computing each term as detailed below.

For further comprehension, the analysis of the integration terms is conducted. In addition, the integration of the square of the Modified Bessel of the second kind function of first order proved to be impossible in Matlab. This immediately prompted the use of the mathematically focused software, which is Mathematica. The added advantage of this software is the ability to specify the machine precision deemed sufficient.

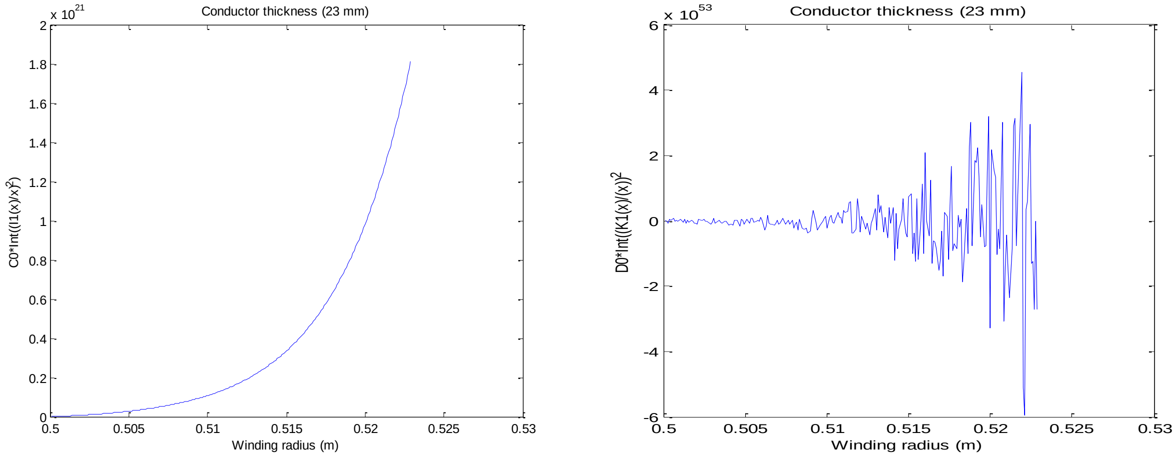

Figure 3.15: Integration of Modified Bessel functions at 500 mm radius

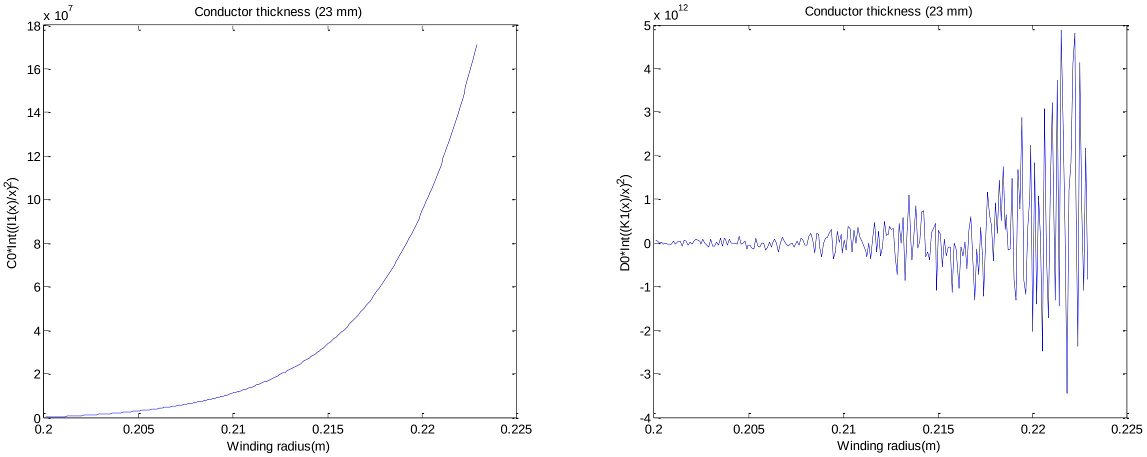

Figure 3.16: Integration of Modified Bessel functions at 200 mm radius

Using the knowledge of the maximum conductor sizes specifically the thickness; the integral terms are assessed while varying the conductor thickness. The investigation is done separately using the two inner radii values namely; 500 mm and 200 mm. It is observed from both Figure 3.15 and Figure 3.16 that the first term diverges as the conductor size increases. It is also notable that the order of the *y*-axis value reduces rapidly when the radius is 200 mm, indicating a dependency on the inner radius. The second term is also not sensible as there is visible distortion as soon as the conductor thickness exceeds skin depth. If the results were valid, the investigation similar to Section 3.4 would have been pursued.

The Author is of the view that the cylindrical approach is difficult to provide important and valid results. The anomalies suggest that this detailed approach is too complex for practical transformer applications. In addition, it is known that design routine programs significantly demand the relaxation of mathematical complexity. Hence the use of the cylindrical one-dimensional approach is not justifiable. Notwithstanding that the apparent behaviour may suggest that at smaller inner radii and conductor sizes, Equation 3.76 may be of practical use, there may be applications for this approach outside transformers. The method can in future be investigated further to quest for the identities that may simplify the integration of Modified Bessel functions.

3.7. Conclusion

This chapter focused on the derivation of winding eddy losses using rectangular and cylindrical coordinate solutions. The rigorous approach to eddy current loss computation using cylindrical coordinates has been derived. It however proves to be mathematically impractical as the integration of the Modified Bessel functions yields insoluble results.

Winding eddy loss equations obtained in Equations 3.48 and 3.49 remain the key governing equations for the computation of winding eddy losses. The two equations show that the respective loss components are directly proportional to the square of the incident flux density components. Hence, there is a need to accurately evaluate these flux density components. Furthermore there is a large error in the magnitude of 74% associated with the radial loss component. It can be deduced that the simplifications applied for Equation 3.49 are inadequate for the evaluation of the radial winding eddy losses. The integration resolution should be improved, which is done in the computation of winding eddy losses using 3-D FEM in Chapters 5 and 6. The next chapter explores in detail the method of computing the flux density components as well as selecting the method that is significant in accurately predicting the winding eddy losses.

Chapter 4

Evaluation of Rabins' analytical method

In Chapter 3, the computation formulae for winding eddy losses are established. Inherently, the winding eddy loss components are governed by the incident radial and axial flux densities. These two equations are derived from the one-dimensional behaviour of the field using rectangular coordinates which are considered adequate. The losses are proportional to the square of the incident field. Accordingly, in the event that the field is incorrectly evaluated the resulting error is squared. In this chapter, the rigorous and practical methods essential to the determination of the field quantities are explored. In particular, the analytical method is sought, this done by critically assessing known methods and juxtaposing them against the numerical method.

The method of determining the field distribution in transformers was first introduced by Rogowski. An account of his work is given by Hague [47]; a section is dedicated to the treatment of the leakage fields using this method. Rogowski was concerned with the evaluation of leakage field and reactance of sandwich windings. The leakage flux problem is treated in rectangular coordinates such that the windings are assumed long bars. The periodic distribution of the field allowed for the representation of the distribution using a single Fourier series. However, the main shortcoming of Rogowski's work is the inability to take the curvature of the windings into account.

The next person to improve the calculation of the leakage field distribution was Roth. He published a series of papers from 1927, mainly to address the leakage flux computations. His first publication dealt with the flow of heat in electrical machinery, later the mathematic similarity to magnetic problems was observed. Instead of separating the vector potential regions like Rogowski, Roth expresses the solution of the non-current carrying sections in a universal manner. This vector potential approach satisfies the double Fourier series in the *x*-*y* system. In addition, Hague praises Roth by saying that his [Roth] papers are a complete treatise which no student of these problems can ignore [47]. Interestingly, later on Hammond [50] argues that Hague commits a mistake by using the word treatise. He outlines the limitations of Roth's method, which are chiefly attributed to complex formulations.

It can be said however that Hammond's dispute of Hague's praises is unfair to a certain degree. The fact that he published his work after researchers had already advanced the subject meant added resources. One such is Billing. In 1951 [51], he published a paper to calculate the magnetic field in rectangular conductors. His solution of magnetic vector potential was based on Fourier series and Bessel functions; he therefore extended the earlier work of Rogowski and Roth. The remarks of this work include the magnetic vector potential mapped everywhere in the core window. However, the discrepancy of this method is the assumption of axial symmetry and neglecting of the curvature.

To take the curvature into account a breakthrough was witnessed in 1956, this is when Rabins advanced the calculation of flux densities using analytical methods. In addition, this method appears in the publication by Thomson [48], which seems to be earlier than Rabins. Nevertheless, the method is now known as Rabins' method, Del Vecchio et al [43] have a complete section entitled "Rabins Method for Calculating Leakage Fields, Forces, and Inductance in Transformers". The advantage of Rabins' method is the rigorous analytical approach towards obtaining the solution of the magnetic vector potential in cylindrical coordinates. This is done by expressing the solution of the field in cylindrical coordinates using Modified Bessel, Struve and Fourier series functions. In [49], Rabins presented his method primarily to calculate the leakage reactance of power transformers using digital computers.

Nowadays, computers are fast, perpetuating the need for relaxing assumptions tailored for digital computers. Meanwhile, mathematics packages such as Matlab and Mathematica come with improved libraries that include built-in functions. This chapter is focused on the implementation of Rabins' method using advanced programs; the studies of the convergence of the Fourier series are synthesized. On the other hand, the rapid development of computers has seen FEM becoming prevalent in solving electromagnetic field related problems. The commercial FEM package ANSOFT Maxwell is used in parallel to compare the results of the implementation of Rabins' method. A brief account of the work entailed here has been summarised and presented in [66].

4.1. Analytical computation of the field

Different methods of calculating the leakage field have been briefly discussed above. Amongst them, the latest and novel approach preferred for taking the curvature into account is that of Rabins'. In this section this method is dealt with rigorously, the equations, assumptions and simplifications are provided. The algorithms are implemented in the next section where the convergence of the Fourier series functions are thoroughly analysed.

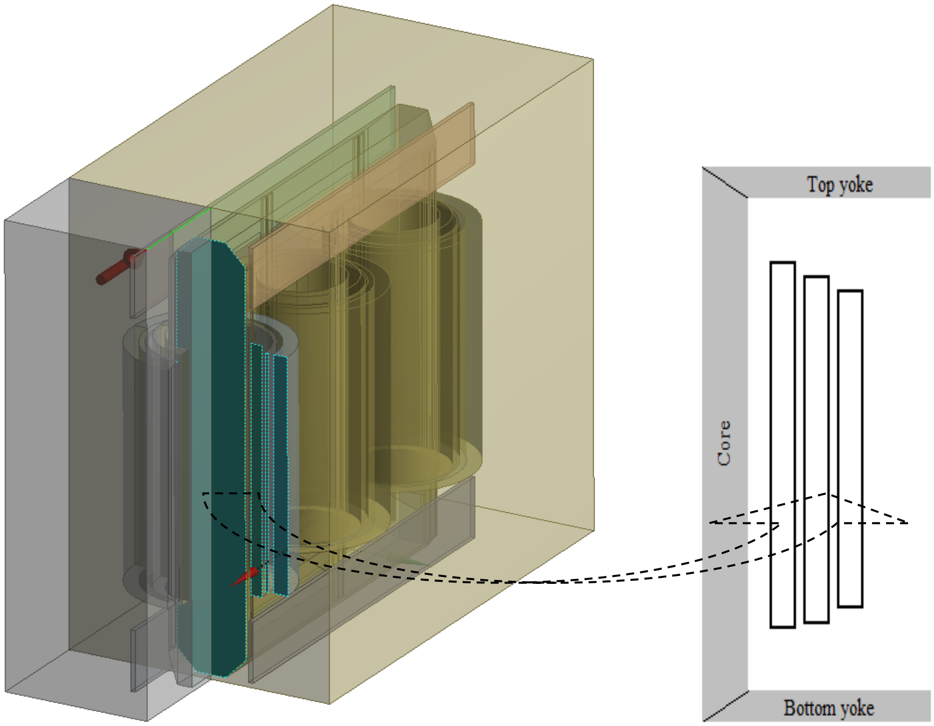

Figure 4.1: Power transformer 2-D cross sectional view

Core-type power transformer core limbs and yokes are laminated and stacked such that the resulting cross sectional area is circular in orientation. Similarly, the windings are cylinders composed of stranded copper conductors. This is the reason the simplification of the geometry inherits the axisymmetric modelling of the structure as depicted in Figure 4.1. Besides, the importance of accounting for the magnetic vector potential in cylindrical coordinates becomes evident. Rabins solves Maxwell's equations by obtaining the solution of the field using Fourier series, Modified Bessel and Struve functions. All these functions are essential to obtain a cylindrical coordinate solution of the field. In this section the theoretical derivation is discussed in detail. Maxwell equations that are fundamental to Rabins' method need to be first outlined as follows:

$$\nabla \times \boldsymbol{A} = \boldsymbol{B} \tag{4.1}$$

$$\nabla \times \boldsymbol{H} = \boldsymbol{J} \tag{4.2}$$

It is noted that both these equations have been given in the previous chapter. Thus, in this chapter only the application of each is dealt with. Now, to aid with the understanding of Rabins' method, it is important to first present this method in a flow chart format as shown in Figure 4.2.

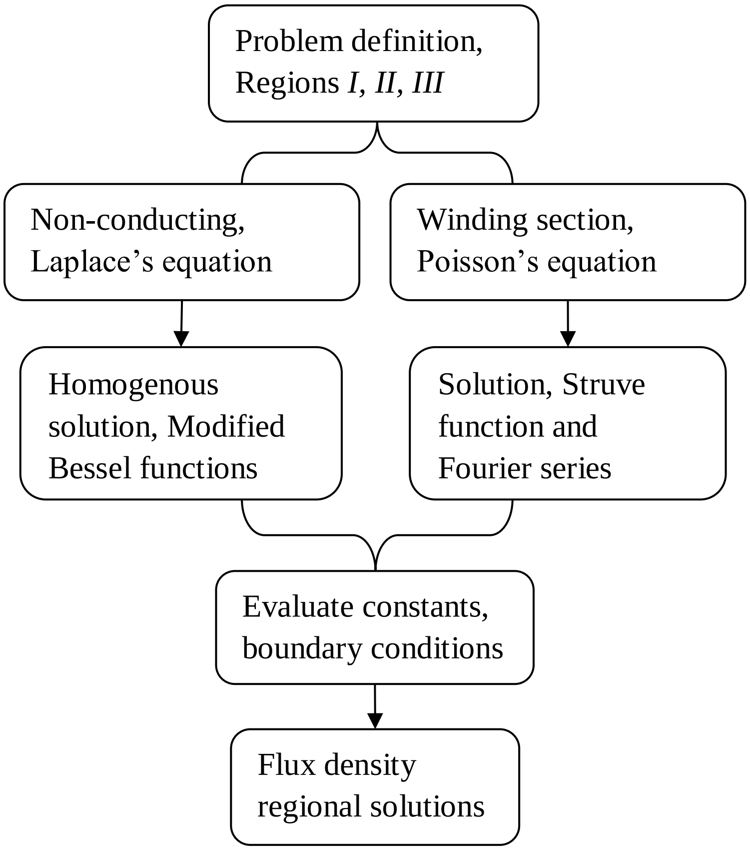

Figure 4.2: Rabins' method solution procedure

Figure 4.2 shows the typical procedure followed in the implementation of Rabins' method. As already mentioned in the introductory section of this chapter, this method is used to evaluate the leakage field between the transformer windings and subsequently the local flux density components. The first step is to envisage a cross sectional view presented in Figure 4.1. In this step the horizontal ducts and the winding that lie inside the core window are denoted as regions *I*, *II*, *III*. These regions become the cornerstone of the implementation of Rabins' method as the magnetic vector potential of each is sought.

The second step is to use the appropriate Maxwell's equations and express them in cylindrical coordinates to take the curvature into account. This step seeks to represent field equations in terms of the current density and the magnetic vector potential. At this point the field and current distributions should be visualised as conforming to periodic functions. It follows that the core and duct regions have no source current density. Hence, the two equations Laplace and Poisson are introduced.

Step three searches for the general solution of the two equations. In addition, the solution of partial differential equations of the cylindrical coordinate inherits Modified Bessel functions. In the respective regions, if there is a current source that is spatially distributed, the solution includes Modified Struve functions.

Once the equations are solved, the integration constants become the new unknowns. The boundary conditions are then used to determine these constants. Lastly, they are substituted back into the magnetic vector potential solutions of the different regions. The analytical equations are then manipulated to give the solution of the local flux density components. Lastly, most sections of this chapter are devoted to describing the individual aspects presented in Figure 4.2.

In order to accomplish the whole implementation of Rabins' method, the assumptions that constrain the behaviour of the field are required. They are particularly applied to determine the constants, these assumptions are:

- Infinite permeability of the core.
- The yokes are infinitely large.
- The ampere-turn unbalance is approximately zero.
- The effect of the tank wall and adjacent windings is negligible.

To proceed with the derivation Equation 4.1 is substituted into Equation 4.2 and combining them with the relationship between the magnetic field and flux density produces:

$$\nabla \times \nabla \times A = \mu_0 \mu_r J \tag{4.3}$$

Equation 4.3 can be expanded to obtain the following:

$$\nabla \times \nabla \times A = \nabla(\nabla . A) - \nabla^2 A = \mu_0 \mu_r J \tag{4.4}$$

Through vector operations described in Chapter 3, Equation 4.4 yields:

$$\nabla^2 A = -\mu_0 \mu_r J \tag{4.5}$$

Considering that the winding is cylindrically constructed as outlined above, it can be deduced that the current flows only in the azimuthal direction; Figure 3.9 in Chapter 3 depicts this phenomenon, hence:

$$\nabla^2 A_\varphi = -\mu_0 J_\varphi \tag{4.6}$$

In Equation 4.6 the term μ_r has been dropped because the permeability of copper is approximately 1. Furthermore, the result of Equation 4.6 is a significant one in that it postulates that the component of the magnetic vector potential required in the winding is only in the azimuthal direction, giving the expression below.

$$(\nabla^2 A)_\varphi = \frac{\partial^2 A_\varphi}{\partial r^2} + \frac{1}{r}\frac{\partial A_\varphi}{\partial r} - \frac{A_\varphi}{r^2} + \frac{1}{r^2}\frac{\partial^2 A_\varphi}{\partial \varphi^2} + \frac{2}{r^2}\frac{\partial A_r}{\partial \varphi} + \frac{\partial^2 A_\varphi}{\partial z^2} \tag{4.7}$$

The expression shown in Equation 4.7 is the Laplacian operator of the vector potential in cylindrical coordinates. In addition, the terms containing the changing magnetic vector potential in the azimuthal direction are eliminated since the solution is axisymmetric. The remaining components of the field are those that change in the *r* and *z* directions. Following this explanation, the regional solutions are diagrammatically depicted below. The aim is to clearly establish the non-current and current carrying solutions so as to distinctly represent them in an analytical manner.

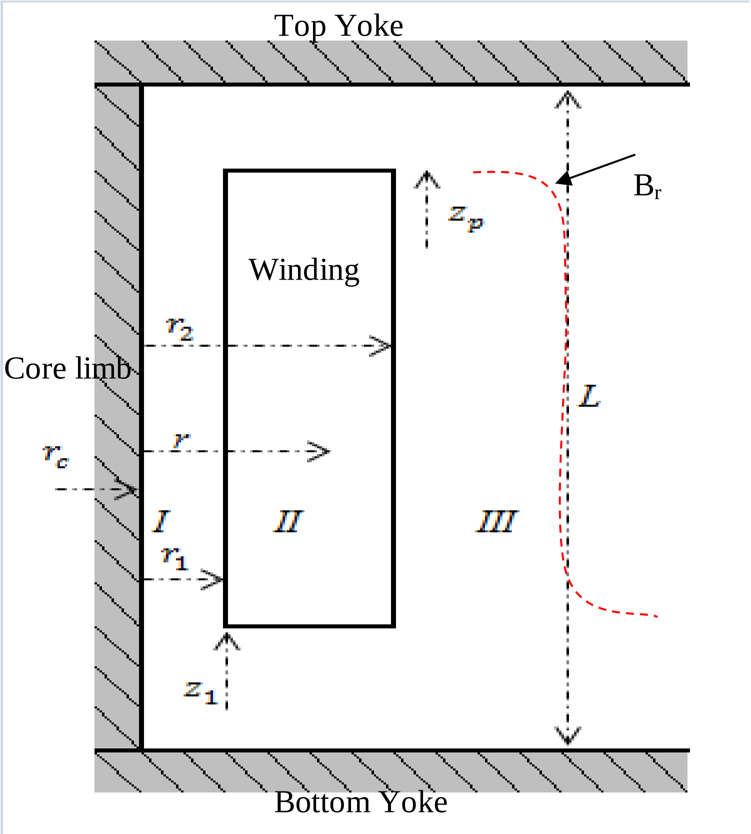

Figure 4.3: Transformer core and winding arrangement

In Figure 4.3 the following boundaries are established:

Region *I* $r_c \le r \le r_1 , 0 \le z \le L$

Region *II* $r_1 \le r \le r_2 , z_1 \le z \le z_p$

Region *III* $r > r_2 \le , 0 \le z \le L$

The classification of boundaries in Figure 4.3 and the simplification of Equation 4.6, results in the following magnetic vector potential expressions:

Region *I* and *III:*

$$\frac{\partial^2 A_\varphi}{\partial r^2} + \frac{1}{r}\frac{\partial A_\varphi}{\partial r} - \frac{A_\varphi}{r^2} + \frac{\partial^2 A_\varphi}{\partial z^2} = 0 \tag{4.8}$$

Region *II:*

$$\frac{\partial^2 A_\varphi}{\partial r^2} + \frac{1}{r}\frac{\partial A_\varphi}{\partial r} - \frac{A_\varphi}{r^2} + \frac{\partial^2 A_\varphi}{\partial z^2} = -\mu_0 J_\varphi \tag{4.9}$$

Equation 4.9 is the partial differential equation of Poisson’s form that defines the problem that Rabins is credited for solving using a mathematically manageable solution. He introduced the

Struve function term while satisfying periodic distribution. The diagram shown in Figure 4.4 illustrates the harmonic current distribution that will aid in the understanding of the problem.

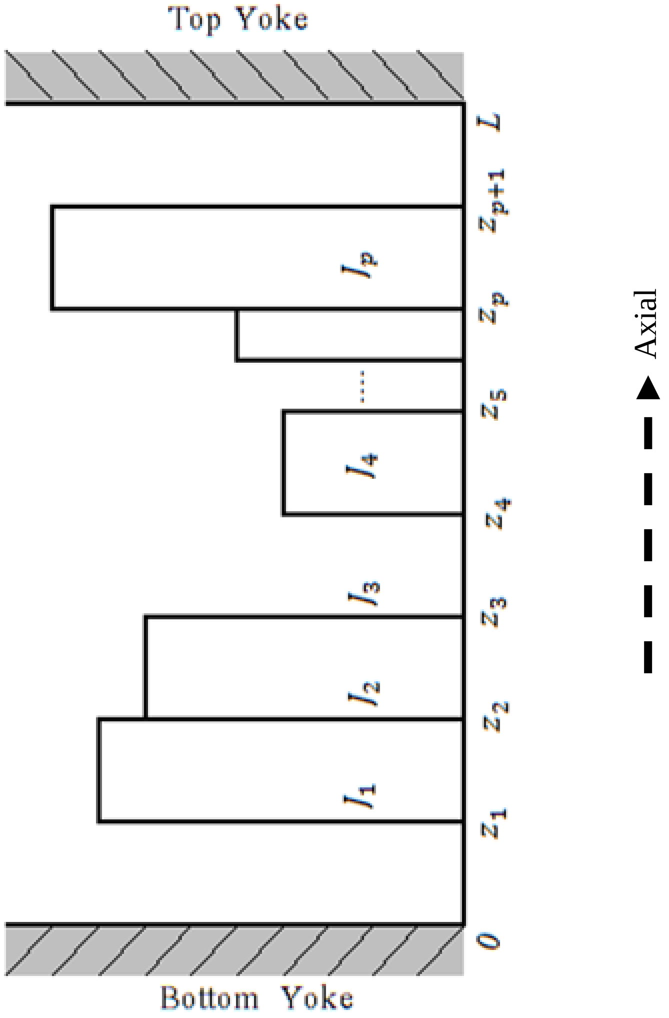

Figure 4.4: Distribution of current density along the window section

The multi-coils presented in Figure 4.4 show that in the axial direction the current distribution can be represented as a piece wise function. In addition, in Chapter 3 it is demonstrated that the distribution of the current density in a conductor is periodic. Even though the study was based on the radial direction, it is also applicable to the distribution of current in the axial direction. In this case, each coil resembles the harmonic distribution. Thus, for the practical examples used in this dissertation, it is accepted that the current distribution of a single coil satisfies the spatial formulation. The interval of this periodic representation is defined by the core window height *L* as shown in Figure 4.4. This concept is abstract and an extended explanation is found in [52]. Boyajian discusses the harmonic concept of the current density distribution in the core window of a transformer. Furthermore, the work of Rogowski is premised on sandwiched winding arrangements, where the periodic distribution of the current density is outlined. As shown in Figure 4.4, the assumption is that the current is uniform in each section satisfying:

$$J = J_0 + \sum_{n=1}^{\infty} J_n \cos mz \tag{4.10}$$

Assuming that the magnetic vector potential is distributed in a periodic manner as is the current density, it becomes:

$$A = A_0 + \sum_{n=1}^{\infty} A_n \cos mz \tag{4.11}$$

Where:

$$m = \frac{n\pi}{L} \tag{4.12}$$

In Equation 4.12, *n* denotes the index of the number of series elements equal to 1, 2, 3... The winding can be separated into numerous segments, each having a uniform current distribution. The region of interest in this analysis is *II*; and satisfies the spatial current distribution as explained above. However the solution of region I and II are first discussed.

From Figure 4.3 the regions *I* and *III* have zero source current density. Hence, the magnetic vector potential solution of this equation becomes homogenous. This further permits the expression of the product of *R(r)* and *Z(z)* as a function of separation of variables [53].

$$\frac{\partial^2 R(r)Z(z)}{\partial r^2} + \frac{1}{r}\frac{\partial R(r)Z(z)}{\partial r} - \frac{R(r)Z(z)}{r^2} + \frac{\partial^2 R(r)Z(z)}{\partial z^2} = 0 \tag{4.13}$$

Dividing by *R(r) Z(z)* yields,

$$\frac{\partial^2 R(r)}{R(r)\partial r^2} + \frac{1}{r}\frac{\partial R(r)}{R(r)\partial r} - \frac{1}{r^2} + \frac{\partial^2 Z(z)}{Z(z)\partial z^2} = 0 \tag{4.14}$$

To find the solution of Equation 4.14, the different coordinates need to be segregated. This is done by assuming that the sum of the square of a constant equals to zero. Therefore the *r* component becomes

$$\frac{\partial^2 R(r)}{R(r)\partial r^2} + \frac{1}{r}\frac{\partial R(r)}{R(r)\partial r} - \frac{1}{r^2} = m^2 \tag{4.15}$$

Subsequently the *z* term follows:

$$\frac{\partial^2 Z(z)}{Z(z)\partial z^2} = -m^2 \tag{4.16}$$

m has two possibilities i.e. *m*=0 or *m*>0, the independent solutions of *m* are therefore sought for both *R* and *Z*.

Solving for *R* when m =0 yields:

$$\frac{\partial^2 R(r)}{R(r)\partial r^2} + \frac{1}{r}\frac{\partial R(r)}{R(r)\partial r} - \frac{1}{r^2} = 0 \tag{4.17}$$

The general solution of Equation 4.17 is vastly known in the field of mathematics,

$$R_0 = ar + \frac{b}{r} \tag{4.18}$$

When *m* > 0, solving for *R* and *Z*.

$$Z = Z_m cos\,(mz + \varphi_m) \tag{4.19}$$

$$R_n = C_n I_1(mr) + D_n K_1(mr) \tag{4.20}$$

The vector potential solution of regions *I* and *II* is simplified by substituting the *R* and *Z* solutions in Equation 4.19 and 4.20 respectively and, the magnetic vector potential becomes:

$$A = ar + \frac{b}{r} + \sum_{n=1}^{\infty}[C_n I_1(mr) + D_n I_1(mr)] \cos mz \tag{4.21}$$

We change focus to the magnetic vector potential solution of region *II*, in this instance the harmonic distribution is substituted into the differential Equation 4.9. It follows that the solution satisfying Equation 4.22 is sought:

$$\mathrm{A} = \sum_{n=1}^{\infty} R_n \cos mz \tag{4.22}$$

From Equation 4.21, the *z* component immediately becomes:

$$\frac{\partial^2 A}{\partial z^2} = \frac{\partial^2 \sum_{n=1}^{\infty} R_n \cos mz}{\partial z^2} = -m^2 \sum_{n=1}^{\infty} R_n \cos mz \tag{4.23}$$

The above mathematical manipulation is necessary to eliminate the *z* component. Substituting Equation 4.23, 4.24 and 4.10 into 4.9 results in:

$$\sum_{n=1}^{\infty}\left[\frac{\partial^2 R_n}{\partial r^2} + \frac{1}{r}\frac{\partial R_n}{\partial r} - \frac{R_n}{r^2} + \frac{\partial^2 R_n}{\partial z^2}\right] \cos mz - m^2 \sum_{n=1}^{\infty} R_n \cos mz = -\mu_0[J_0 + \sum_{n=1}^{\infty} J_n \cos mz] \tag{4.24}$$

For n=0 and considering like terms yields:

$$\frac{\partial^2 R_0}{\partial r^2} + \frac{1}{r}\frac{\partial R_0}{\partial r} - \frac{R_0}{r^2} = -\mu_0 J_0 \tag{4.25}$$

Therefore the general solution becomes:

$$R_0 = ar + \frac{b}{r} - \frac{-\mu_0 J_0 r^2}{3} \tag{4.26}$$

When $n > 0$, Equation 4.24 becomes:

$$\sum_{n=1}^{\infty}\left[\frac{\partial^2 R_n}{\partial r^2} + \frac{1}{r}\frac{\partial R_n}{\partial r} - \frac{R_n}{r^2} + \frac{\partial^2 R_n}{\partial z^2}\right]\cos mz - m^2 \sum_{n=1}^{\infty} R_n \cos mz = -\mu_0 \sum_{n=1}^{\infty} J_n \cos mz \tag{4.27}$$

The orthogonality of the cosine function allows for the dropping of the Fourier series representation and Equation 4.27 is simplified to:

$$\frac{\partial^2 R_n}{\partial r^2} + \frac{1}{r}\frac{\partial R_n}{\partial r} - \frac{R_n}{r^2} + \frac{\partial^2 R_n}{\partial z^2} - m^2 R_n = -\mu_0 J_n \tag{4.28}$$

Similar to Equation 4.20, the particular solution of R satisfies Modified Bessel functions, but now a new term, Modified Struve function of order one is introduced.

$$R_n = C_n I_1(mr) + D_n K_1(mr) - \frac{\pi \mu_0 J_0}{2m^2} L_1(mr) \tag{4.29}$$

Substituting the solutions back into 4.21, the following is obtained:

$$A = ar + \frac{b}{r} - \frac{-\mu_0 J_0 r^2}{3} + \sum_{n=1}^{\infty}\left[C_n I_1(mr) + D_n K_1(mr) - \frac{\pi \mu_0 J_0}{2m^2} L_1(mr)\right]\cos mz \tag{4.30}$$

If the same approach as in Equation 4.7 is used and Equation 4.1 is evaluated, the following point flux densities are obtained:

$$B_r = -\frac{\partial A}{\partial z} \tag{4.31}$$

$$B_z = \frac{1}{r}\frac{\partial (rA)}{\partial r} \tag{4.32}$$

Thus from differentiating Equation 4.32 by parts, we get

$$B_z = \frac{A}{r} + \frac{\partial (A)}{\partial r} \tag{4.33}$$

The next step is to obtain the solution constants of the three regions as shown in Figure 4.3. Within these regions, the following field boundary conditions need to be satisfied:

- The components of the field have to be continuous at the region interface, thus
    - Flux density
        - At $r = r_1$ $B_r^{I} = B_r^{II}$
        - At $r = r_2$ $B_r^{II} = B_r^{III}$
    - Magnetic field
        - At $r = r_1$ $H_z^{I} = H_z^{II}$
        - At $r = r_2$ $H_z^{II} = H_z^{III}$
- The radial flux density component at r_c equals to zero, i.e. infinite permeability of the core
    - $\frac{\partial A_I}{\partial z} = 0$

The boundary conditions outlined above are pivotal to the determination of the solution constants. Using the magnetic vector potential solutions of the regions, the constants are evaluated; this process is extensively covered in [47],[48],[49],[50],[51],[43]. As a result, only the computational aspect of the constants is covered in this section.

To ease the mathematical representation, $x = mr$, for n =1,2,… as already defined above is used. Even though the process is not given here, eventually five constants are defined. They are C_n, D_n, E_n, F_n and G_n. These constants are mainly dependent on the geometric parameters. They are evaluated using the transformer data provided in Appendix B. In this section they are all plotted except G_n. The omission of G_n becomes obvious in the following sections. The number of terms of the series is restricted to 70 in the evaluation of constants.

$$C_n = \int_{x_1}^{x_2} tK_1(t)dt \qquad (4.34)$$

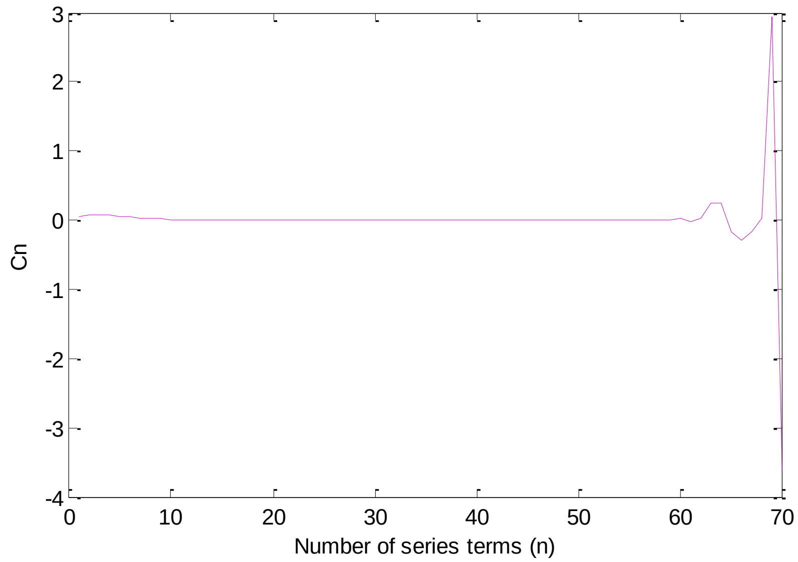

Figure 4.5: Integration of the Modified Bessel function to evaluate Cn

$$D_n = \frac{I_0(x_c)}{K_0(x_c)} C_n \tag{4.35}$$

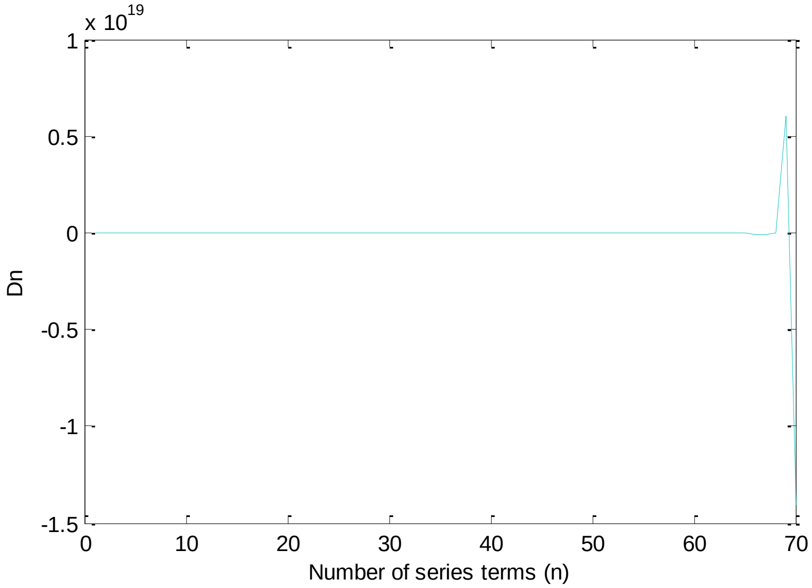

Figure 4.6: Integration of the Modified Bessel function to evaluate Dn

$$E_n = \int_0^{x_2} t I_1(t) dt \tag{4.36}$$

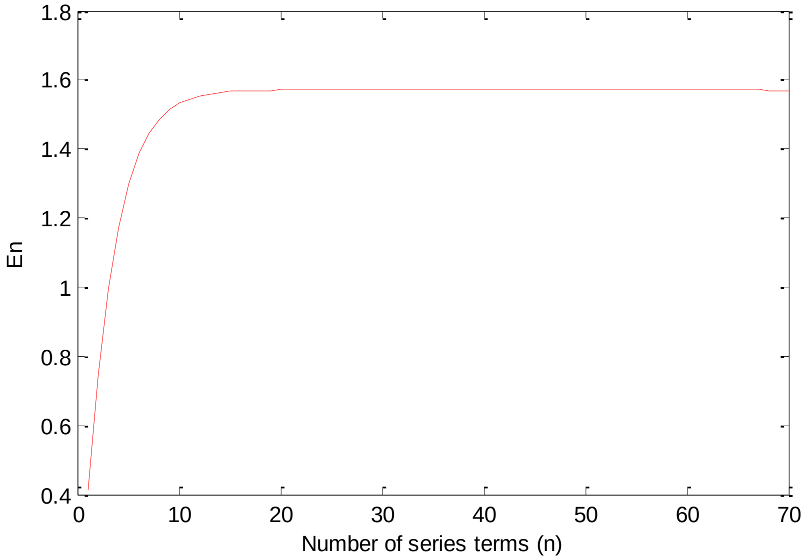

Figure 4.7: Integration of the Modified Bessel function to evaluate En

$$F_n = \frac{I_0(x_c)}{K_0(x_c)} \int_{x_1}^{x_2} tK_1(t)dt - \int_0^{x_2} tI_1(t)dt \tag{4.37}$$

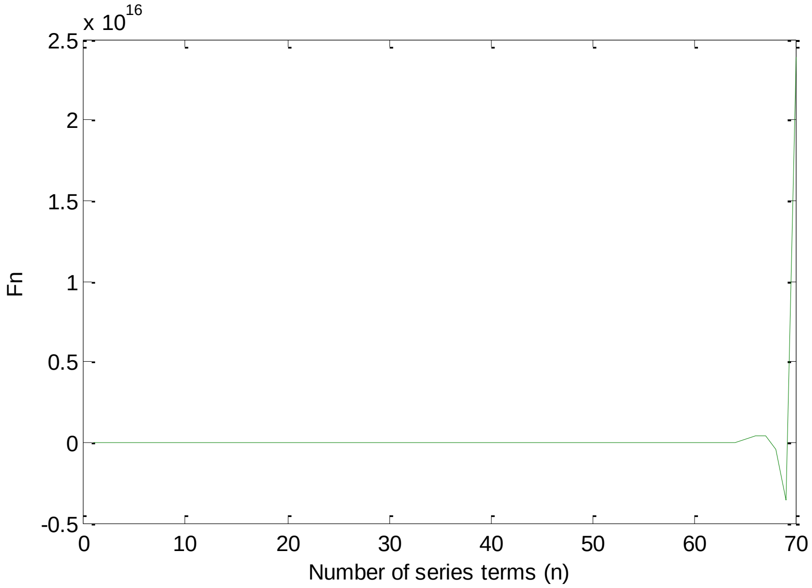

Figure 4.8: Integration of Modified Bessel functions to evaluate Fn

Of the shown constants above, C_n and E_n are observed to consist of consumable values. In particular, C_n is seen to have a smooth convergence after a few n-terms. On the contrary, D_n and F_n have very high exponent values. At this stage however these values are not of concern. The typical expectation is that these exponents get compensated for by the corresponding terms.

Having obtained and plotted the behaviour of the solution; it is a good position to determine the vector potential solutions of all the regions.

$$A_I = \frac{\mu_0 J_0 (r_2 - r_1)}{2} r + \mu_0 \sum_{n=1}^{\infty} \frac{J_n}{m^2} [C_n I_1(x) + D_n K_1(x)] \, cos(mz) \qquad (4.38)$$

$$A_{II} = \mu_0 J_0 \left(\frac{r_2 r}{2} - \frac{{r_1}^3}{6r} - \frac{r^2}{3} \right) + \mu_0 \sum_{n=1}^{\infty} \frac{J_n}{m^2} \left[E_n I_1(x) + F_n K_1(x) - \frac{\pi}{2} L_1(x) \right] \, cos(mz) \qquad (4.39)$$

$$A_{III} = \frac{\mu_0 J_0 ({r_2}^3 - {r_1}^3)}{2r} + \mu_0 \sum_{n=1}^{\infty} \frac{J_n}{m} G_n K_1(x) \, cos(mz) \qquad (4.40)$$

The flux density components are obtained from substituting Equation 4.31 and 4.33 into the simplified vector potential solutions above. The local flux density components of region *II* are given by Equations 4.41 and 4.42.

$$B_r = \mu_0 \sum_{n=1}^{\infty} \frac{J_n}{m} \left[E_n I_1(x) + F_n K_1(x) - \frac{\pi}{2} L_1(x) \right] \, sin(mz) \qquad (4.41)$$

$$B_z = \mu_0 J_0 (r_2 - r) + \mu_0 \sum_{n=1}^{\infty} \frac{J_n}{m} \left[E_n I_0(x) + F_n K_0(x) - \frac{\pi}{2} L_0(x) \right] \, cos(mz) \qquad (4.42)$$

The transformer used for the implementation of the analytical approach consists of two windings. For this situation, it is of utmost importance to realize the need to superimpose the solution for regions *I* and *II* for any point in winding A. Hence, the actual flux density value is the sum of the two solutions.

Thus the superposition of regions *I* and *II* yields:

$$B_{rsi}(r) = \frac{\mu_0 J_{1n}}{m^2} \left[E_n I_1(x) + F_n K_1(x) - \frac{\pi}{2} L_1(x) \right] + \frac{\mu_0 J_{2n}}{m^2} [C_n I_1(x) + D_n K_1(x)] \qquad (4.43)$$

$$B_{zsi}(r) = \frac{\mu_0 J_{1n}}{m} \left[E_n I_0(x) + F_n K_0(x) - \frac{\pi}{2} L_0(x) \right] + \frac{\mu_0 J_{2n}}{m} [C_n I_0(x) + D_n K_0(x)] \qquad (4.44)$$

The two equations presented above are important in this chapter; as the next section discusses how they are implemented in a computer program.

4.2. Rabins' algorithm implementation

The derivation of Rabins' method has been discussed in the preceding section, now this algorithm needs to be implemented in mathematical programs. At the time Rabins developed the method, he used digital computers to evaluate the Fourier series expansion terms. With awareness of convergence limitations, asymptotic approximations were introduced to correctly approximate Modified Bessel and Struve functions. Today, a variety of computational platforms are available, the discussion in this section is focused on using two platforms namely; Matlab and Mathematica.

The initial attempt to implement Rabins' algorithms was initiated in Matlab where Modified Bessel and Struve functions were evaluated as part of the Fourier series expansion. This package however proved to be insufficient in terms of controlling the number of digits of precision of the solution. The main observations include divergence when high order harmonics of the Fourier series expansions are considered. Terms exceeding forty were already showing divergence. The main cause of this phenomenon is the outward calculation approach inherent to Matlab operations. In this instance, the precision is sequentially lost in every execution step. This dependence immediately prompted a need for a more robust platform; with a flexible number of digits of precision.

From the above explanation, the package available to explore the precision requirements is Mathematica. In this section the implementation of Rabins' algorithms is entailed. The effect of the number of digits of precision versus accuracy is extensively analysed. In addition, the number of terms sufficient to obtain convergence is rigorously assessed.

The geometry dimensions and characteristics of the transformer used for the study are provided in Appendix B. This transformer is used throughout the chapter for all comparisons.

4.2.1. Assessment of the number of digits of precision

The flux density components are calculated at the centre of the radial position (fixed) of the winding. Along the winding height, the axial position is increased in step increments equal to the conductor height in order to discretize the winding into several strands of centroid coordinates.

In determining the sufficient number of digits of precision an assumption of 70 Fourier series elements is considered. The assumption was also made by Kulkarni [9]; he states that the mentioned number suffices, notwithstanding the detailed validation in the next section. The number of digits of precision is increased in steps of 10 starting from 10 to 50. Subsequently, the flux density components are evaluated.

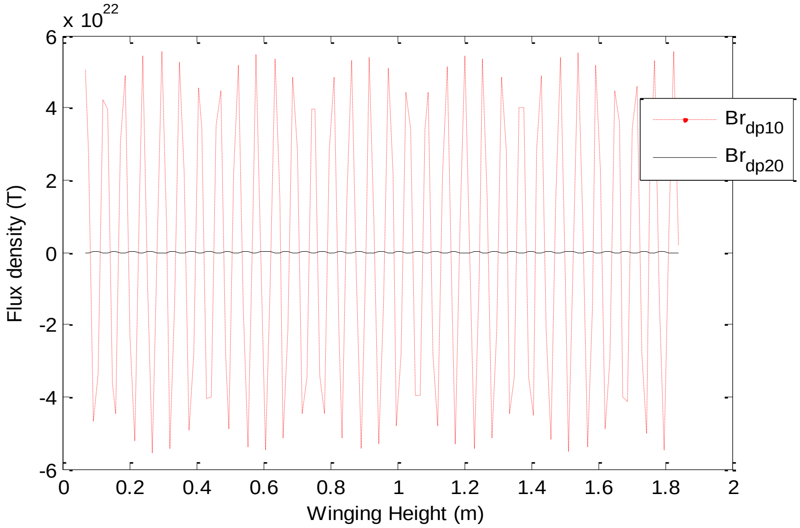

Figure 4.9: Radial flux density distribution of precision digits ranging from 10 to 20

The precision dependent solution of the radial flux density presented in Figure 4.9 is obtained when two digit precision cases are simulated, they are 10 and 20. A waveform that is sinusoidally distributed along the winding height is observed. When the number of digits of precision is set to 10, the magnitude is in the order of 22, and reduces to 16 with 20 digits. Therefore it can be said that the results obtained from fewer digits of precision are not of any use. The number of digits of precision is further increased in steps of 10, from 20 to 50. This increase slowed the convergence, resulting in a much longer simulation time.

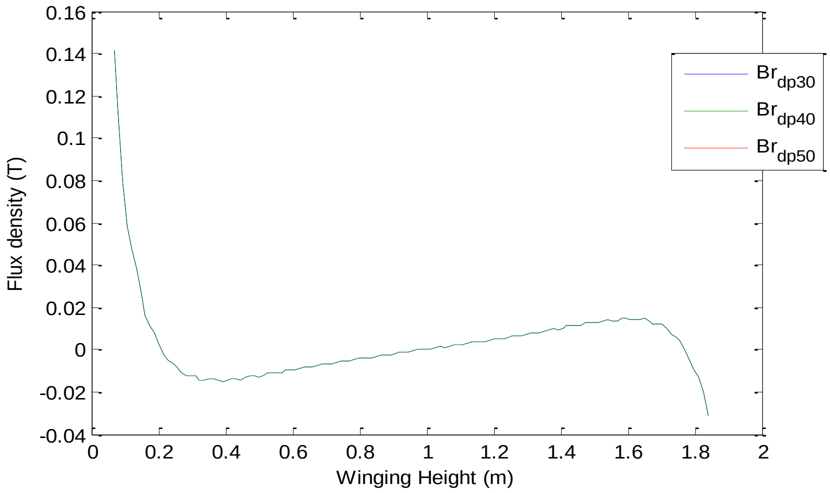

Figure 4.10: Radial flux density distribution of digits ranging from 30 to 50

The increase of the number of digits of precision from 30 to 50 showed practical results. The magnitude of the calculated flux density values reduced to more reliable results. It is noted that there is no fundamental change of waveform shape as the precision is increased further. To ensure that the obtained results are not coincidental, the axial flux density components are studied separately below.

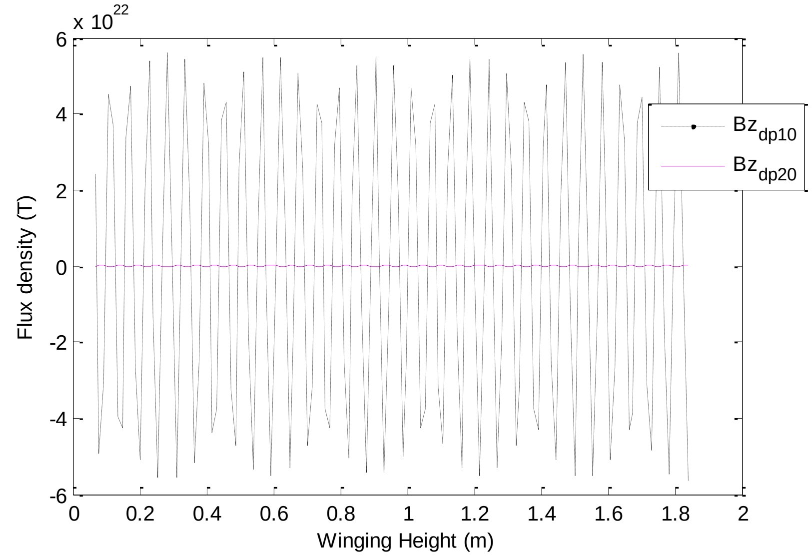

Figure 4.11: Axial flux density distribution of digits ranging from 10 to 20

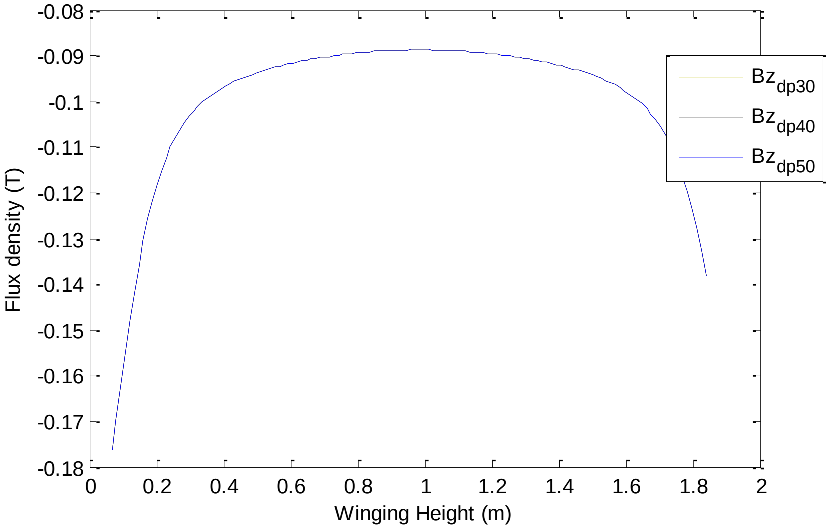

Figure 4.12: Axial flux density distribution for precision digits ranging from 30 to 50

In Figure 4.11 and Figure 4.12, the number of digits of precision is changed in the same manner as was done for the radial components. Varying the number of digits of precision from 10 to 50 yields the same behaviour. The important conclusion is however, that there is an exponential relationship between accuracy and the number of digits of precision. This relationship can be regarded as being directly proportional in the physical/ practical sense. This condition has shown to be true for the number of digits of precision less than 30. In addition, the radial and axial flux density components are exactly the same for the number of digit of precision larger than 30 as seen in Figure 10 and Figure 4.12. This result emphasizes the need to ensure that the valid number of digits of precision is known. The next subsection deals with the comparison of the number of Fourier series terms against accuracy.

4.2.2. Number of series terms

It has been discussed how the number of digits of precision affects the magnitude of the flux density values. Despite the previous assumption of regarding 70 elements as being sufficient, it is important to understand the region of confidence when working with this number. It is known that the number of elements of the series directly affects the computational speed. The advantage of knowing the maximum number is that it accelerates the implementation.

In a mathematical sense, the optimal number of elements can be established using the derivative of the function. If the subject of the field equation is *n*- terms and the derivative is equated to 0, the maximum number is attainable. However, in view of the Fourier series equations being mathematically abstract, the derivative route would introduce unnecessary difficulties. It is for this very reason that the practical approach is adopted. In a similar setup to the examination of number of digits of precision, the number of terms is studied. This number is increased from 10 to 70, and the radial and axial flux densities are recoded. A precision of 32-digits is used for all the cases.

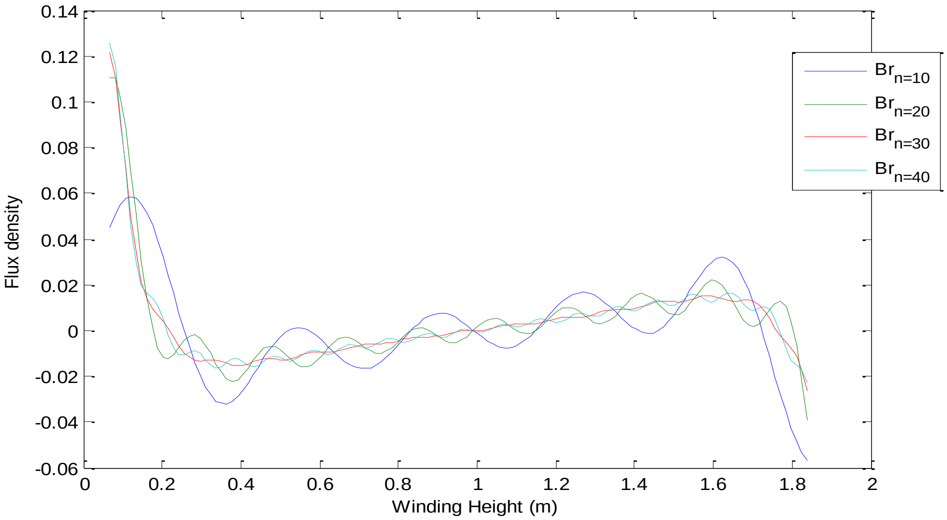

Figure 4. 13: Radial flux density distribution when the number of terms varies from 10 to 40

The above figure shows the result of having a 10 to 40 number of terms. The main reason the results are presented in segments is the enhanced visualization. The numbers of terms drive the harmonic distortion of the field distribution. When 10 elements are used the distortion is even more visible.

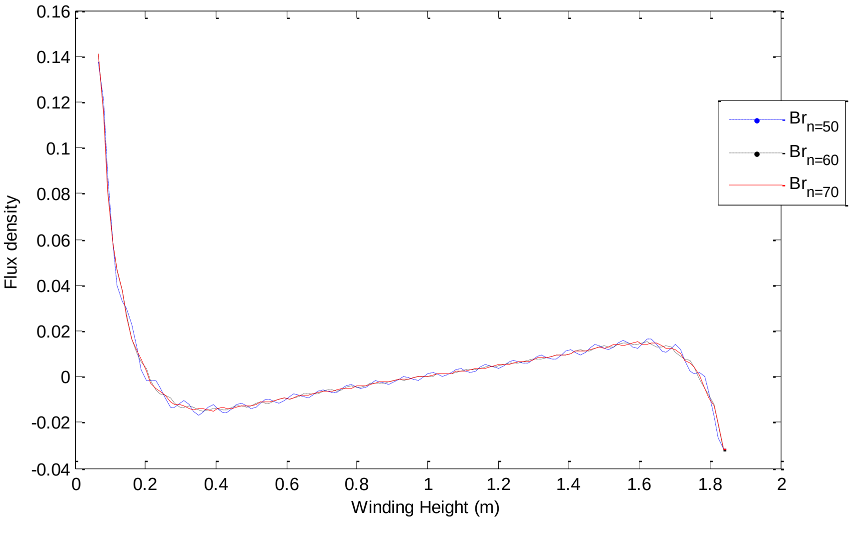

Figure 4.14: Radial flux density distribution when the number of terms varies from 50 to 70

As soon as the terms reach 50 as shown in Figure 4.14 the ripple effect reduces rapidly. With 60 to 70 elements, it is seen that the results are completely settled. The use of 70 elements during the assessment of number of digits of precision is therefore justified. To ensure that the number of the convergence seen is not component dependent, the axial flux density distribution is also tested.

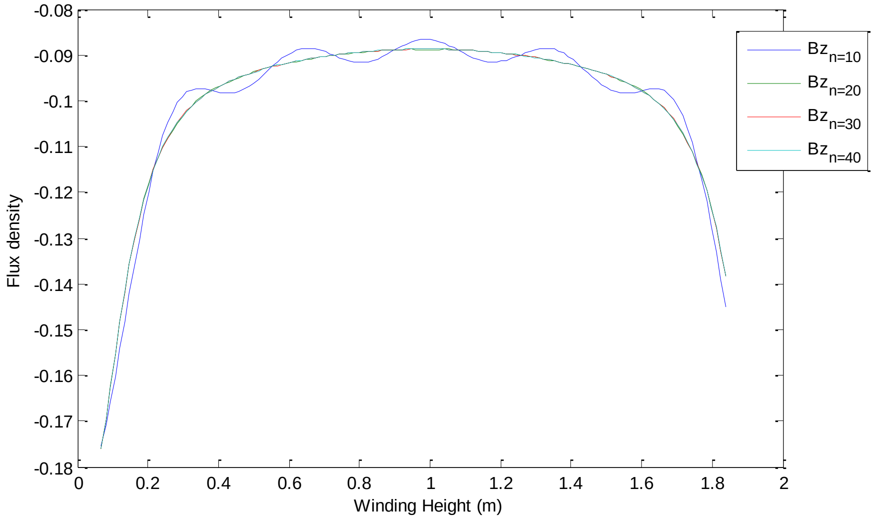

Figure 4.15: Axial flux density distribution when the number of terms varies from 10 to 40

The axial flux density distribution is similarly affected by the number of terms of the Fourier series chosen. Although, the effect is less noticeable compared to the radial flux density distribution. According to Figure 4.15, the harmonic distortion is less visible after 30 elements.

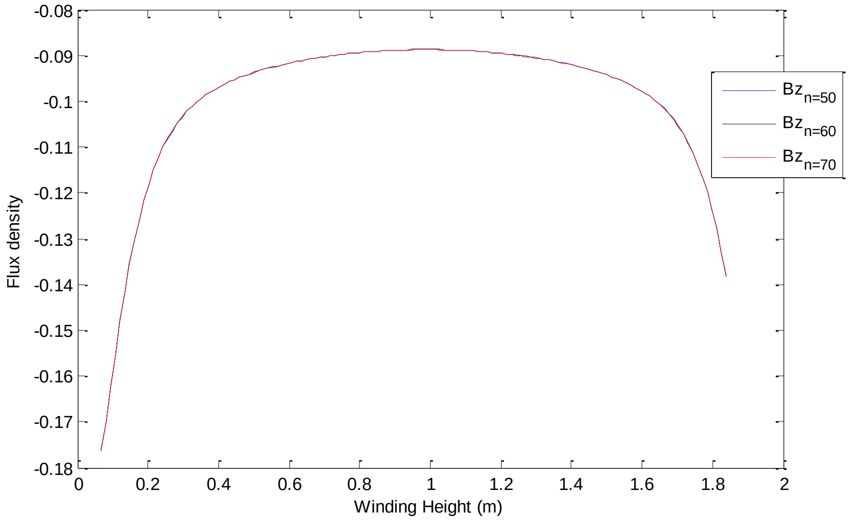

Figure 4.16: Axial flux density distribution when the number of terms varies from 50 to 70

In Figure 4.16, the analytical solution is already stable from 50 elements onwards. As the three conditions are presented in a superimposed manner, it is not easy to distinguish between the three plots. The results match exactly from these three conditions. Through the detailed implementation of Rabins' method in Mathematica, the definite number of digits of precision and the number of series terms are established. The 32-digits and 70 elements of the respective parameters discussed above are further tested later in the discussion section. The next section contains the use of the numerical method to determine field quantities.

4.3. Numerical approach

In the preceding section the analytical method has been implemented and the flux density computed. The numerical results presented in this section are obtained from a simulation model conducted in the commercial FEM software Ansoft Maxwell 14.0. In this program, the eddy current simulation type is configured with the operating frequency of 50Hz. The geometry model is similar to the one used in the previous section. The setup of this geometry is specified to be axisymmetric. The geometric model parameters of this simulation and the loading data are provided in Appendix B.

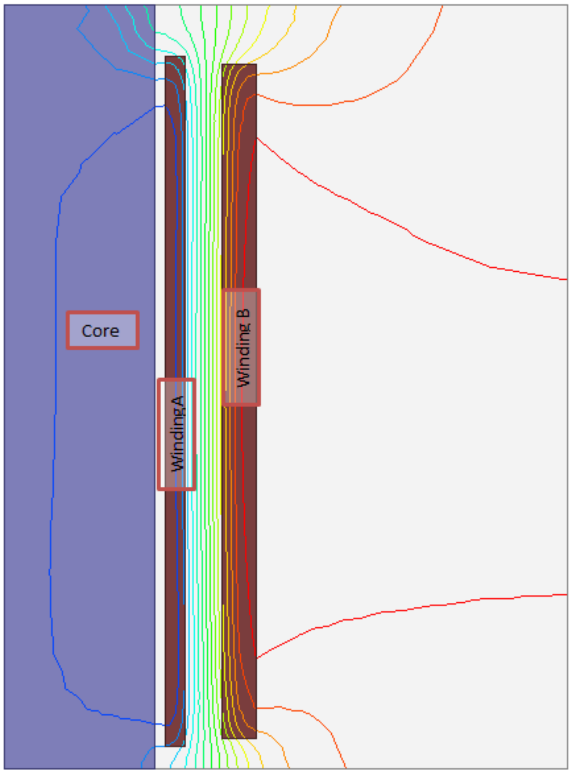

Figure 4.17: Maxwell simplified geometry model

In Figure 4.17, the transformer geometry is modelled; the 2-D cross-sectional view shows the number of windings taken into account. The two windings are of different types. From the core they are of helical and disc type respectively. The conductor types are continuously transposed cable (CTC) and strip conductors for Winding A and B respectively.

During the simulation, the windings are geometrically constructed as solid blocks, albeit configured to be stranded. This ensures that the eddy currents are not taken into consideration; otherwise the model would require that the geometric detail be at the strand level. This modelling approach is adequate since the attention is placed on evaluating the leakage field.

Given the number of discrete points of the field quantities required, a routine is developed. The field quantities are therefore obtained from a parameterized model, one such is described in [8]. This automated process was written in Matlab. The centroid coordinates of all strand positions are calculated from the knowledge of strand dimensions. The matrices containing flux density components (r and z) in each strand position are extracted from the model. The flux density components obtained from the above numerical method are then compared to the results obtained using Rabins' method. The accuracy is investigated with the change of winding height to core window height ratio.

4.4. Results discussion

The analytical method has been implemented in Mathematica in Section 4.3. The number of digits of precision and the number of the Fourier series terms have been investigated. The 32-digits and 70 series terms proved to be sufficient for the computation. The simulation of the implementation of the algorithms in Mathematica took approximately 15 minutes. To accelerate the simulation time, parallel computing consisting of 16 kernels was configured.

In this section the analytical results are compared to those of FEM when computed at similar positions. The FEM package utilized for the numerical results uses an adaptive solver. This requires that the maximum number of convergence passes be set. Hence, the results compared with analytical method were obtained after 14 passes. After each pass, the mesh elements are increased by almost 30 per cent.

When implementing the numerical method under the stringent convergence criteria mentioned above, the total simulation time was 32 seconds. This time can be broken down into initialization, solving, and post-processing; with each process lasting 12, 16 and 4 seconds respectively. The results obtained from both the analytical and numerical methods are shown below; the axial and radial components are plotted in different figures.

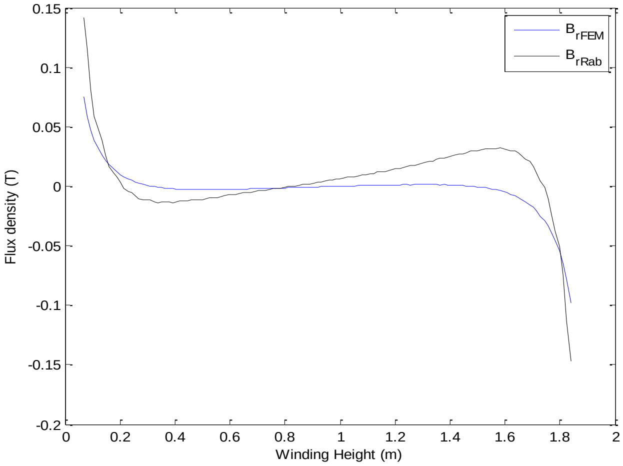

Figure 4.18: Radial flux density from FEM and Rabins' method

In Figure 4.18, the radial flux density components evaluated using FEM and Rabins' methods are shown. The flux density values of winding A are plotted across the winding height with 132 discrete points. It is clear from the diagram that the fundamental distribution of the field for both methods is periodic with similar profiles. However, the magnitude differs. The maximum for FEM is 0.1 T, while Rabins yields 0.14 T. This difference is large and may result in the overestimation of the winding hot-spot factors when losses are calculated.

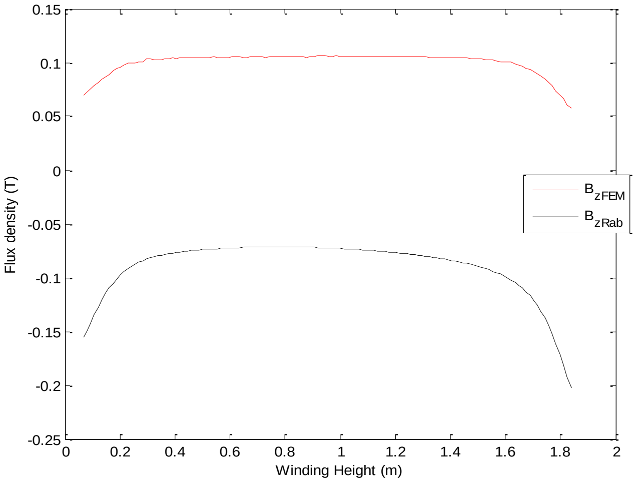

Figure 4.19: Axial flux density from FEM and Rabins' method

The axial flux density in Figure 4.19 shows a spatially distributed profile similar for both methods. From this figure, the analytical method has an off-set with respect to the numerical results. There is no known source based on the mathematical algorithms that can be identified at this stage as the cause for this phenomenon. In terms of accuracy, the percentage of the local values is not likely to provide a clear understanding. The values dealt with are small and a comparison of the percentage difference is not coherent. Furthermore, an investigation of Rabins' implementation and robustness follows and the effect of the winding height is assessed.

For further understanding of the implementation of Rabins' method, the winding height to core window height ratio is varied and the results are recorded. Five simulation cases were established by changing the yoke dimensions shown in Table 4.1.

Table 4.1: Winding height cases

Dimensions	Case 1	Case 2	Case 3	Case 4	Case 5
TY Distance (mm)	115.5	96	76.5	39	0
WH (mm)	1824	1863	1902	1941	1980
BY Distance (mm)	40.5	21	1.5	0	0
WH/L	0.921	0.941	0.961	0.980	1

The simulation cases presented in Table 4.1 were simulated in FEM and Mathematica. For the first four cases, only one case is reported which is Case 2. This is because the computational aspect did not change significantly. The results of Case 5 became interesting as the mathematical expectation differs from the numerical solution. As the field quantities are determined, the simulation time of 70 elements took approximately 25 minutes for each case. The field quantities of Case 2 and Case 5 are presented on the graphs below.

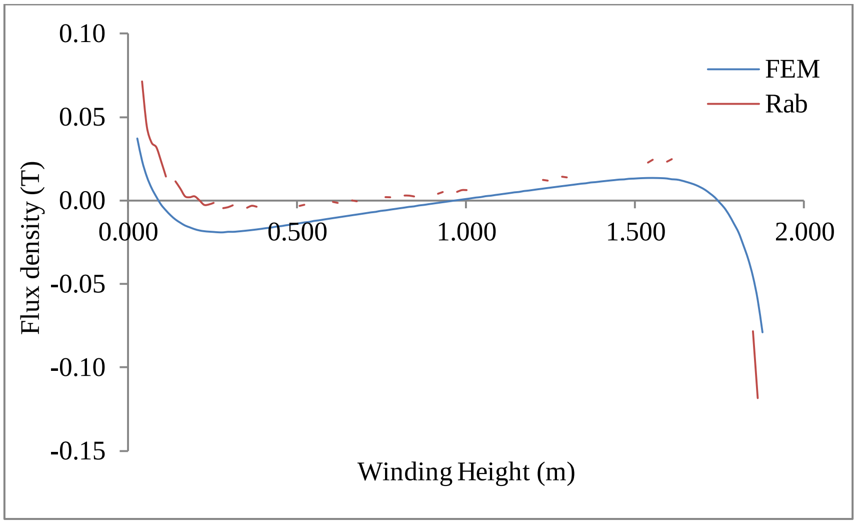

Figure 4.20: Radial flux density distribution of Case 2

The sluggish convergence experienced is attributed to insufficient number of digits of precision used. Therefore the earlier assumption of 32-digits being adequate does not hold for all cases. The results of the simulation returned a matrix with a mix of high exponent values. These were discarded to make a comparison of only valid data due to numerical instability of Rabins' method. This is evident in Figure 4.20; the discontinuities seen are due to the removal of invalid data. However it is observed that the fundamental shape of the distribution is sustained.

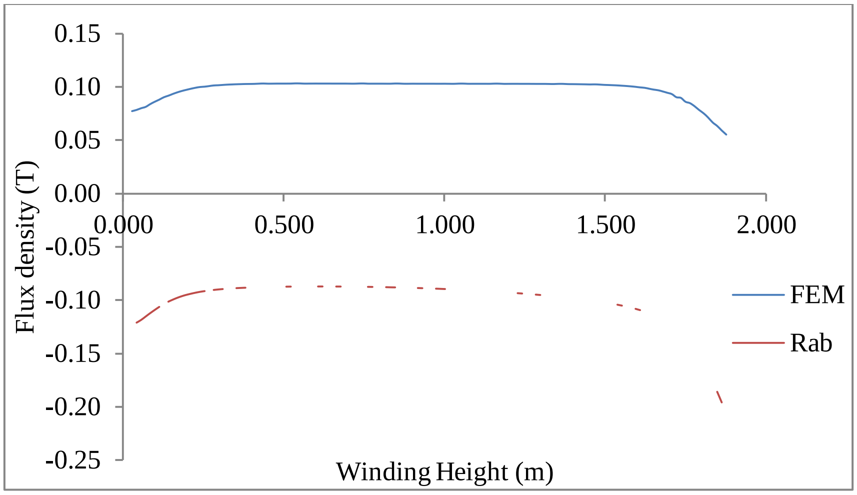

Figure 4.21: Axial flux density distribution of Case 2

The axial flux density results of Case 2 in Figure 4.21 are no different to the radial field distribution in terms of discontinuities. It is observed that the off-set of the magnitude persists. But, in pursuit of understanding the cause, the Case 5 results are expected to share important insight.

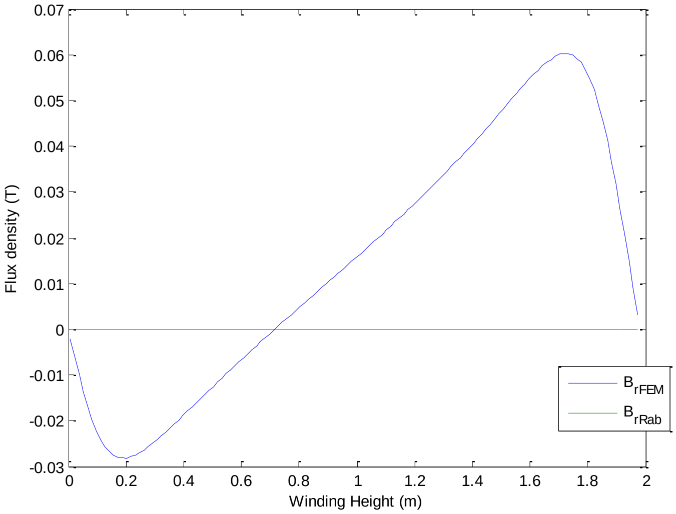

Figure 4.22: Radial flux density distribution of Case 5

The special case amongst all the cases is Case 5. The winding height is equal to the core window height. Mathematically, the periodicity falls away as the current distribution is governed by the dc term. This leaves only the axial component of the field.

The analytical solution in Figure 4.22 shows that the aforementioned mathematical behaviour is achieved. The radial flux density is flat at 0 T along the winding height. However, the numerical method result shows that the radial flux density does not become 0 T. The maximum flux density obtained is 0.06 T. The difference of these results to the ones previously achieved is the positions of the maxima along the height. Traditionally, the maximum radial fields are obtained towards the winding ends, which is not the case here. It is therefore proposed that the main cause of the effect is the adjacent winding. Since the analytical solution does not take into account the geometric influence of the adjacent winding, it is not easy to capture this profile analytically.

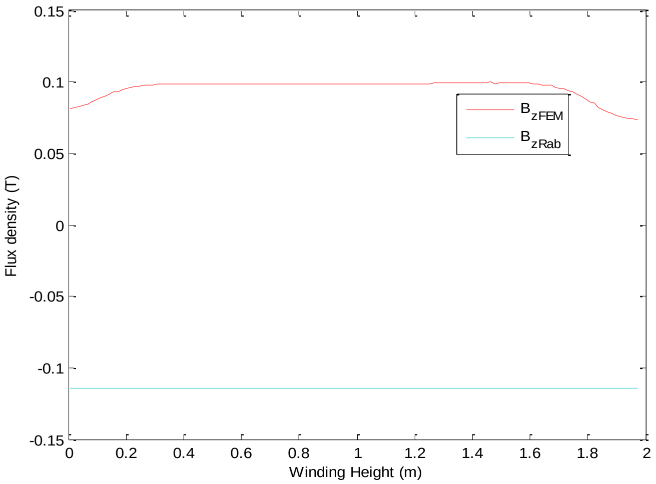

Figure 4.23: Axial flux density distribution of Case 5

From Figure 4.23 above, the axial flux density is constant at -0.114 T. This satisfies the orthogonality of the field on the boundaries of the yokes. The same cannot be said from the FEM results as the field is not constant along the height. The explanation of this cause has been provided above on the radial flux density account. Moreover, the magnitude difference between the numerical and analytical results is of concern. The definition of the current direction may be the cause; in the implementation of the analytical method, the current of the winding has a negative polarity. Figure 4.24 depicts the flux density with the results of the predicted off-set of 0.2 T.

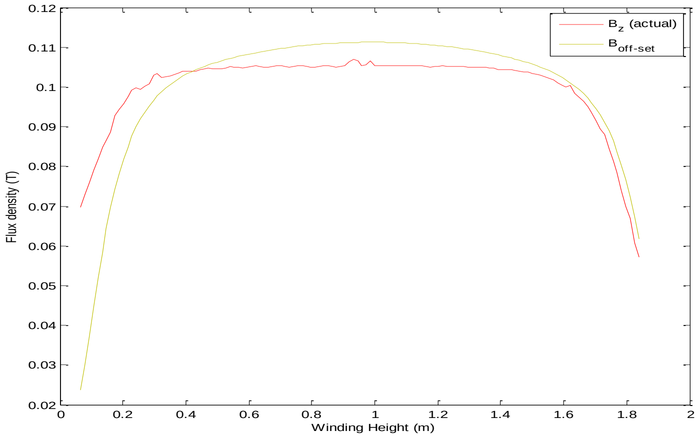

Figure 4.24: Assessment of the off-set for axial flux density distribution

The axial flux density distribution of the results presented so far shows a consistent off-set, even the simple dc case shown in Figure 4.23. It is therefore important to understand the origin of this off-set. Through a random search of possible dc off-set from the multitude of results shown in this section a value of 0.2 T is established. Furthermore, the results shown earlier in Figure 4.*19* are used to examine the accuracy of the off-set illustrated in Figure 4.24. From these results, the minimum error achieved with the off-set of 0.2 T is 0.32%, while maximum is 10.905 %.

From the set of results presented, the exact number of digit of precision is not known; however it is proven that it should be more than 32-digits of precision. Also it has been shown that this number can be influenced by the geometric dimension, such as the variation of the limb height that was assessed. This makes it difficult to define the exact number of digits of precision that satisfies a large range.

4.5. Conclusion

The implementation of the leakage field computational methods showed that the numerical method is accurate, flexible and fast. This makes the numerical method a preferred method that transformer designers should rely on for calculating leakage fields.

For the analytical method, the number of Fourier series terms should at least exceed 50 to obtain meaningful results. In addition, more than 32-digits of precision are required to successfully implement Rabins' method. The stability of the analytical method is dependent on the transformer geometry, with the winding height to core window height ratio influencing the results significantly.

Lastly, the leakage flux patterns obtained using Rabins' method and FEM compared well, thus justifying the relevance of Rabins' method in the modern environment. Although, it is seen that the implementation of Rabins' method is tough and mathematically abstract, lower level programming platforms can be used to improve the speed. Rabins' method results are used to compare the winding eddy losses in Chapters 5 and 6 to validate the 2-D FEM results.

Chapter 5

Core window effect on the calculation of winding eddy losses

In the previous chapter, different aspects of the computation of the leakage field quantities that are significant to the calculation of winding eddy losses are presented. It is clear that the numerical model approach is robust, flexible and fast for two-dimensional transformer models. The common practice in modelling transformers for loss calculations in transformer windings involves two-dimensional methods which are implicitly accepted as accurate [54]. However, the two-dimensional modelling approach of a transformer does not entirely represent the field distributions in all areas of the transformer winding. This chapter assesses the distribution of the flux density components around the winding circumference. It further quantifies the effect of this distribution to the winding eddy losses.

In most practical designs, sections of the winding conductors are situated on the inside and the others on the outside of the core window. The situation is such that the windings are subject to different leakage field levels. In this chapter, this phenomenon will be referred to as the “core window effect”. The only methodologies able to account for this effect should have capacity to model the complete three-dimensional structure of the transformer.

The methods presented so far for calculating winding eddy losses are inherently applicable to the

2-D axisymmetric model, involuntarily neglecting the core window effect. As indicated earlier, this is because most transformer manufacturers find it easy to embed this calculation methodology in their design routine programs. Most solvers of these programs are configured to conduct simulation in the axisymmetric and planar domains. Kulkarni et al [8] developed such a routine; although there are other handfuls of such unpublished programs. Moreover, there is an abundance of 2-D FEM packages that are freely or commercially available.

Several authors have used three-dimensional methods to determine winding eddy losses. For an instance, Saley et al [7] developed a 3-D program to calculate the three-dimensional field using the integral equation techniques. Also, Girgis et al [55] performed field measurements in the windings of a shell-form transformer. Their aim was to verify the three-dimensional tool they had developed earlier [56]. What is common amongst these attempts is the failure to comment on field distribution around the circumference of the winding.

Waters [57] conducted a practical experiment to evaluate the radial field for the calculation of axial forces. He commented that the radial field inside the window is 20 to 50 % greater than the mean value. However, his comments are limited only to the measured radial field components. In addition, there is no other known published work on the critical analysis of the core window effect.

The purpose of this chapter is to analyse the field distribution along the circumference of the transformer winding, further examining the overall effect of the core window to the winding eddy loss evaluation. Subsequently, the core window effect is evaluated through field quantities determined from three-dimensional models of different simulation types such as:

- Magnetostatic
- Transient
- Eddy current

The availability of the full version of Ansoft Maxwell 14.0 comes in handy when performing analyses of this nature. A core-type, three phase, three winding transformer is simulated in this FEM package and the results are presented. This model is used to assess the contribution of the winding to core distance and also the effect of the adjacent windings.

5.1. Global flux density distribution

The performance of the transformer in operation is affected by load losses. This section graphically presents the distribution of the leakage field obtained using the numerical method. The leakage field from winding blocks of a loaded transformer is distributed as shown in Figure 5.1 below. As already presented, the winding eddy losses are separated into axial and radial winding eddy loss components. In this chapter they are dealt with in a three-dimensional perspective also in a rigorous manner. The respective incident field penetrating the strands is known to be the cause, equally their distribution around the circumference is not known. This field is also responsible for the formation of winding eddy losses, circulating current losses and losses in metal parts as discussed in Chapter 2.

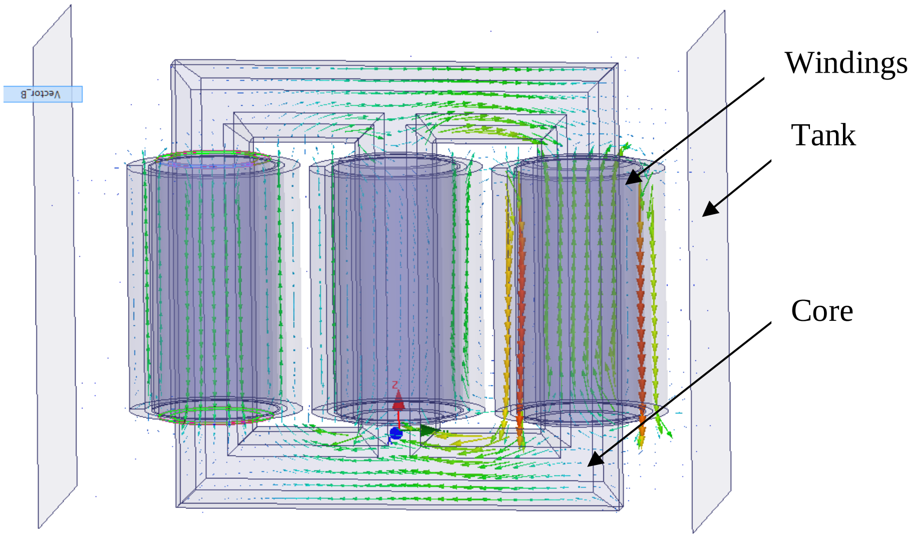

Figure 5.1: 3-D Flux distribution during operation

The theoretical analysis of eddy currents in non-magnetic and magnetic conductors is presented in Chapter 3. The analysis is based on Maxwell's equations that describe the time varying field distributed according to Figure 5.1. This is followed by the use of the one dimensional solution of the diffusion equation. The overall result of the eddy current analysis shows the dependency of the solution on the flux density. This relationship is briefly discussed in Section 5.3 in the context of analysing the core window effect. The analytical method practical for the leakage field evaluation of transformer local field quantities is Rabins' method [49], which is a two dimensional based methodology. In the next section, to aid with the understanding of the core window concept the geometric meaning of this concept is first presented.

5.2. Core window concept

The transformer design approach discussed in-depth in Chapter 1 demonstrated that the commonly practiced core-form arrangement has windings fitted around the core limbs. The bottom and the top sections of the winding are enclosed by the core yokes. This section is focused on discussing the core window concept to elaborate its geometric meaning before it is applied in any computational platform. In principle, a significant portion of the winding is underneath the yokes and this depends on the winding under consideration. Thus, a portion of the winding conductors can be classified with reference to their position relative to the core window as follows:

- The portion of the winding that lies on the inside of the core window (*inside window*).
- The portion of the winding that lies outside the core window (*outside window*).

Figure 5.2 shows section or sections of the windings lying inside and outside the core window.

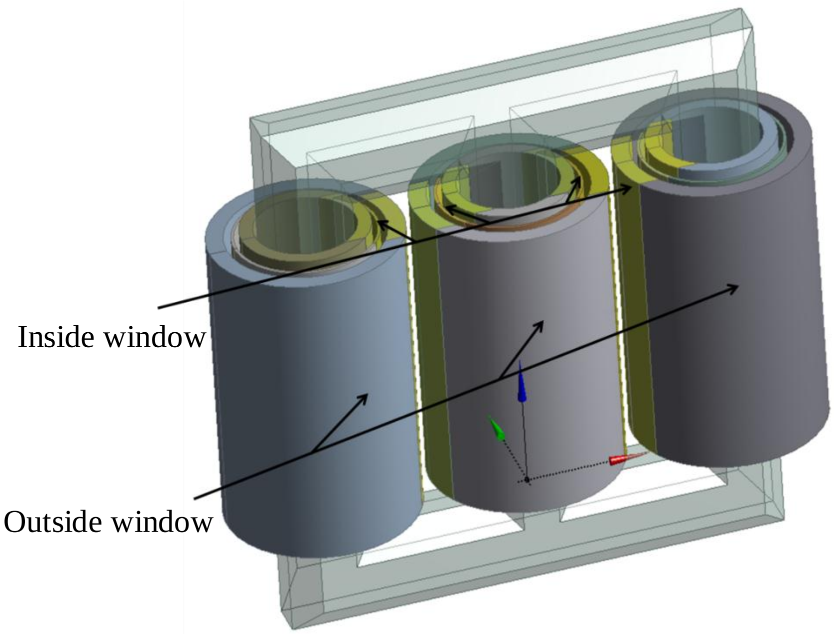

Figure 5.2: 3-phase winding transformer showing the circumference effect.

It is observed that the centre phase windings have a large portion of conductors situated inside the core window. Furthermore, the cross-sectional cases of the two-dimensional views of both these concepts are established as shown in Figure 5.3 and Figure 5.4. In both these figures the two windings and the core of the transformer model are demonstrated. The outermost winding is depicted in detail; a strand level model is shown.

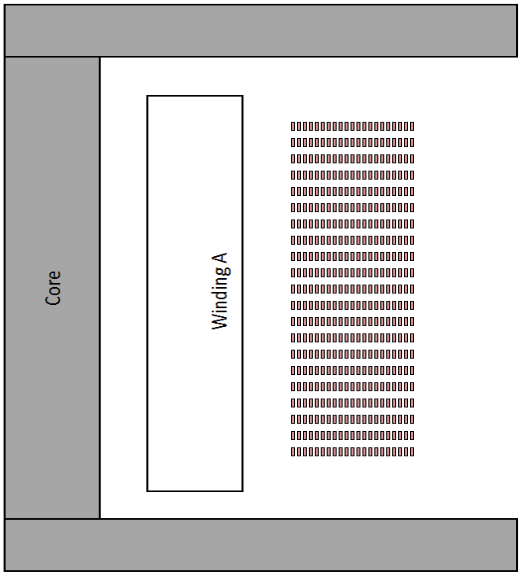

Figure 5.3: Winding sections situated inside the core window

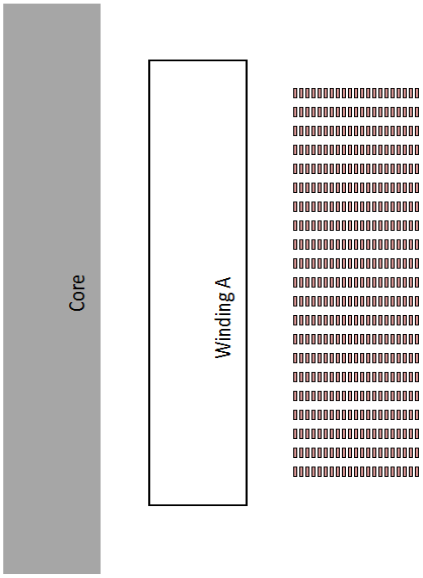

Figure 5.4: Outside core window winding sections

Across the 360° circumference, a winding is likely to be covered by the yokes as seen in Figure 5.2, and it can be approximated that a quarter to a third of the winding conductors lie inside the core window. It is known that the leakage field inside the core window is different to that outside the core window; the next sections will discuss the quantity of this difference. Typically, the field penetrates the yoke at a right angle, which is why the solution of the field in [49] permits the assumption of infinite permeability of the yokes. At this stage, the difference between the field inside the core window and outside of the core window has not been well established.

The presence of the core over certain sections of the winding conductors influences the reluctance path across the circumference. Thus, the reluctance paths travelled by the field in the outer and inner core window regions require a meticulous computation of the field around the circumference to clearly understand this effect.

5.3. Calculation of winding eddy losses

The winding conductors are subject to two components of the incident field, namely the axial and radial flux density components. The consequence of this field penetrating the strands is the winding eddy losses. The detailed formulation resulting in the governing equation outlined in Equation 5.1 is covered thoroughly in Chapter 3. In this section the importance of understanding the leakage field distribution to evaluate the losses is emphasized. The result of the analytical equation is the loss density in Watts per cubic meters of each strand as follows:

$$P_e = \frac{\omega^2 t^2 B^2}{24\rho} \tag{5.1}$$

The next step is to obtain the losses in Watts, done by multiplying the loss density by the strand volume. Additionally, it is seen later in the discussion section that this can also be achieved by integrating the flux density over the volume domain. Below, Equations 5.2 and 5.3 define the loss components as a function of the number of strands for both the radial and axial components. These representations show the computation of winding eddy losses using the field quantities obtained at the mid-point of each strand.

$$P_{ea} = \frac{\omega^2 t^2}{24\rho} \sum_{n_a=1}^{n_{aT}} \sum_{n_r=1}^{n_{rT}} \left(B_a(n_r, n_a)\right)^2 V_s(n_r, n_a) \tag{5.2}$$

$$P_{er} = \frac{\omega^2 h^2}{24\rho} \sum_{n_a=1}^{n_{aT}} \sum_{n_r=1}^{n_{rT}} (B_r(n_r, n_a))^2 V_s(n_r, n_a) \tag{5.3}$$

From (5.2) and (5.3), it is obvious that the losses are proportional to the square of the flux density components. This relationship is important to conductors situated in the same radial position along the winding height. These strands will have the same volume throughout the winding height provided their dimensions are the same. In addition, most practical applications use the same winding strand dimensions per winding.

$$P_{ea} \propto {B_a}^2 \tag{5.4}$$

$$P_{er} \propto {B_r}^2 \tag{5.5}$$

According to Equations 5.4 and 5.5, for the better estimation of losses, the local flux density components require a high degree of accuracy during computations. This underpins the need for a rigorous investigation of the core window effect. The analysis of the core window effect avails the flux density components in differential volumes around the circumference.

5.4. Transformer modelling using 3-D FEM

The previous sections have laid the ground work involving the description of the core window effect. Section 5.3 provided insight on how the flux density distribution around the winding circumference affects the winding eddy losses. The transformer model used for the analysis of the three-dimensional leakage field is presented in this section. The size of the transformer is 40MVA, and the transformer is double-wound. The selection of this unit is motivated by the large number of batches that have been manufactured and tested at Powertech Transformers' Pretoria West plant. The measured load losses of eleven units of this design will be presented in the next chapter.

The transformer under consideration has three windings in each limb, the detailed winding design of each is provided in Appendix C. The geometry is set up in the FEM simulation package ANSYS module "Design Modeler" and exported to Ansoft Maxwell for the calculation of field quantities. The advantage of this approach is the flexibility of the ANSYS package in interweaving the multidisciplinary modules. There are two transformer models established explicitly for the analysis of the core window effect. The first is the single phase case, it is used to analyse the distance to core yoke effect. Meanwhile, the three phase case is used to provide the understanding of the leakage field distribution in each phase and how these are affected by the adjacent windings. Finally, the eddy current simulation is prepared for computing the winding eddy losses.

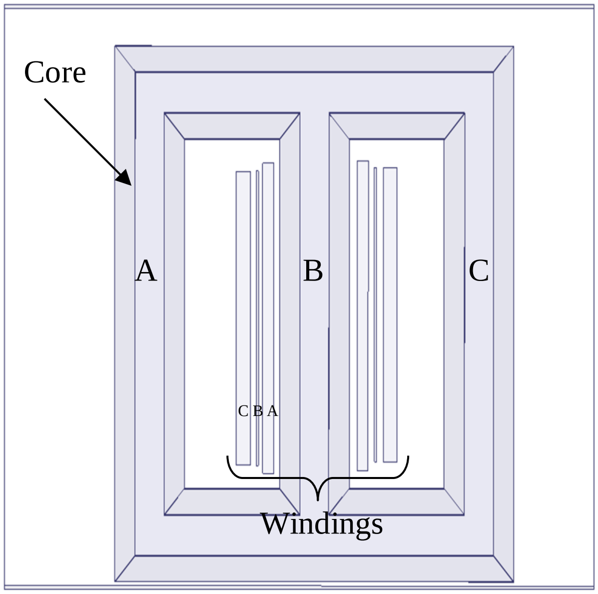

Figure 5.5 a: Single-phase configuration

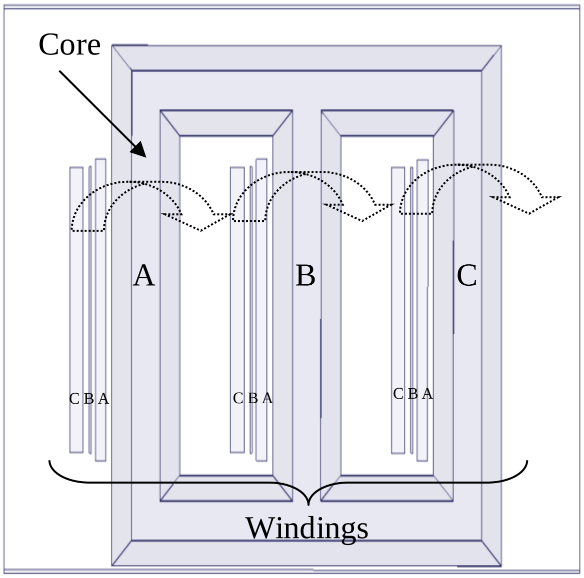

Figure 5.5 b: Three-phase configuration

Once the model is exported to Maxwell, the transformer excitation, loading parameters and boundary conditions are assigned. The excitation data for this specific transformer is provided in Table 5.1.

Table 5.1: 40 MVA excitation data

	Winding A	Winding B	Winding C
Turns	163	56	1072
Current (A)	1210.7	174.95	174.95
Winding type	Helical	Loop layer	Disc

Maxwell uses the adaptive technique to find the converging simulation results. As such, the input parameters of the convergence criterion include the setting of percentage energy error and mesh refinement. However, to improve accuracy, advanced meshing principles can be applied to optimize the simulation time. As an example, seven passes were selected for the eddy current simulation, and the advanced mesh techniques were configured to improve the simulation time. The convergence behaviour obtained as the change of the energy percentage error is depicted in Figure 5.6. The energy error criterion was set at 0.1% of each iterative pass.

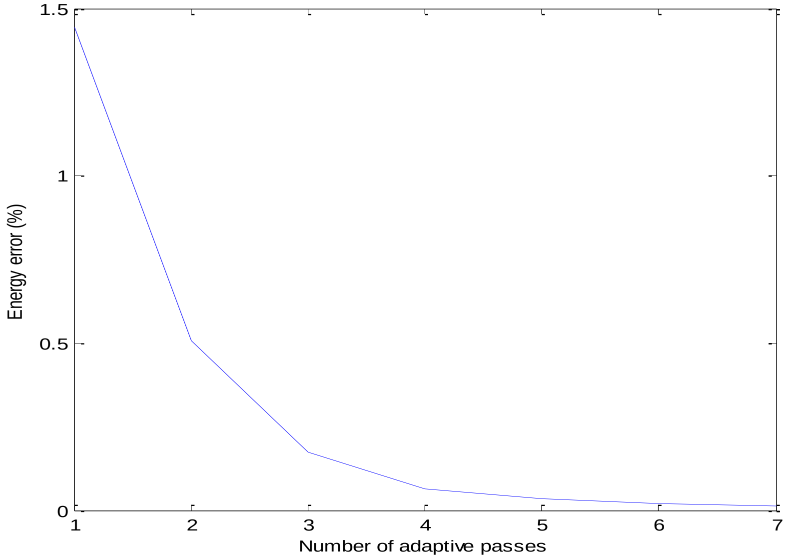

Figure 5.6 : Energy error changes per adaptive pass

From Figure 5.6, the energy error decays exponentially as the number of passes increases. This indicates the sufficiency of the choice of seven iterative passes as where the global energy error decays below 0.1%. The results obtained after the convergence of the solution are post-processed in the next sections. The magnetostatic, eddy current and transient solutions are presented for the purposes already mentioned.

5.5. Results post-processing procedure

Immediately after the simulation run is completed, the field quantities became available from the components defined by the transformer geometry model. This section describes how the field quantities are obtained from the model. In addition, the focus is placed only on the regions applicable to the window sections. These are of utmost importance for the study of the core window effect. Two methods are used to extract the field quantities namely; through a non-model object line or using coordinates text file as an input. Both methods are explained briefly in this section.

These two methods are applied intensively to post-process the field distribution. A non-model circular polyline is drawn around one winding object of the simulated transformer model. This line can be duplicated to the remaining phases of interest, especially in the three- phase simulation model. Here, the *z* coordinate of the lines is the top of winding A (1682 mm) as provided in Appendix C, and this location is used throughout the analysis. The choice of this location is already observed in the preceding chapter where; it was shown that the radial flux density becomes significantly higher towards the winding ends. Figure 5.7 illustrates this line drawn in each winding for the acquisition of field quantities.

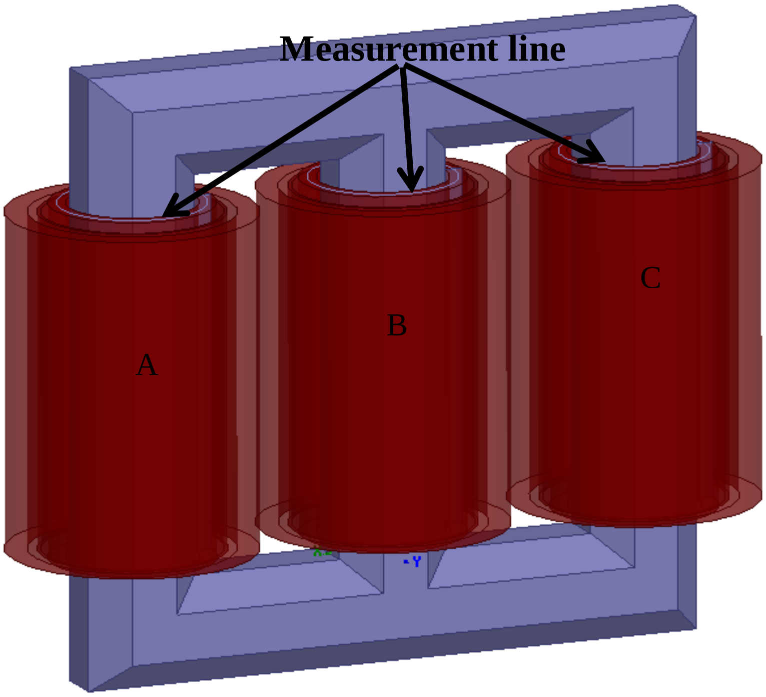

Figure 5.7: Non-model object line drawn for the acquisition of the flux density

The alternative to the method presented above is to obtain field quantities in the circumferential direction by extracting them using an automated routine. Such a routine is written in Matlab to transform the Polar coordinates data to Cartesian coordinates. The *x* and *y* coordinates are calculated with a 0.36° step change equivalent to Polar coordinates. This yields 1001 sample points around the circumference. The corresponding flux density components are then extracted from the model.

For the analysis of the flux density, the “field calculator” in Maxwell is used. Both methods of attaining flux density components are used with the calculator. However, for simplicity, the first method is preferred. This is because it is more robust and achievable with few computational steps. The second method is also used in circumstances where the drawing of the non-model object is considered challenging.

For the study of the circumference flux density distribution, the field quantities are plotted on the polar coordinates system. The selection of this approach is mainly to enhance the visualization of the distribution of the field components. Following this discussion, the next sections present the results obtained using either one of the above methods.

5.6. Circumferential field distribution

The sets of results reported in this section are primarily the flux density components obtained around the circumference of winding A from a magnetostatic simulation. The flux density values of interest are those calculated at the mid radial dimension of the winding. The results are post-processed in the manner described in the previous section.

The full ampere-turns are assigned to phase A, meanwhile phases B and C have the same half ampere-turns in the opposite direction. This is to ensure that there is an ampere-turn balance, i.e. the sum of all winding ampere-turn values is approximately equal to zero. With the use of the field calculator in Maxwell as earlier reported, the field equations for the *r* and *z* components of the flux density are defined. It is already mentioned that the results are acquired at 0.36° resolution. This resolution is considered sufficient to observe the changes of the flux density components. This is evident in the graphical results presented in this section.

The results of the setup described above are presented in Figures 5.8 and 5.9 for radial and axial components of the flux density respectively. The two components are assessed individually below.

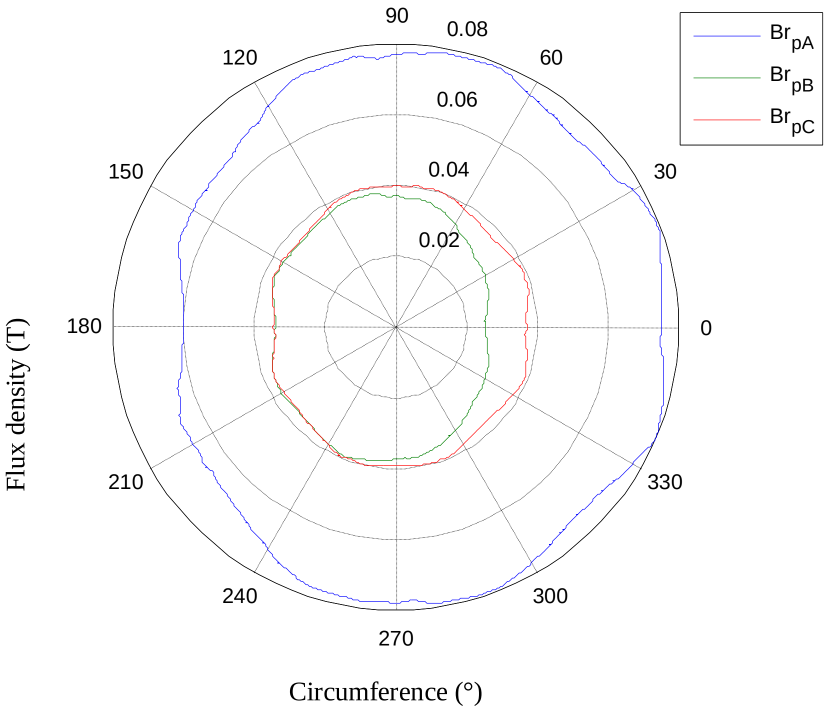

Figure 5.8: Radial flux density distribution around the circumference

Figure 5.8 shows the radial flux distribution for phase A, B and C around the circumference. It is noted that the magnitude of phase A is higher than B and C which is expected. This is due to the proportional relationship between the current and the flux density. Furthermore, the radial flux component plotted above is the magnitude of the x and y components. This is in part due to the coordinate system transformation of B_x and B_y to cylindrical coordinate system components r and z. Hence, the radial field is analysed using the magnitude only.

The maximum flux density of phase A is approximately 0.08 T; meanwhile the minimum is 0.06 T. This difference between the two extreme values yields 25%. The flux density of the other two phases is distributed in a similar manner to that of phase A; the exception is phase B. In this phase the distribution shrinks inwards on the right hand side of Figure 5.8. The flux density distributions of the three phases clearly indicate that there is a reduction of the radial components on the sections covered by the core. The next figure shows the distribution of the axial field in the same locations. This plot serves to provide insight on how axial field levels of the sections under the core window are affected.

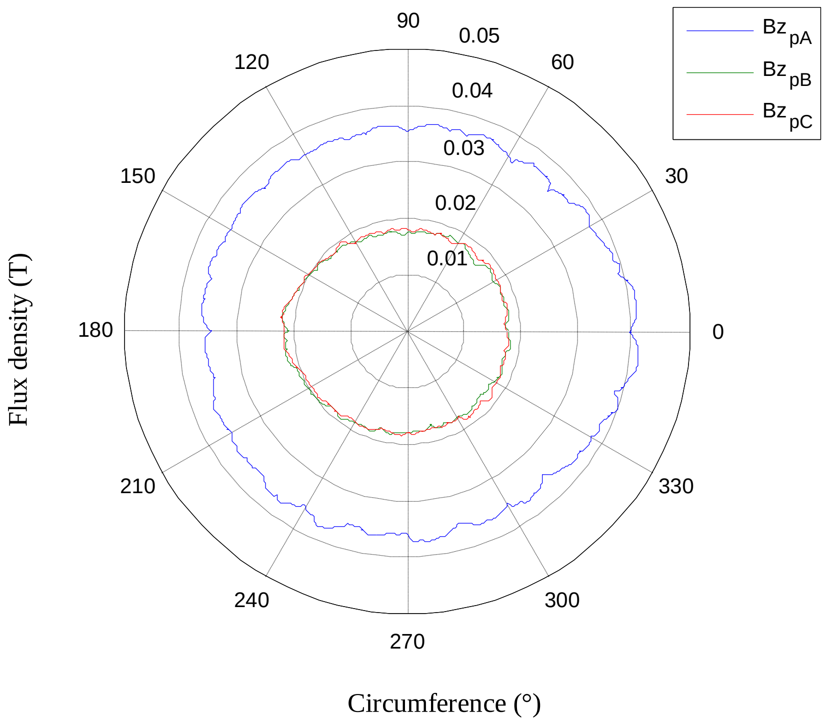

Figure 5.9: Axial flux distribution for phase A, B and C along the circumference

Similarly with the assessment of the radial component, the results of axial flux density are acquired and shown in Figure 5.9. However, the axial component does not need an additional manipulation as the z component is the same for both the cylindrical and rectangular coordinate systems. Phase A has the magnitude of approximately 0.036 T. The peak is observed on the path of 270° to 90°, strictly in the anticlockwise direction. The difference between the maximum and the minimum field is approximately 16% of the maximum flux density of 0.041T. Essentially, the axial flux density distribution is almost uniform across the circumference of the winding. This immediately implies that the radial field components are more significantly affected by the core window as compared to the axial component.

The distribution of phase B and C is equal in magnitude across the circumference of the windings. Notably, the two components show the peak in the same direction as illustrated in Figure 5.9. The latter confirms that apart from the presence of the core, the adjacent windings cause the non-uniform distribution of the field. Lastly, at this stage it is not clear whether the non-uniform distribution is due to the presence of the core or the ampere-turn of the adjacent windings. To further understand the core window phenomenon, the change of the winding to core yoke distance is studied. In addition, the effect of the adjacent winding is assessed using the transient simulation. It is also established later how the field quantities deviate from the average.

5.7. Effect of the winding to core yoke distance

In the preceding section it is mentioned that there is no obvious evidence of the main cause of the non-uniform behaviour of the field around the circumference of the winding. Consequently, an additional simulation of the single phase model was setup. This simulation is a single phase transformer of three limbs. Since the aim is only to assess the core window effect the same unit was selected with few alterations. In this model the windings of the side limbs are removed.

The assessment of the core window is conducted through a simulation of numerous design points that are established. In each design point the limb height of 1808 mm as shown in Appendix C is reduced by 21 mm. However, the minimum case is the limb height of 1684 mm as shown in Table 5.2. According to the 21 mm reduction this value should be 1682, however, to prevent a convergence problem a 2 mm gap is reserved. Table 5.2 shows all simulation cases considered for the analysis of the winding to core yoke distance effect.

Table 5.2: Single phase parametric design points

Simulation Case	Limb Height (mm)	Winding to Top Yoke (mm)
1	1808	126
2	1787	105
3	1766	84
4	1745	63
5	1724	42
6	1703	21
7	1684	2

To prepare these design cases, the geometry model of the test transformer is parameterized in the ANSYS module, Design Modeler. This environment is flexible to small changes of the geometry and application of the optimization tools as earlier indicated. Essentially, the seven design models presented in Table 5.2 should be individually prepared by manually changing the parametric values. However, in ANSYS workbench there is a variety of design optimization tools which are tailored to the parametric modelling approach. As a result one of these tools called "Response Surface" was manipulated to instantly create seven design points. In addition, for the full use of this tool an independent "DesignXplore" component "Optometrics" in Maxwell is required. Due to a lack of this resource the full simulation of each model is not automatically accomplished. These simulation models are updated manually.

Through the development of the numerous models of different limb height dimensions, the results of flux densities are extracted and presented. The results of the flux density distribution around the circumference of the winding for the single phase transformer are shown in Figure 5.10 and Figure 5.11.

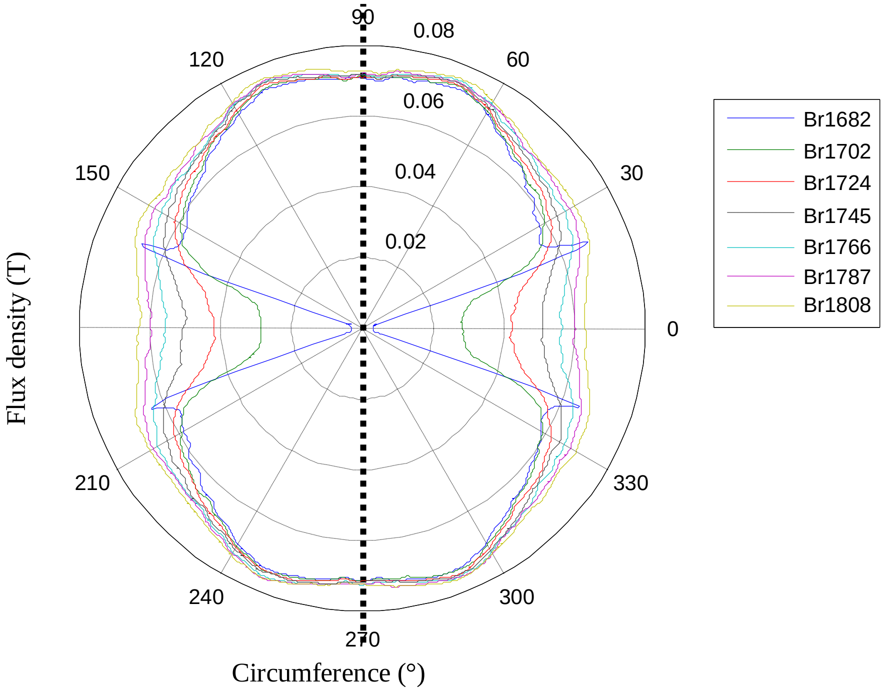

Figure 5.10: Radial flux distribution across the winding circumference

It is shown in Figure 5.10 that the radial flux density is proportional to the winding to core yoke distance. For the winding to core yoke distance of 2 mm the radial flux density approaches zero inside the core window. The distribution of the radial component is symmetric both in the *x* and *y* planes, hence the core window effect accounts for 22°out of the 90°. This is the angle at which the field is visibly deviating from the circular line or the mean value. It is also observed that the high winding to core yoke distance is indispensable to achieve a uniform distribution of the radial flux density components. Furthermore, the minimum flux density of 0.00298T is observed when the minimum winding to core yoke distance is 2 mm. This flux density value is 95.25 % lower than the maximum.

For the same geometry configuration the distribution of axial flux density components was also analysed. Flux density attained by varying the geometry according to Table 5.2 is shown in Figure 5.11.

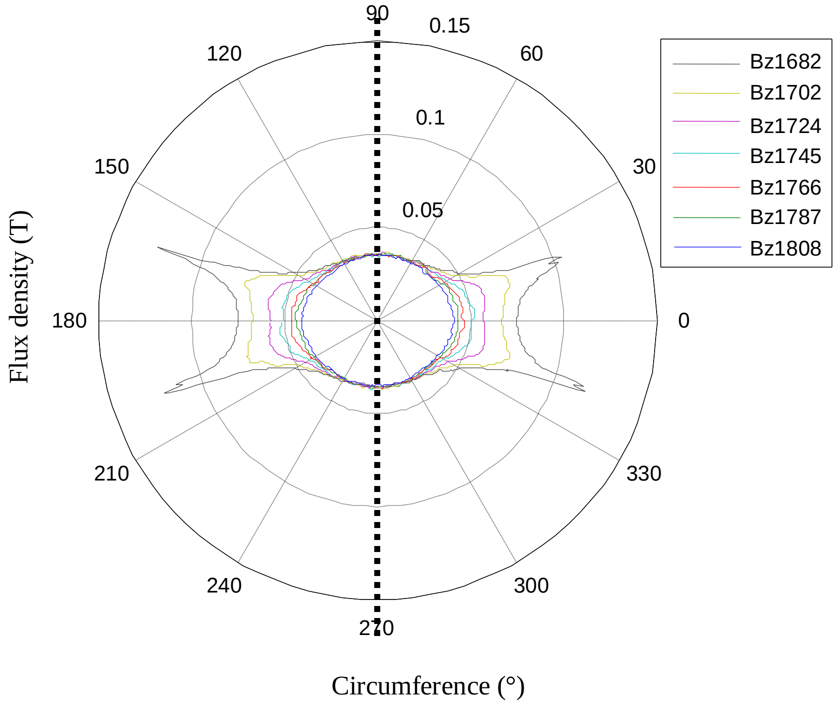

Figure 5.11: Axial flux distribution across the winding circumference

The results of the axial flux density of different winding to core yoke distances are shown in Figure 5.11, it is apparent that the axial field component is inversely proportional to this distance. This is also followed by the irregular distribution of the field around the winding circumference. At the extreme minimum distance of 2 mm the orientation indicates the maximum flux density to be inside the core window. It is also evident that the field distribution is almost symmetrical in the *x* and *y* plane. Effectively, out of 90° the core window effect accounts for 30°. However, the higher winding to core yoke distances illustrate that the non-uniform distribution of the field diminishes. The latter is seen when the limb height is 1808 mm.

To understand the real meaning of the results, it is necessary to compare the mean flux density against the actual flux density distribution. Thus, the leakage field distribution of the minimum case is compared against the average.

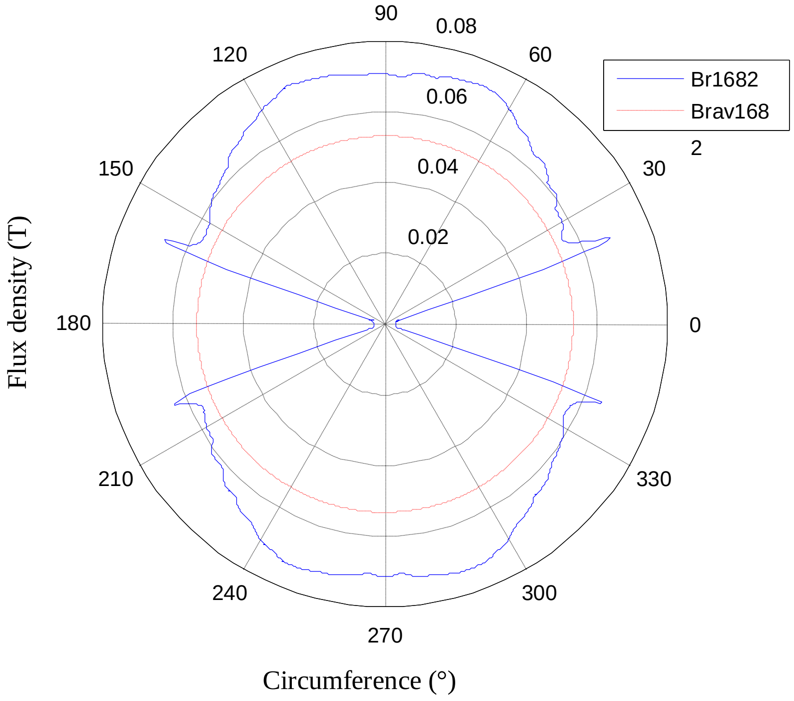

Figure 5.12: Radial flux density plotted with the average value

Figure 5.12 shows the radial flux density obtained when the limb height is 1684 mm. The mean flux density distribution around the circumference is 0.0532 T. It is assumed that this line represents the 2-D axisymmetric case. The actual radial distribution around the circumference fails to track the mean value. This is an indication that at low winding to core yoke distances, the consequences of the core window effect could be significant. For practical applications, the aforementioned distance is not common. Distances larger than 100 mm at the top and 60mm at the bottom are ordinarily used. These distances are dictated by dielectric clearance requirements and pressing of the top and bottom winding ends.

It is also observed from Figure 5.12 that the task of assessing the core window effect is complex when using two dimensional tools. There are two main prevailing behaviours observed:

- The radial flux component outside the core window section is larger than the mean value.
- The section of the winding circumference lying inside the core window is subject to lower field values than the mean.

To further analyse this phenomenon, the axial field is studied against the mean.

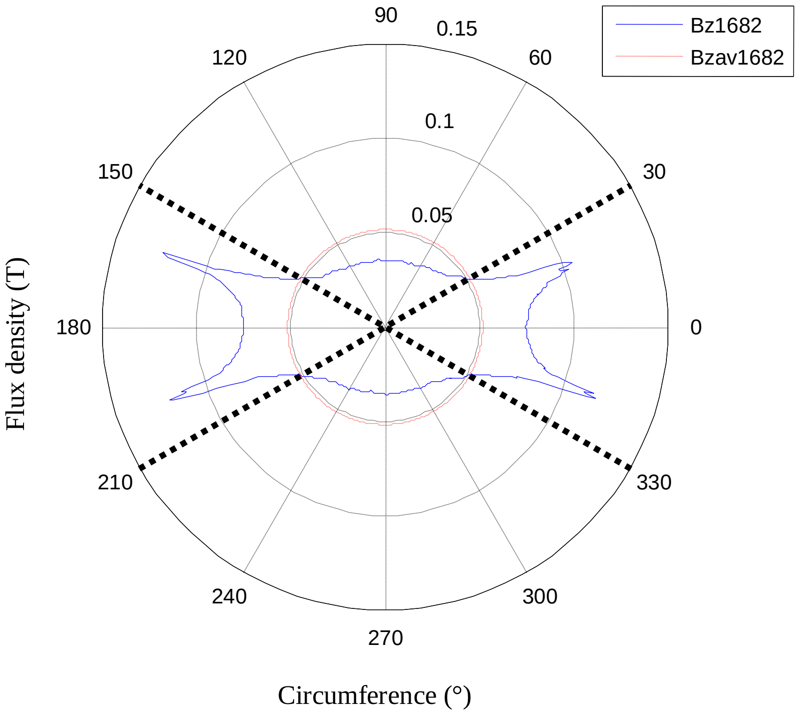

Figure 5.13: Radial flux density plotted with the average value

Illustrated in Figure 5.13 is the average distribution of the axial flux density across the winding circumference, which is shown as a red dotted plot. It is the mean value calculated by taking all axial flux densities across 360°. The critical observation from this distribution is the intersection points of the actual and average distribution located at 30°, 150°, 210° and 330°. The average flux density is 0.05168 T, the maximum flux density deviates by approximately 128.3%. It should also be mentioned that this point is a peak value and may have little consequence on the overall losses.

The result of the study of the effect of the core window effect has so far shown that the sections under the core window will experience high axial field and low radial field intensities. The findings are congruent with the conclusion made during the implementation of Rabins' method [49] in Chapter 4 where, the boundary conditions at the yokes incorporate the assumption that the field is normal to the yokes. In addition, the results of the study presented in this chapter are found to oppose the conclusions drawn by Waters [57]. In his studies of the axial forces he comments that the presence of the core does not cause the concentration of flux around the circumference. The polar plot presented in his paper show uniformly distributed radial flux density. Therefore, according to the study in this section the core has an effect dependant on the distance between the winding and the core yokes. A great deal of details will be missed if the variation of this distance is not done.

5.8. Transient analysis

The analyses of the flux density distribution discussed in Section 5.6 show that the adjacent windings influence the field around the circumference. In order to establish the extent of this influence, a transient simulation is required. In this section the study of flux density distribution around the circumference during different time intervals of the sinusoidal excitation is undertaken. From the knowledge of the period of the full 50 Hz sinusoidal signal, six simulation points were considered. The simulation runs from a time step of 0s to 0.02s, in steps of 0.004s. The transient discrete simulation points are depicted in Figure 5.14.

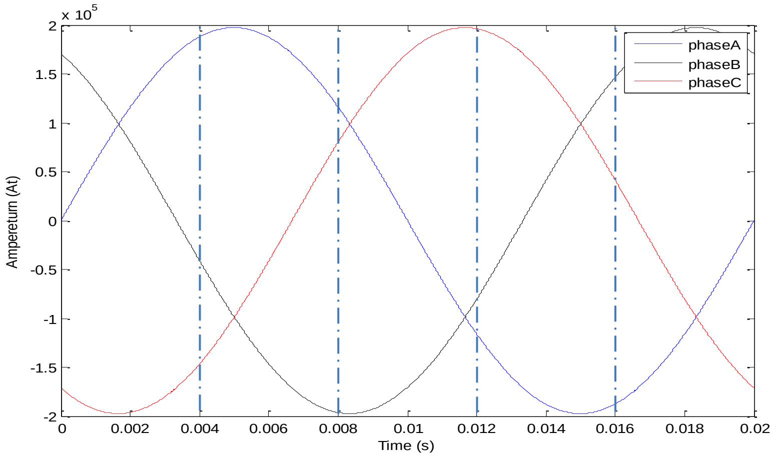

Figure 5.14: Sinusoidal excitation with discrete transient simulation points

In Figure 5.14, the ampere-turns of each phase are shown in the sinusoidal form. The ampere-turn unbalance of the simulation points was also calculated discretely to confirm that it approached zero.

The three-dimensional model already prepared during magnetostatic simulation is reconfigured for the transient analysis. The results obtained for the first windings of each phase are presented for t=0, 0.004 and 0.012 s. In each of the above mentioned points the winding A magnitude contours of the field is plotted. Figure (a) of 5.15 to 5.17 is the radial flux density component. Similarly, Figure (b) is the axial flux density component.

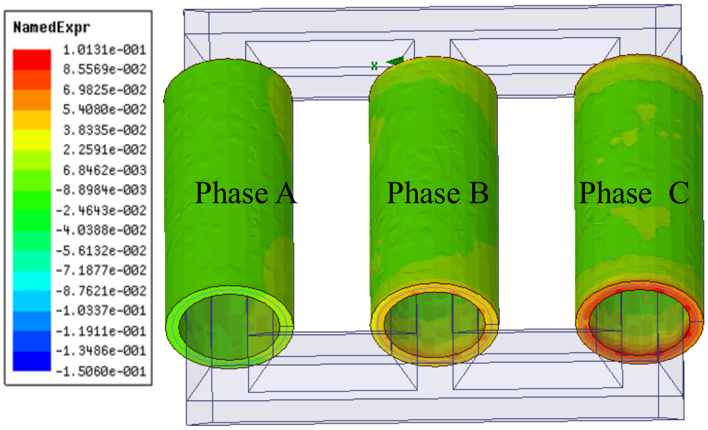

Figure 5.15a: Radial flux density at t=0

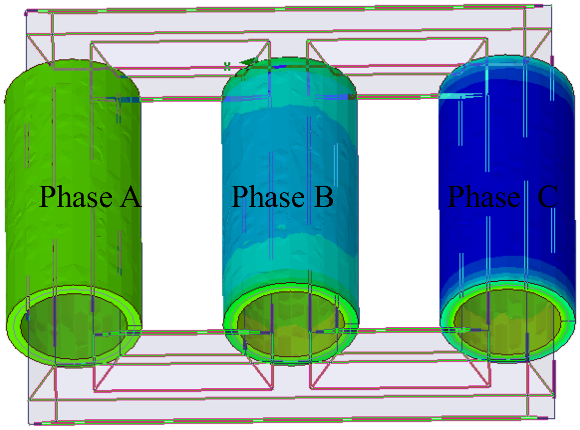

Figure 5.15 b: Axial flux density at t=0

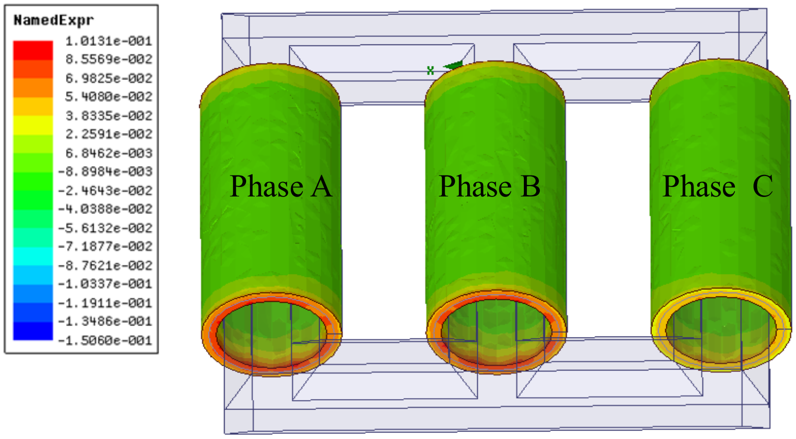

Figure 5.16a: Radial flux density at t=0.004

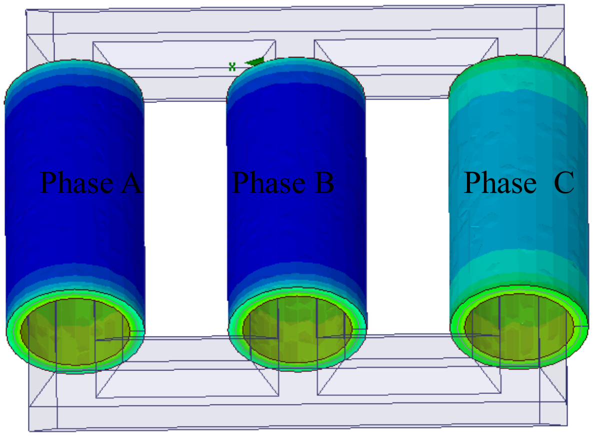

Figure 5.16 b: Axial flux density at t=0.004

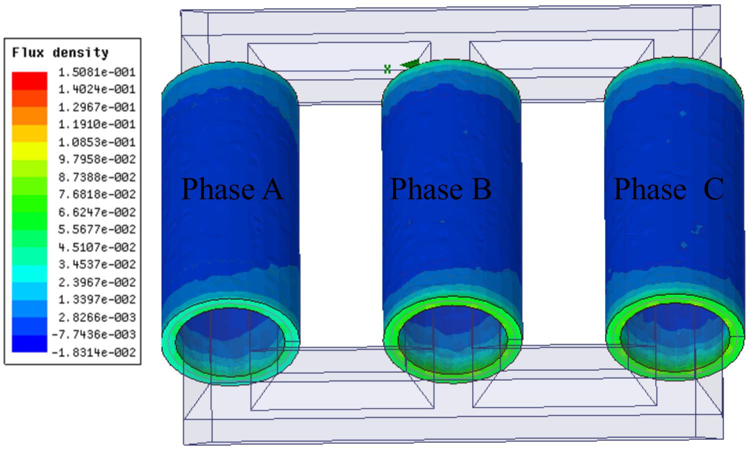

Figure 5.17a: Radial flux density at t=0.012

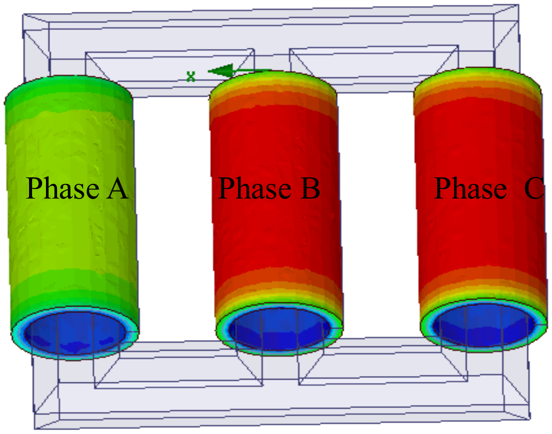

Figure 5.17b: Axial flux density at t=0.012

From Figure 5.15 to Figure 5.17, the flux density distributions on all the surfaces of the windings are shown. The contour maps of the magnitude of the field at different time intervals are shown. At t=0s, the excitation cycle indicates that phase C has the maximum radial flux density on the outer surfaces of the winding. The same behaviour is observed in Figure 5.15(b), except that it is obvious that the field is generated by the excitation in the most negative cycle. The repetition of this behaviour depending on the phase that has the maximum radial flux density value is seen at t=0.004 and 0.012s. From these figures it is not easy to draw conclusions on the field behaviour as a consequence of the presence of the adjacent windings. Therefore, a detailed comparison is required. The flux density components were then extracted from the location of the non-model object line. The field distribution is shown in Figures 5.18 to 5.20 obtained at t=0.012 s.

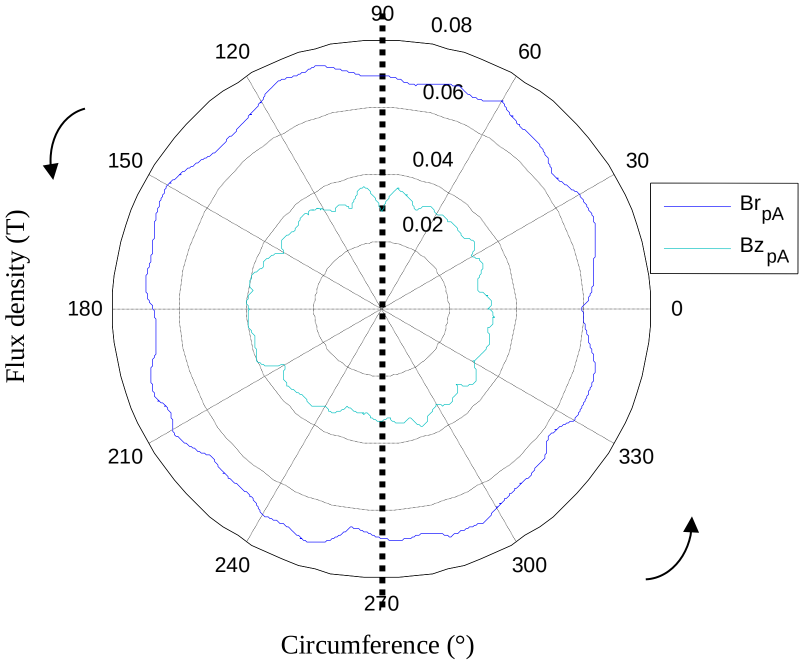

Figure 5.18: Flux density distribution of phase A at t =0.012 s

The results shown in Figure 5.18 have ripples; up to so far smooth results have been obtained. These ripples are an indication that the mesh elements regarded sufficient for a magnetostatic solution may be inadequate for the transient analysis. Nonetheless a conclusion is drawn from these results since the fundamental profile is preserved. There is an evident shift of both flux density component quantities showing an increase from the 90° to 270° quadrants.

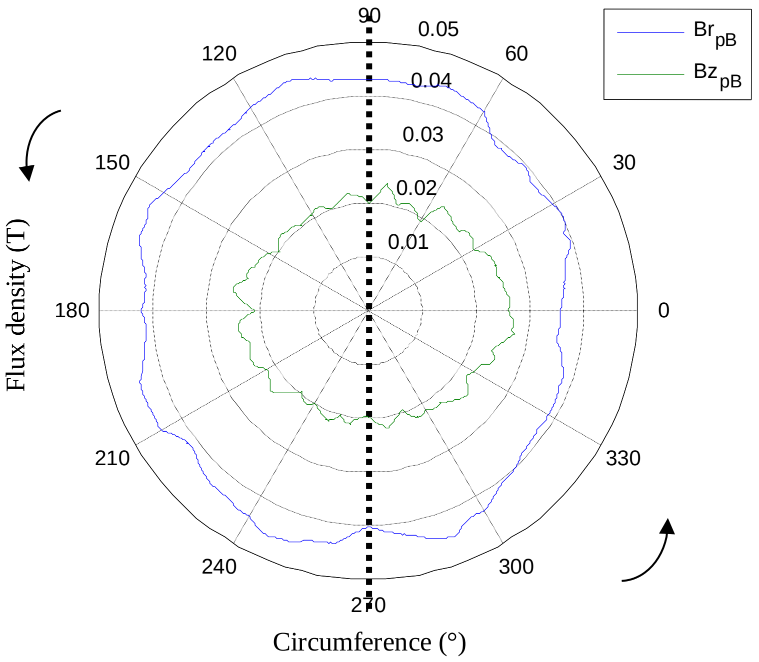

Figure 5.19: Flux density distribution of phase B at t =0.012 s

Figure 5.19 shows the radial and axial flux density components of phase B at t=0.012s. There is a shift of the maximum radial flux density distribution leaning towards the 90° to 270° quadrants. The peak of the axial flux density component is shifted along the path of 270° to 90° quadrants. The characteristics of the field distribution of a single phase in a 3 limb transformer have already been established from the previous section. The results of this phase are supposedly equivalent to the single phase transformer case if the effect of the adjacent winding is neglected. Therefore, this can assist in distinguishing the contribution of the adjacent windings.

The axial flux density of phase B is almost half that of phase A at approximately 0.02 T. The same can be said for the radial component which is estimated at 0.04 T in comparison to 0.08T in Figure 5.18. The field distribution is almost symmetric only in the *x* plane.

The axial and radial flux densities of the single phase illustrated symmetry in the *x* and *y* planes of the distribution of flux densities around the circumference. The fact that the field distribution observed on this phase in Figure 5.19 is shifted towards the opposite/ a different side indicates the effect of the adjacent windings. It is difficult to estimate or quantify the effect of the adjacent winding from the set of results presented so far.

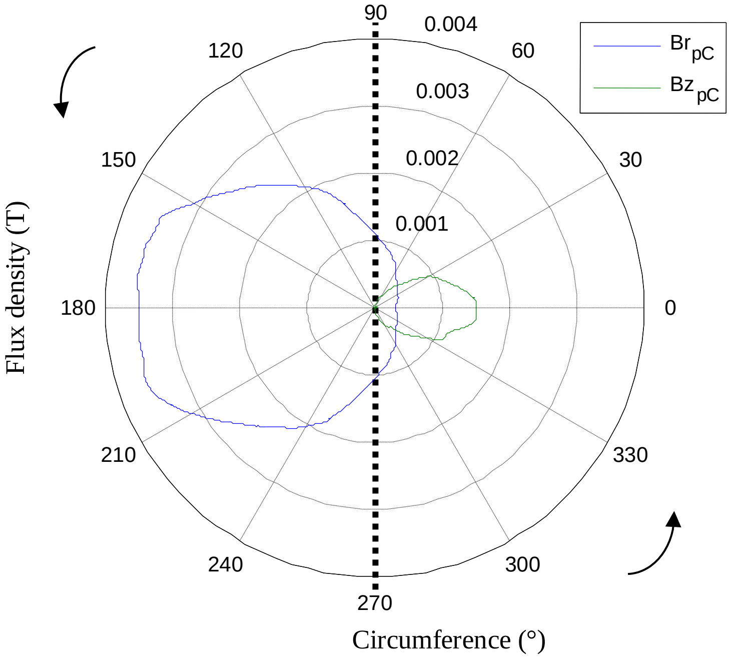

Figure 5.20: Flux density distribution of phase C at t =0.012 s

In Figure 5.20 it is apparent that the distribution of the magnetic field components of phase C lies in the opposite quadrants. The radial component is leaning towards the 90° to 270° quadrants with a small overlap that is close to the zero line. On the other hand, the axial field is distributed only in the 270° to 90° quadrants. This evidence shows that there is a dynamic ampere-turn balance requirement during operation, which is mainly achieved by the contribution of the adjacent windings.

It is concluded that the core window effect is attributed to the combination of both the winding to core yoke distance and the contribution from the adjacent windings. The next section details the evaluation of winding eddy losses using the three-dimensional flux density quantities. The contribution of the investigated phenomenon to the overall winding eddy losses is presented.

5.9. Result discussion

The core window effect has been studied with the use of three-dimensional models of the single-phase and three-phase transformers. In this section, the final three-dimensional winding eddy loss components that take into account the core window effect are discussed. The overall effect of the core window is established through the comparison of the 3-D FEM and 2-D FEM axisymmetric results. In addition, to validate the 2-D FEM results the results of the in-service analytical program used by Powertech Transformers are provided. It is important to note that the 3-D calculations are obtained using Equations 5.2 and 5.3 presented in Section 5.3. The field calculator in Maxwell is used to simplify the calculation. Lastly, the results are multiplied by the respective winding space factors, to account for the copper to insulation ratio in the conductors of the cylindrical object. The details of the winding design are provided in Appendix C.

Table 5.3: Calculated winding eddy loss results

		3-D FEM		
		Phase A	Phase B	Phase C
Winding A	P_{er}	173.16	130.42	171.93
	P_{ea}	1846.81	1859.119	1847.97
Winding B	P_{er}	5.22	10.09	5.17
	P_{ea}	590.72	616.2961	592.44
Winding C	P_{er}	932.89	1287.49	945.98
	P_{ea}	1901.36	1958.321	1906.49
	Total	5450.16	5861.74	5469.98

The winding eddy losses in Watts are calculated and tabulated in Table 5.3, the radial and axial components are shown separately. The 3-D FEM results were computed using the eddy current transformer model. Phase A, B and C are assigned phase shifted currents of 0°, 120° and 240° respectively. It is demonstrated from the table that the total results of phase B are higher than phase A and C. This is due to symmetric distribution of the winding eddy losses of the side limbs. In addition, these results are a clear indication of the need to understand the core window effect. However it is not apparent which of the investigated effects in the previous section is prevalent. The single phase, 3-D FEM simulation results presented below will provide the necessary insight.

A detail analysis of the results in Table 5.3 reveals that the radial winding eddy losses are the most affected by the core window effect. In particular, the radial component of the winding eddy losses of winding A of phase C is 31.83% larger than phase B. Contrary to these observations, the radial winding eddy losses of winding C of phase C is 26.53% less than those of phase B. It is apparent that the axial component is less affected; the difference of the results between any windings is within 4%.

The single-phase results of the three-dimensional model, 2-D FEM axisymmetric model and in-service program are presented in Table 5.4. Firstly, it is remarkable that the difference between total 2-D FEM and in-service program losses is 0.48%. The in-depth analysis of the results shows that the local quantities are slightly different. The component losses of the winding A are compensated in the winding B. The difference that is observed can be attributed to the empirical factors embedded in the service program. The results in Table 5.4 are expected to provide details of the contribution of the investigated phenomena pertaining to the core window.

Table 5.4: Single phase at the limb height of 1808 mm

		3-D FEM Phase B	2-D FEM	In-service program
Winding A	P_{er}	127.38	639.32	502
	P_{ea}	1851.54	1826.59	1836
Winding B	P_{er}	3.06	0.7093	0
	P_{ea}	600.65	560.4854	599
Winding C	P_{er}	829.4	871.355	989
	P_{ea}	1923.06	1849.509	1794
	Total	5335.08	5747.97	5720.00

The single-phase, 3-D FEM results of winding A and winding B are consistent with the 3-D FEM phase results presented in Table 5.3. On the other hand, the single-phase winding C results are 458.09W less than the 3-D FEM three-phase results. It can therefore be concluded that this difference is due to the effect of the adjacent windings. Subsequently the adjacent winding influence affects only the radial winding eddy losses of the centre phase and outer winding. This phenomenon can be as high as 48%, culminating in the additional losses with respect to the side windings. Again from Table 5.3, it is concluded that the presence of the core above the windings may result in a difference up to 32% between the sides and centre windings. This is indicated by the results of winding A.

The comparative study has shown that the local flux density is non-uniformly distributed around the circumference of the transformer windings. The local errors have been presented from numerous sets of results. However, the overall difference of the winding eddy losses obtained from the 3-D FEM and 2-D FEM methods is about 462.03W. This constitutes a difference of 3%, which may be considered insignificant. The use of the 2-D axisymmetric model approach overestimates the radial component drastically. The difference may be in the region of 400% larger.

5.10. Conclusion

A novel approach to evaluate the effect of the core window in the determination of winding eddy losses is established. The transformer models of different solution types are developed and the results are analysed. The analysis involved the examination of the effect of the winding to core yoke distance and the influence of the adjacent windings during the phase shifted excitation cycles.

The core window effect is observed to influence the results of the winding eddy losses, particularly the local flux density calculations. However, the overall loss results are marginally affected. Despite that, the local values can have severe implications on the design of cooling system. The results revealed that the winding to core yoke distance should be greater than 84 mm to avoid significant calculation errors that can be incurred due to the core window effect.

The next chapter compares the 3-D FEM, three-phase results presented in this chapter against the measured results. The calculated results from the three-dimensional approach are now considered accurate, as they account for the core window effect.

Chapter 6

Experimental results and discussion

This chapter presents the measured winding eddy losses of the transformer used in the preceding chapter. The three-dimensional finite element method model is used to evaluate the other stray loss components induced outside the windings. It is outlined in Chapter 1 that the measurable load loss components are the total losses and dc losses, of which the difference is stray losses. The literature survey detailed in Chapter 2 discusses the evaluation of losses in metal parts.

In this chapter, the stray losses in structural parts are evaluated with the intention to strategically separate winding stray losses from the measured stray loss component. This difference is considered as measured winding eddy losses. The measured winding eddy losses are then compared to the winding eddy losses calculated in Chapter 5. The important assumptions made are: the three-dimensional finite element method results are accurate and there are no circulating current losses in windings.

In predicting the structural part losses, the three-dimensional FEM package from Ansoft Maxwell is used. This 3-D FEM package uses an adaptive meshing technology as presented in Chapter 5. The meshing scheme of this package is prevalent in the simulation of electromagnetic problems to optimizing the meshing processes. The adaptive schemes are able to approximate better the exact solution with a smoother distribution of nodes, especially in regions of high error

[58]. In addition, the error in the field distribution calculated using the finite element method strongly depends on the mesh used [59]. With the abovementioned improvements, the computation of stray losses in structural parts is still intricate. This is partly because of the small skin depth of mild steel, which is prominently used for tank walls, core clamps and flitch plate structures. The thin regions can be expensive to model using volume finite elements if the dimensions of the device are comparatively large [62].

There is an abundance of literature material already available to better model the skin depth layers such as surface impedance modelling and shell modelling approaches. Through these approaches, the time-harmonic regime solvers are modified to take the nonlinearity of the material into account using approximate formulations. The work of [31], [64], [65] involved the application of surface impedance and shell modelling. Having discussed the above, the commercial package Ansoft Maxwell that is available for this study does not have the capacity to take nonlinearity into account. This shortcoming is accepted and allowed for in this study. A comment by [43] that the linear simulation results can be corrected by multiplying them by a factor of 1.1 to 1.4 is leveraged.

The purpose of this chapter is to synthesize the measured and calculated load losses and compare the perceived measured winding eddy losses to the winding eddy losses. This chapter begins by discussing the measurement aspects of load losses, and provides the measuring circuitry. The test results of eleven transformers of the same design then follow. The results of the stray losses in structural parts are also covered.

6.1. Load loss measurement

The results of the load losses for the tested transformers are presented in this section, and they are obtained using the IEC standard [1]. The definition of load losses according to this standard is “the absorbed active power at a rated frequency and reference temperature associated with a pair of windings when rated current (tapping current) is flowing through the line terminals of one of the windings, and the terminals of the other winding are short-circuited. Further windings, if existing, are open-circuited”. Thus, a circuit connection satisfying this definition is arranged during load loss test of the eleven transformers.

It has been echoed in the introduction that the components of load losses measurable are; the total losses and the I^2R losses. The numerical difference between the two components is regarded as the stray losses of the transformer, a formal definition of stray losses can be found in [60]. During the measurement of load losses, according to [1] the tolerance is limited to 10% of the load losses specified by the customer. However, in the event that they are exceeded a consultative process can be followed with the customer to reach an agreement or arrange payment of penalties. Furthermore, [60] provides the test system accuracy, which should be maintained at ±3% for load loss measurements. This requirement assists in ensuring that the measurement equipment is constantly serviced to avoid unnecessary measurement errors. Following the guidelines presented above, the circuit that is generally used is discussed in detail in the next sub-section.

6.1.1. Measuring circuitry

From the measurement procedure described above, the measuring circuit for the measurement of transformer load losses is set-up as shown in Figure 6.1. The three phase circuit connection showing the components of the entire circuit can also be found in [61].

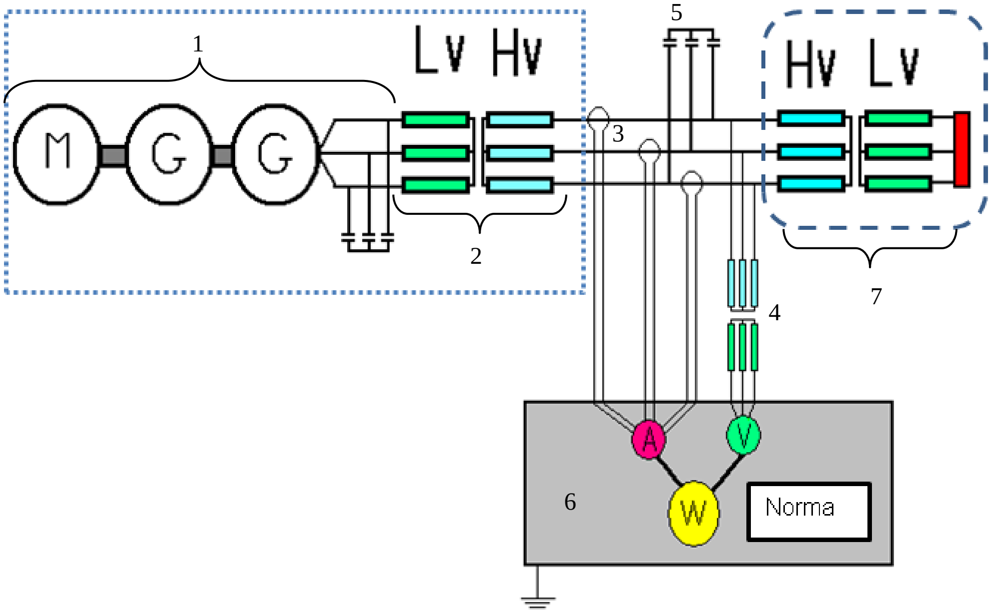

Figure 6.1: Three-phase load loss measuring circuitry

In Figure 6.1, the circuit components are as follows; 1-The alternator, 2-Testing transformer, 3-Current Transformers (CTs), 4-Voltage Transformers (VTs), 5-Capacitor banks, for power factor correction, 6-Wattmeter, 7-Transformer being tested. In addition, items 1 and 2 of Figure 6.1

belong to the internal test facility or capacity available at Powertech Transformers. The Three-wattmeter method is used to record the losses of the transformer.

When testing, the impedance voltage test is conducted. This is done by exciting the HV windings while the LV windings are short-circuited, and this happens until the rated current flows in the LV side. This test procedure was followed to obtain the results of transformers presented in the sub-section 6.1.2. The design of the unit investigated has been manufactured and tested numerous times. For the comparative study, the record of the results of some of these units are retrieved and presented next.

6.1.2. Load loss test results

In this sub-section, the stray losses of the eleven transformers tested during 2010, from June to November are presented. The 40 MVA, 132/11kV transformer has been analysed in Chapter 5, where the three-dimensional winding eddy losses are calculated. The stray losses are measured at various temperatures and corrected to 75°C using the fundamental formula in [1]. Therefore, the last column of Table 6.1 shows the combination of measured (winding and metal part) stray losses at 75°C. It is noted that the measured LV current shown in Appendix D is approximately 175 A, which corresponds to current shown in Table 5.1.

Table 6.1: Measured stray losses of the tested units

	Test Date	Rating(MVA)	Voltage(kV)	Measured(kW)
Transformer 1	15-Jun-10	40	132/11	46.62
Transformer 2	19-Jun-10	40	132/11	50.30
Transformer 3	21-Jul-10	40	132/11	53.93
Transformer 4	09-Jul-10	40	132/11	51.70
Transformer 5	12-Aug-10	40	132/11	55.48
Transformer 6	16-Aug-10	40	132/11	54.34
Transformer 7	16-Aug-10	40	132/11	51.21
Transformer 8	26-Aug-10	40	132/11	53.73
Transformer 9	31-Aug-10	40	132/11	57.87
Transformer 10	31-Aug-10	40	132/11	56.09
Transformer 11	23-Nov-10	40	132/11	56.40
	Average			**53.42**

The test procedure for the measurement of load losses of the design unit is the same for the eleven transformers. The results presented in Table 6.1 show a large difference between the minimum and maximum measured stray losses. The minimum of 46.62 kW is recorded for Transformer 1. On the other hand, the maximum of 57.87 kW is obtained from Transformer 9. Comparing the two constitutes a difference of 11.25 kW. This difference is largely attributed to the manufacturing tolerances and processes, and handling of the magnetic material. It influences the potential conclusion that can be drawn, further presenting a challenge on understanding the real meaning of the results. Additionally, in pursuit of a hybrid method based on the statistical data and three-dimensional magnetostatic analysis of losses outside windings, [54] affirms that the additional losses of different units of the same design vary substantially. The excerpt obtained from the actual reports for the two extreme values are included in the appendix section.

The uncertainty observed in Table 6.1 indicates that the manufacturing aspects have a significant contribution to the interpretation of measured stray losses. To mitigate this influence, a decision to use the average of the tested transformers is taken. Hence, the winding eddy losses computed in Chapter 5 are compared later to 53.42 kW less the stray losses in structural parts. At this point the structural part loss component is unknown. In the next section the estimated individual components using three-dimensional finite element method tools are presented.

6.2. The results of the finite element method model

This section presents the result of the three-dimensional model simulated in Ansoft Maxwell using the eddy current solver. The geometry model of the 40MVA, 132/11kV transformer presented in Chapter 5 is prepared in the same manner. The construction geometry dimensions are the same as those provided in Appendix C. A similar process of conducting the simulation is repeated to determine the metal part losses in Maxwell. Similarly, the current magnitudes provided in Table 5.1 are impressed in the windings accordingly. The eddy current solver is configured so that the structural part components are set for eddy current calculations. The sub-sections below provide the simulation results of the tank, core clamps and flitch plates.

6.3.1. The tank losses

The surface impedance boundary modelling approach is used to calculate the losses in the tank. The method includes the assignment of boundary conditions on the transformer tank surfaces. In the definition of the surface impedance parameters, the relative permeability and conductivity of 200 and 6.67 MS/m are used respectively. Using Equation 3.20 in Chapter 3 yields a skin depth of 1.94 mm. The surface impedance modelling approach allows the reduction of the simulated tank surface thicknesses to be modelled as 1 mm sheets. This permits the omission of meshing the inside of the tank plates, placing more attention on the tank surfaces. In order to improve the integration error, the mesh operation in Maxwell that specifies the minimum number of elements is assigned on all tank surfaces. The surface loss density distribution achieved after the simulation is depicted in Figure 6.2, Figure 6.3 and Figure 6.4, which show the tank walls, cover and base respectively.

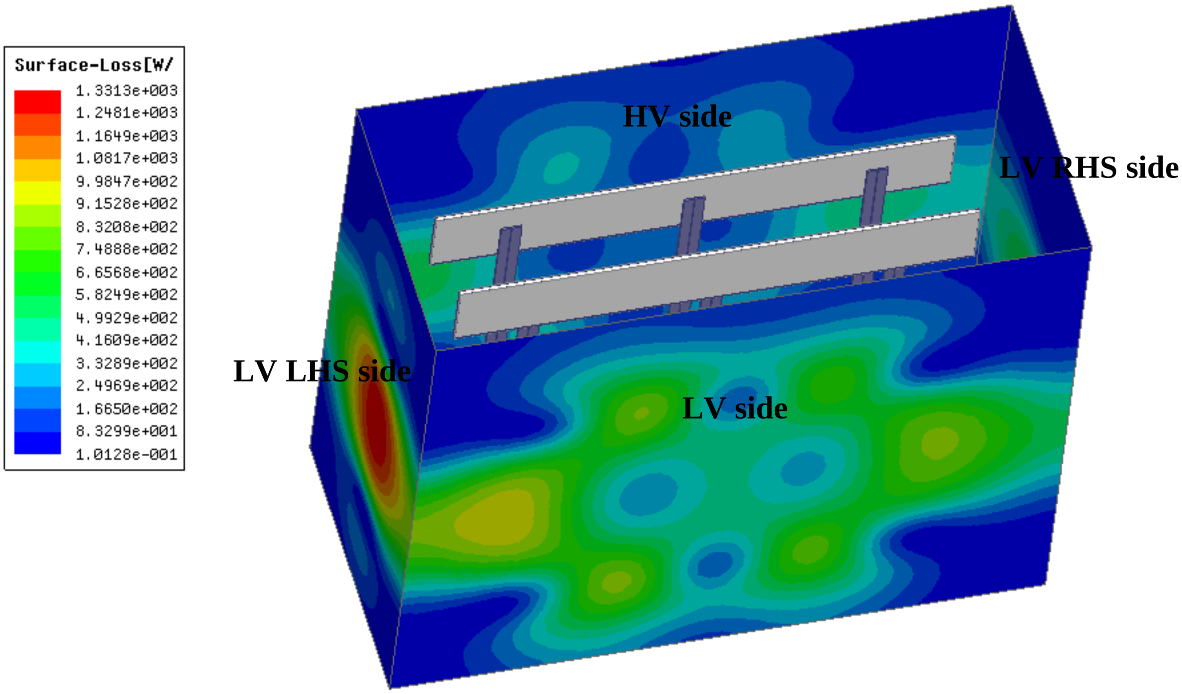

Figure 6.2: The leakage field on the tank walls

Figure 6.2 shows the distribution of the losses on the surfaces of the tank walls. It is clear from the figure that the loss density distribution profile is different for the four tank walls. The contour plot of the LV left hand side (LHS) shows a fairly high intensity and spherical distribution. This is mainly due to the short winding to tank distance. The other side, LV right hand side (RHS) does show a similar profile but with less loss distribution intensity. On this side, the tap changer is installed. Consequently the winding to tank distance is longer that the adjacent side. The magnetic distances directly affect the distribution of losses in structural parts. This phenomenon is also evident in the cover and base shown in Figure 6.3 and Figure 6.4.

The magnetic distance of the tank cover for this transformer is 205 mm, and the base is 30 mm, both are distances from the end of the core top and bottom respectively. It is discussed above that the magnetic distance influences the magnitude of the field intensity; hence the base has a higher loss density distribution than the cover. After plotting the contours of the loss distribution on the tank, the subsequent total losses experienced are calculated and presented in Table 6.2.

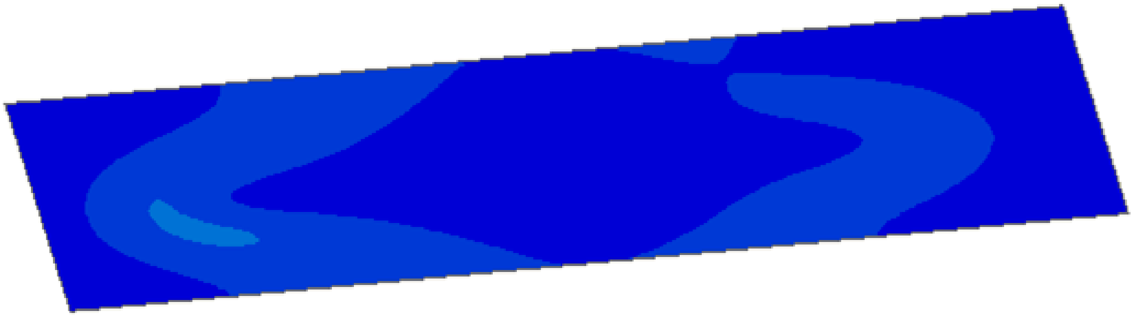

Figure 6.3: Loss distribution on the surface of the tank base plate

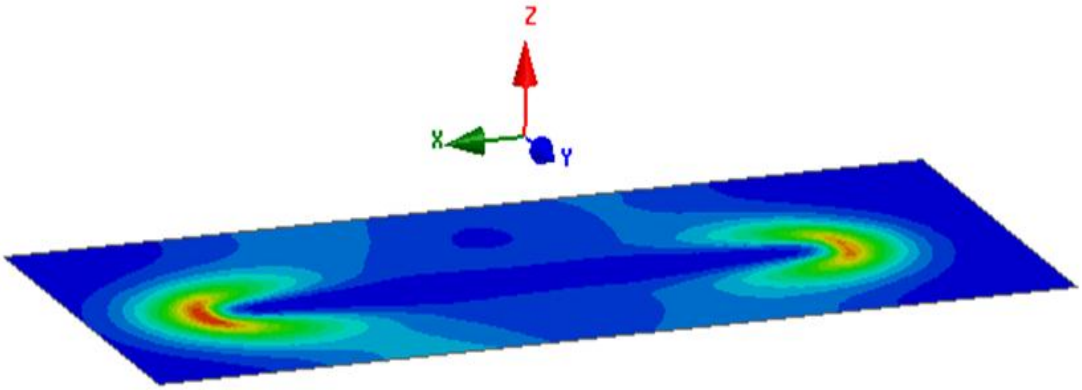

Figure 6.4: Loss distribution on the surface of the tank base plate

Using Equation 3.43 illustrated in Chapter 3, and integrating the losses of each surface element, the total losses of the tank are calculated. Moreover, this operation is embedded in the field calculator of Ansoft Maxwell. The user is only required to pass the surfaces under consideration and perform the surface integration. The numerical results obtained on the surfaces already shown above as contours are detailed in Table 6.2.

The transformer topology consists of four tank sides; traditionally the LV and HV sides are adjacent to the three phase winding configuration. While the LV RHS and LHS are adjacent to one winding. Therefore these sides experience different leakage fields. In Table 6.2 below this scenario is evident on the total losses of the surfaces.

Table 6.2: Tank wall, cover and base losses

Tank Walls	3-D FEM(W)	Constant linearization(W)
LV LHS tank losses	2069.35	2897.09
LV RHS tank losses	1039.91	1455.87
Cover	492.88	690.03
Base	1308.06	1831.29
LV tank losses	4532.10	6344.93
HV tank losses	2320.03	3248.04
Total Tank	11762.32	16467.25

The simulation results of the overall surface integration are presented in Table 6.2; they are obtained from the isotropic properties of the material as already indicated. The discussed surface impedance method is implemented on the boundary of the surfaces. It is mentioned earlier that [43] suggests a linearization factor varying from 1.1 to 1.4. Therefore the factor of 1.4 is conservatively chosen to multiply the simulation result of each side as per the last column. The simulation results of the core clamps and flitch plates are presented next.

6.3.2. Core clamp and flitch plate losses

The losses of the core clamps and flitch plates are obtained using a different approach to surface impedance modelling; the volumetric integration of the eddy current density uses Equation 3.35. The attributes of this methodology include the rigorous mesh requirements for obtaining the accurate results. To fulfil this requirement, the approach adopted is the multi-layer modelling approach with mesh operations. For core clamp loss calculations, two sheets of layers that lie within the material skin depth are literally created and assigned surface mesh operations to modify the mesh on each layer. The thickness of each core clamp is 30 mm also the transformer has four core clamps, two on both the LV and HV sides.

The multi-layer approach results in the increased amount of mesh elements of the main object, particularly within the skin depth. The convergences of the losses of the core clamps are monitored after each pass and the results are shown in Figure 6.5.

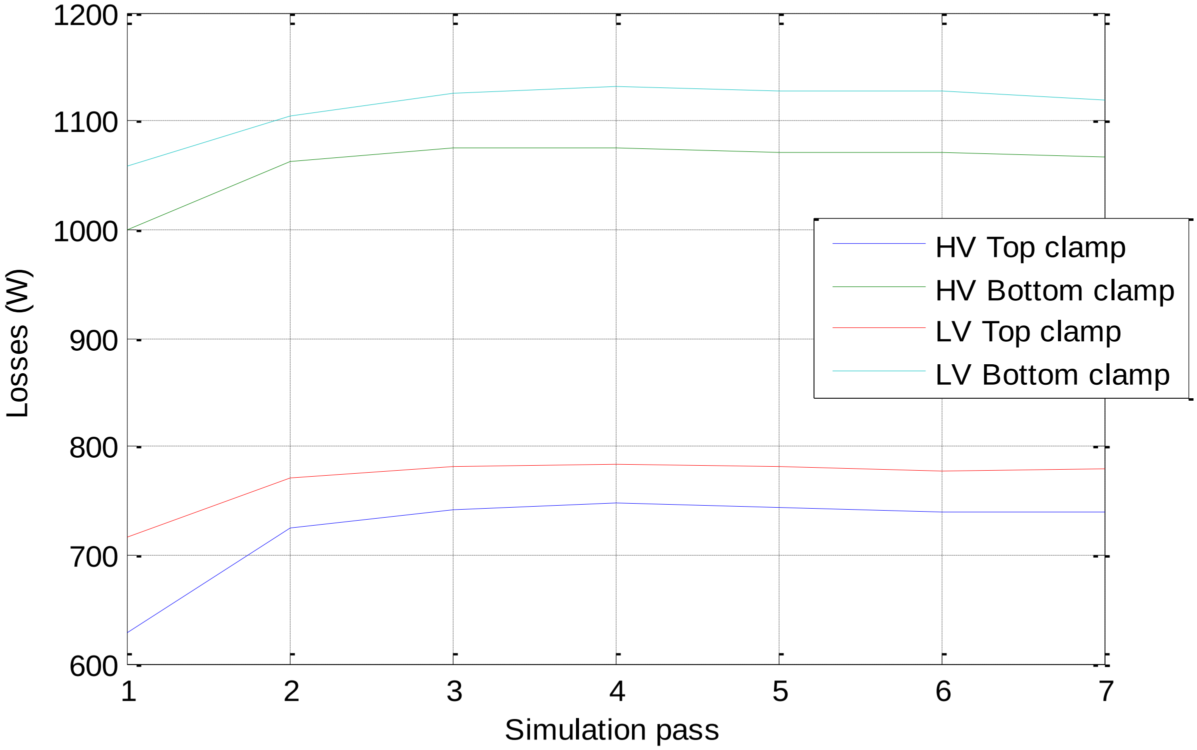

Figure 6.5: Core clamp convergence analysis

The convergence improvements are apparent in Figure 6.5, the losses of the four core clamps start converging after four passes. The losses of the bottom clamps, both the LV and HV sides are higher than their equivalent top clamps. This is due to the design philosophy which allows the use of the press ring only at the top. Hence the magnetic distance becomes larger, resulting in low losses.

Figure 6.6 shows the typical distribution of losses on the core clamp and flitch plate surfaces obtained from the simulation result sets. Confining the discussion to the core clamp losses for now, it is clear from Figure 6.6 that the loss density is higher on the surfaces adjacent to the side limbs. Again the overall losses are obtained using the formula for differential volumetric losses provided in Equation 3.35. The losses are recorded and presented in Table 6.3.

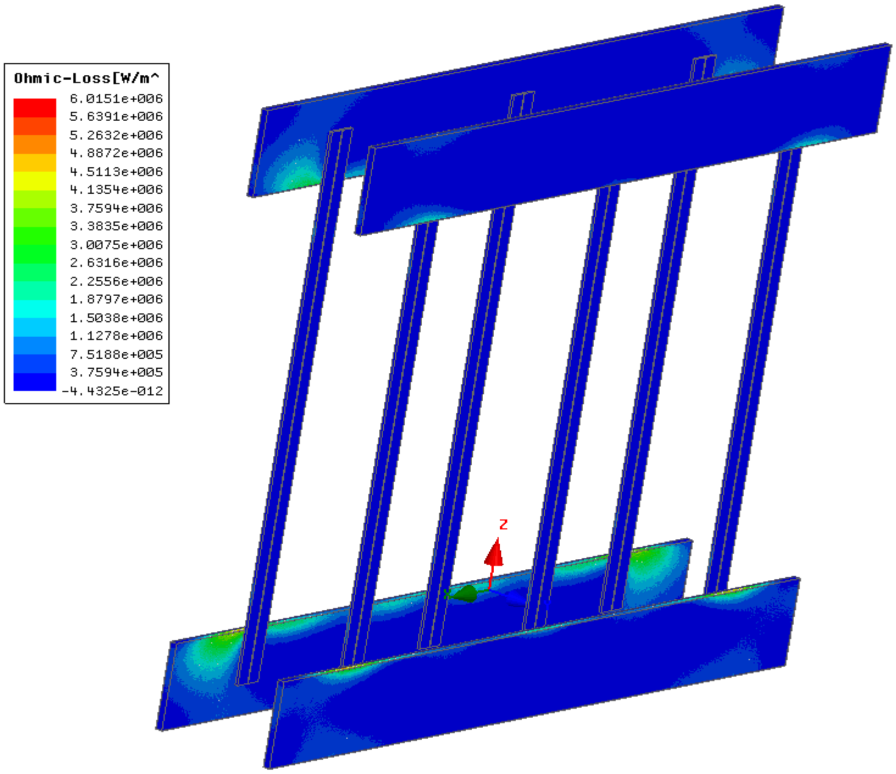

Figure 6.6: Loss density pattern in the core clamps and flitch plates

The losses of the core clamps are calculated using the field calculator of Ansoft Maxwell, the function used to perform this operation is predefined and readily available in the calculator. Since the linear properties are used, the losses are also multiplied by 1.4 shown on the last column of Table 6.3. In this table the clamps are denoted according to the voltage level (LV or HV) sides and their respective locations i.e. bottom or top.

Table 6.3: Core clamp simulation results

Clamps	3-D FEM(W)	Constant linearization (W)
HV Top	738.65	1034.10
HV Bottom	1066.35	1492.89
LV Top	778.41	1089.78
LV Bottom	1119.34	1567.07
Total Clamp	3702.75	5183.85

Shifting focus to the flitch plates, they are modelled using only the skin-depth meshing operation. This functionality is embedded in Ansoft Maxwell for the purpose of simulating materials with small skin depths. It is however not as effective as the method of creating the layers inside the material as discussed above in the case of the core clamp. Nonetheless, it is deemed sufficient for the eddy current losses induced in flitch plates as they are known to be fairly small. In addition, the analysed transformer has twelve flitch plates i.e. two on each side per limb. The simulated results obtained for all flitch plates are shown in Table 6.4 below.

Table 6.4: Flitch plate losses

Flitch Plates	3-D FEM(W)	Constant linearization(W)
HV34	29.7446	41.64
HV35	25.5892	35.8
HV26	19.3482	27.09
HV27	19.9797	27.97
HV30	26.0687	36.50
HV31	28.4958	39.89
LV36	27.4542	38.44
LV37	25.149	35.21
LV28	18.8177	26.34
LV29	20.1212	28.17
LV32	24.1471	33.81
LV33	29.2723	40.98
Total flitch plate	294.188	411.86

The results of the flitch plates are obtained in the same manner of integration as the core clamping structures. The naming that denotes each flitch plate uses the voltage level (LV or HV) and the object number in the simulation. It is seen that the losses of the plates lying on the HV side are slightly higher than those of the LV side. Furthermore, the total contribution in comparison to the tank and core clamp losses is relatively small. This is the main reason the intensive meshing techniques are not employed in these structures. In the next section the net results calculated so far are subtracted from the actual measured stray losses and a conclusion is drawn.

6.3. Measured winding eddy losses

The three-dimensional finite element method is used to calculate the losses in metal parts of the test transformer. These results are important in separating the measured stray losses, and in this section it is shown how they produce the measured winding eddy losses. The difference between the average measured stray losses of 53.42 kW from Table 6.1 and the sum of the calculated losses in metal parts is the measured winding eddy losses shown in Table 6.5. The results of the calculated winding eddy losses are also included in the table, they involve the following methodologies; 3-D FEM three-phase, 3-D FEM single-phase, 2-D FEM axisymmetric and in-service (Rabins' Method) program. The single-phase losses are multiplied by three to obtain the three-phase equivalent winding eddy losses.

Table 6.5: Calculated versus measured winding eddy losses

	Calculated				**Measured**
	3-D FEM 3-phase	**3-D FEM Phase B**	**2-D FEM**	**In-service program**	
Winding eddy losses	16781.88	16005.24	17243.91	17160	27166.04
Tank Wall	16467.25				
Core Clamp	5183.85				
Flitch Plate	411.86				
Outer core packet				3140	
High Current leads				1051	
Stray losses (W)	**43035.84**				**53424.55**

It should be noted that the structural part components calculated involved only the main structures. Hence, the losses due to the outer core packet and high current carrying leads should also be taken into account. However, these are not calculated here, they are obtained using the in-service program used by Powertech Transformers to evaluate losses. The losses depicted using the indigo colour are the final losses used for comparison. They take into account the nonlinearity as shown in the individual calculation of metal part losses. Therefore, 27.17 kW is the maximum measured winding eddy losses.

In comparing the losses above, the minimum percentage difference between any of the calculated to the measured winding eddy losses without the nonlinearity factor is 36.52%. However, the result considered accurate to predict winding eddy losses from Table 6.5 are those computed using 3-D FEM for the three-phase. They result in a percentage difference of 38.22% when compared with the measured winding eddy losses. Finally, before a conclusion is drawn it is of utmost importance to assess the worst case. This case is equivalent to the lowest measured stray losses in Table 6.1.

For a proper comparison of this worst case, the following conditions are presented; the nonlinearity factor has multiplied the losses and the additional loss components discussed above are included. The calculation of the new winding eddy losses is done and the new measured winding eddy losses become 20.37 kW. The percentage difference when compared with the three-phase, 3-D FEM result is 17.60%. It is clear that these measured winding eddy losses do not provide an adequate conclusion as the percentage difference is still larger than 10%, which exceeds the IEEE load loss acceptance criterion.

6.4. Conclusion

The difference between the calculated and measured stray losses has been methodically assessed. It is deduced that the results are inconclusive; the synthesis of stray losses based on calculating losses in metal parts does not work. The evaluation of stray losses in metal part components is dynamic and intricate, it further depends on manufacturing tolerances that are difficult to predict.

The standard deviation of the measured results shown in Table 6.1 is fairly large, and this effectively contributes to the complexity in achieving a coherent conclusion. The difference between the minimum and maximum measured stray losses of the same design can be as much as 68% of the calculated winding eddy losses.

The metal part losses should be estimated with the three-dimensional tools that account for the nonlinear behaviour of the magnetic steel structures. A different experimental approach is required to predict the measured winding eddy losses. Methods such as, variation of the power supply frequency and flux density measurements between windings should be considered.

Chapter 7

Conclusions and recommendations

7.1. Conclusion

a. Eddy currents

The rigorous evaluation of winding eddy losses has been performed using analytical and numerical methods. The accuracy of one-dimensional solution approach in rectangular coordinates is sufficient with limitations. The observed limitation with this method is that there is a large error when the conductor thickness is above 5mm. The radial winding eddy losses of a conductor depend on the solution discretization, the mid-flux density is not adequate to predict the radial winding eddy losses, and the calculation error could be as large as 74%. The use of the cylindrical coordinate solution is assessed to identify improvements and to limit the assumptions. This inherently took into account the curvature when deriving the eddy current theory. The solution of this approach proved to require large computational resources to evaluate mathematical expressions. This method is too intensive and impractical in transformer production environments.

b. Evaluation of leakage fields

The eddy current theory demonstrated that the evaluation of the leakage field components is a prerequisite to its completeness. The two-dimensional, analytical and numerical methods were investigated thoroughly, to accurately determine the local flux density quantities. Rabins' method was implemented in Mathematica. The method showed dynamic dependency on the number of the Fourier series terms and the number of digits of precision. When compared with FEM, FEM is found to be preferable, due to its robustness, flexibility and speed. The calibration of the axial flux density component is essential as the absolute values do not match. In terms of calculation time Rabins' method is much slower, on average FEM took 32 seconds while Rabins took up to 15 minutes. To improve on this time, lower level programming packages such as FORTRAN and C should be considered.

c. Core window effect

The influence of the core window effect to the evaluation of winding eddy losses was investigated. The two-dimensional methods are not able to take into account the core window effect. The three-dimensional models were simulated to assess the winding to core distance and the influence of the adjacent windings. The presence of the yokes is a function of winding to core yoke distance and mostly affects the radial winding eddy loss calculations. Due to the presence of the core, the radial losses of the innermost windings of the side limbs can easily be 32% higher than those of the centre limb winding. The influence of the adjacent windings can cause up to 27% higher radial winding eddy losses on the outer winding of the centre phase. The overall effect of the core window observed from comparing the two-dimensional results to three-dimensional results is 2%.

d. Practical result

The separation of the stray loss components through the determination of metal part losses is complex and gives inconclusive results. There is a large difference between calculated and measured winding eddy losses. The difference between the stray losses of the same unit can be as high as 68% of the winding eddy losses. The unit with the least stray losses from the series of the same unit test sample resulted in the difference of winding eddy losses of 18% between measured and calculated results. Hence, the calculation of the winding eddy losses using intensive methods is perhaps not necessary as the difference between the measured and calculated stray losses of the same unit undermines the benefits of the effort. In addition the detailed calculations may have immense benefits for winding hot-spot localizations.

7.2. Recommendations

For future considerations, from the studies of the evaluation of winding eddy losses the following recommendations are made:

- A study of the applicability of the eddy current analysis using cylindrical coordinates may still be expanded. To be able solve the complicated eddy current equations.
- The investigation of the core window effect is interesting and may be extended to yield the development of an analytical model that accounts for:
    - the winding to core yoke distance influence.
    - the influence of the adjacent windings.
- The evaluation of losses in metal parts is vast and needs an independent treatment where analytical models are compared with the three-dimensional method models.
- To improve the reliability of the calculation of metal part losses, the tools that account for the nonlinear behaviour of the magnetic steel structures should be the prerequisite.
- There is sufficient evidence from the skin depth formulation that the stray losses in metal parts and windings could be experimentally separated by varying the power frequency.
- The measurement of flux density between windings should be contemplated to improve the understanding of winding eddy losses.

References

[1]. *Power transformers-Part 1: General*, IEC 60076-1, April 2000.

[2]. *Power Transformers-Loading guide for oil-immersed power transformers,* IEC 60076-7, 2005, Pg. 47.

[3]. R.L. Stoll, "Numerical method of calculating eddy currents in nonmagnetic conductors," *Proc. IEE*, Vol. 114, No. 6, June 1967, pp. 775-780.

[4]. R.L. Stoll, "Approximate formula for the eddy-current loss induced in a long conductor of rectangular cross- section by a transverse magnetic field," *Proc. IEE*, Vol. 116, No. 6, June 1969, pp. 1003- 1008.

[5]. R. L. Stoll, *The analysis of Eddy Currents,* Oxford University Press, 1974, chapter 2.

[6]. A Rakotomalala et al, "A 2-D semi-analytical method for the calculation of eddy current losses in transformer and inductance coils," *Power Electronics and Variable-Speed Drives,* Conference publication No. 399, 26-28 October 1994.

[7]. A. Saley, A. Adly, T. Fawzi, A. Omar, and S. El-Debeiky, "Estimation and minimization techniques of eddy-current losses in transformer windings," *CIGRE 2002*, Paper No. 12-105.

[8]. Gulwadi, G.S., Ramachandran, R., and Bhatia, S., Kulkarni, S.V., "Accurate estimation of eddy loss in transformer windings by using FEM analysis," *International Conference on Transformers, TRAFOTECH-94,* Bangalore, India.

[9]. S.V. Kulkarni, S.A. Khaparde, *Transformer engineering: Design and Practice,* Marcel Dekker, Inc., 270 Madison Avenue, New York, NY 10016, U.S.A, 2007, Chapter 4.

[10]. R.S. Girgis, D.J. Scott, D.A. Yannucci, and J.B. Templeton, "Calculation of winding losses in shell form transformers for improved accuracy and reliability—Part I: Calculation procedure and program description," *IEEE Transactions on Power Delivery,* Vol. PWRD-2, No. 2, April 1987, pp. 398–410.

[11]. B. Baodong, X. Dexin, C. Jiefan, F. Zhenyao, "Optimal transposition design of transformer windings by genetic algorithms," *IEEE Transactions on Magnetics,* Vol. 31, No. 6, November 1995, pp. 3572-3574.

[12]. H.J. Kaul, "Stray current losses in stranded windings of transformers," *AIEE Transactions,* June 1957, pp. 137–149.

[13]. S. Isaka, T. Tokumasu, and K. Kondo, “Finite element analysis of eddy currents in transformer parallel conductors,” *IEEE Transactions on Power Apparatus and Systems*, Vol. PAS-104, No. 10, October 1985, pp. 2731–2737.

[14]. D.A. Koppikar, S.V. Kulkarni, G. Ghosh, S.M. Ainapure, and J.S. Bhavsar, “Circulating current loss in transformer windings,” *Proceedings IEE—Science*, Measurement and Technology, Vol. 145, No. 4, July 1998, pp. 136–140.

[15]. S.V. Kulkarni, S.A. Khaparde, “Stray loss evaluation in power transformers-A review,” *IEEE Power Engineering Society Winter Meeting*, Vol. 3, No. 10, 2000, pp. 2269–2274.

[16]. J. C. Olivares-Galván, P.S. Georgilakis, R Ocon-Valdez, “A Review of Transformer Losses,” *Electric Power Components and Systems*, 37: 9, pp. 1046 - 1062.

[17]. E. I. Amoiralis, M. A. Tsili, P. S. Georgilakis, “The state of the art in engineering methods for transformer design and optimization: a survey”, *Journal of Optoelectronics And Advanced Materials*, Vol. 10, No. 5, May 2008, pp. 1149 – 1158.

[18]. E. Schmidt, P. Hamberger, “Design optimization of power transformers. Part 2. Eddy current analyses for tank wall and core clamping parts,” *International Conference on Power System Technology - POWERCON 2004*, Singapore, November 2004,pp. 1375-1380.

[19]. L Susnjic, Z Haznadar, Z Valkovic, “3D finite-element determination of stray losses in power transformer,” *Electric Power Systems Research*, 78, 2008, pp.1814–1818.

[20]. L Kralj, D Miljavec, “Stray losses in power transformer tank walls and construction parts,” *XIX International Conference on Electrical Machines - ICEM 2010*, Rome.

[21]. Z. Valkovic, “Calculation of the losses in three-phase transformer tanks,” *Proceedings IEE.*, Vol. 127, Pt. C, No. 1, January 1980, pp. 20–25.

[22]. B. Szabados, I. El Nahas, N. S. El Sobki, R. D. Findlay, H. Poloujadoff, “A new approach to determine eddy current losses in the tank walls of a power transformer,” *IEEE Transactions on Power Delivery*, Vol. PWRD-2, No. 3, July 1987, pp. 810-816.

[23]. C. Guerin, G. Tanneau, G. Meunier, “3D Eddy Current Losses Calculation in Transformer Tanks Using the Finite Element Method,” *IEEE Transactions On Magnetics*, Vol. 29, No. 2, March 1993, pp. 1419-1422.

[24]. J. Turowski, A. Pelikant, “Eddy current losses and hot-spot evaluation in cover plates of power transformers,” *IEE Proc-Electr. Power Appl.,* Vol. 144, No. 6, November 1997, pp. 435-440.

[25]. D. Kim, S. Hahn, S. Kim, “Improved design of cover plate of power transformers for lower eddy current losses,” *IEEE Transactions on Magnetics*, Vol. 15. No. *5,* September 1999, pp. 3529-3531.

[26]. X. M. López-Fernández, P. Penabad-Durán and J.Turowski, “3-D Methodology for the Heating Hazard Assessment on Transformer Covers,” *XIX International Conference on Electrical Machines - ICEM 2010,* Rome.

[27]. Y. Junyou, T. Renyuan, L. Yan, “Eddy current fields and overheating problems due to heavy currents carrying conductor,” *IEEE Transactions On Magnetics,* Vol. 30, No. 5, September 1994, pp. 3064-3067.

[28]. S. Saito, K. Inagaki, T. Sato, Y. Inui, K. Okuyama, H. Otani, “Eddy currents in structure surrounding large currents bushing of a large capacity transformer,” *IEEE Transactions on Power Apparatus and Systems,* Vol. PAS-I00, No. 11, November 1981, pp. 4502-4509.

[29]. S.V. Kulkarni, J.C. Olivares, R. Escarela-Perez, V.K. Lakhiani and J. Turowski, “Evaluation of eddy current losses in the cover plates of distribution transformers,” *IEE Proc.-Sci. Meas. Technol*., Vol. 151, No. 5, September 2004, pp. 313-318.

[30]. E. Schmidt, P. Hamberger, W. Seitlinger, “Finite Element Calculation of Eddy Current Losses in the Tank Wall of Power Transformers,” *IEEE International Electric Machines and Drives Conference,* Vol. 2, 2003, pp. 1167 – 1173.

[31]. S.A. Holland, G.P. O'Connell, L. Haydock, “Calculating Stray Losses In Power Transformers Using Surface Impedance With Finite Elements,” *IEEE Transactions on Magnetics, Vol. 28, N0.2, March 1992,* pp. 1355-1358.

[32]. Z Janic, Z Valkovic and Z Stih, “Stray losses in Transformer Clamping Plate,” *unknown publisher.*

[33]. D. Žarko, Z. Maljković, S. Štefan, “Calculation of Losses in the Core Clamps of a Transformer Using 3-D Finite Element Method,” *unknown publisher.*

[34]. N. A. Kadir, “Clamping Plate Losses in Power Transformers,” *unknown publisher.*

[35]. D. A. Koppikar, *S.* V. Kulkarni, P. N. Srinivas, S. A. Khaparde, R Jain, "Evaluation of flitch plate losses in power transformers," *IEEE Transactions on Power Delivery*, Vol. 14, No. 3, July 1999, pp. 996-1001.

[36]. L. Lin, C Xiang, Z. Yuanlu, C. Zhiguang, Z. Guoqiang, Z.Yinhan, "Losses Calculation in Transformer Tie Plate Using the Finite Element Method," *IEEE Transactions on Magnetics*, Vol. 34, No. *5* , September 1998, pp. 3644-3647.

[37]. X Ma, Y. Jiang, "Study on Eddy Current Loss of Core Tie-plate in Power Transformers," *Asia-Pacific Power and Energy Engineering Conference (APPEEC)*, 2010, pp. 1-4.

[38]. D. K. Cheng, *Field and Wave Electromagnetics*, Addison-Wesley Publishing Company Inc., 2nd Edition, November 1992.

[39]. A.F Chalmers, "Maxwell's methodology and his application of it to electromagnetism," *Studies in History and Philosophy of Science Part A*, Volume 23, Issue1, March 1992, Pages 103-145.

[40]. G. James, *Advanced Modern Engineering Mathematics*, Pearson Education Limited, 3rd Edition, 2004, Pg. 557.

[41]. *IEEE Standard Definitions of Terms for Radio Wave Propagation*, IEEE Standard C211-1997, 1998.

[42]. W.S. Franklin, "Poynting's theorem and the equations of electromagnetic action," *Journal of the Franklin Institute*, Volume 173, Issue 1, January 1912, Pages 49-54.

[43]. R. M. Del Vecchio, B. Poulin, T. F. Pierre, D. M. Shah, R. Ahuja, *Transformer Design Principles - With Application to Core-Form Power Transformers*, CRC Press Taylor & Fransis Group, 2nd Edition, 2010, Chapter 14.

[44]. P Moon, D E Spencer, "The meaning of the vector Laplacian," *Journal of the Franklin Institute*, Volume 256, Issue 1, December 1953, Pages 551-558.

[45]. N. W. McLachlan, *Bessel Functions for Engineers,* 2nd Edition, Oxford University Press, 1955.

[46]. I. A. Stegun M. Abramowitz, *Handbook of Mathematical Functions,* in Dover Publications, New York, 1972.

[47]. B. Hague, *Electromagnetic problems in electrical Engineering*, Oxford University Press, London, 1929.

[48]. J. M Thomson, “Magnetic field in Transformers at low frequencies,” *Philosophical magazine*, Vol. 25, No. 1, June 1938, pp. 242-256.

[49]. L. Rabins, “Transformer Reactance Calculation with Digital Computers,” *AIEE Transactions,* vol. 75, pp. 261-7, 1956.

[50]. P Hammond, “ Roth’s method for the solution of boundary –value problems in electrical engineering,” *Proc IEE,* Vol 114, No. 12, December 1967, pp. 1969-1976.

[51]. E. Billing, “The calculation of the magnetic field of rectangular conductors in a closed slot, and its application to reactance of transformer windings,” *Proceedings of the IEE*, Vol. 98, No.1, 195, pp. 55-64.

[52]. A Boyajian, “Leakage reactance of Irregular Distributions of Transformer Windings by the Method of Double Fourier Series,” *Proc IEE,* Vol 114, No. 12, October 1954, pp. 1078-1086.

[53]. J. A. Edminister, *Electromagnetics,* Schaums’s outline series, McGraw-Hill, 2nd Edition, 1995, Chapter 8.

[54]. F. Kelemen, L. Strac, S. Berberovic, “ Estimation of Stray Losses Outside of Windings in Power Transformers Using Three Dimensional Static Magnetic Field Solution and Statistics,” *18th ICEM 2008*, Vilamoura , September 2008, pp. 1-3.

[55]. W. Randy, R.S Girgis, “Experimental verification of three-dimensional analysis of leakage magnetic fields in large power transformers,” *IEEE Transaction on Power Apparatus and Systems*, Vol. PAS-102, No 9, September 1983, pp. 3212-3217.

[56]. R.S. Girgis, D.J. Scott, D.A. Yannucci, and J.B. Templeton, “Calculation of winding losses in shell form transformers for improved accuracy and reliability—Part I: Calculation procedure and program description,” *IEEE Transactions on Power Delivery*, Vol. PWRD-2, No. 2, April 1987, pp. 398–410.

[57]. M. Waters, “The measurement and calculation of axial electromagnetic forces in concentric transformer windings,” *Proceedings of the IEE-Part II: Power Engineering*, Vol. 101, No 79, 1954, pp. 35-46.

[58]. L. Jänicke, A. Kost, “Error Estimation and Adaptive Mesh Generation in the 2D and 3D Finite Element Method,” *IEEE Transactions on Magnetics,* Vol. 32, No. 3, May 1996, pp. 1334-1337.

[59]. N.A.Golias, T.D.Tsiboukis, “Adaptive Refinement Strategies in Three Dimensions,” *IEEE Transactions on Magnetics*, Vol. 29, No. 2, March 1993, pp. 1886-1889.

[60]. *IEEE Standard Terminology for Power and Distribution Transformers*, IEEE Standard C57.12.80-2010, December 2010.

[61]. *IEEE Standard for general requirements for liquid –immersed distribution power and regulating transformers*, IEEE Standard C57.12.00-2010, September 2010.

[62]. *IEEE Guide for Transformer Loss Measurement*, IEEE Standard C57.123-2002, December 2002.

[63]. D. Rodger, P.J Leonard, H.C. Lai, P.C. Coles, “Finite Element Modelling of Thin Skin Depth Problems Using Magnetic Vector Potential,” *IEEE Transactions on Magnetics*, Vol. 33, No. 2, March 1997, pp.1299-1301.

[64]. C. Guérin, G. Meunier, “Surface Impedance for 3D Non-linear Eddy Current Problems-Application of Loss Computation in Transformers,” *IEEE Transactions on Magnetics*, Vol. 32, No.3, May 1996, pp. 808-811.

[65]. C. Guérin and G. Tanneau, G. Meunier and P. Labie, T. Ngnegueu, M. Sacotte, “A Shell Element For Computing 3D Eddy Currents - Application to Transformers,” *IEEE Transactions on Magnetics*, Vol. 31, No. 3, May 1995, pp. 1360-1363.

[66]. N. Mahomed, M. Hlatshwayo, I. Hofsajer, “Critical Analysis of Rabins’ Magnetic Field Calculation Method,” *Saupec*, Discussion Paper, July 2011.

Appendix A

Single conductor analysis

Simulation model

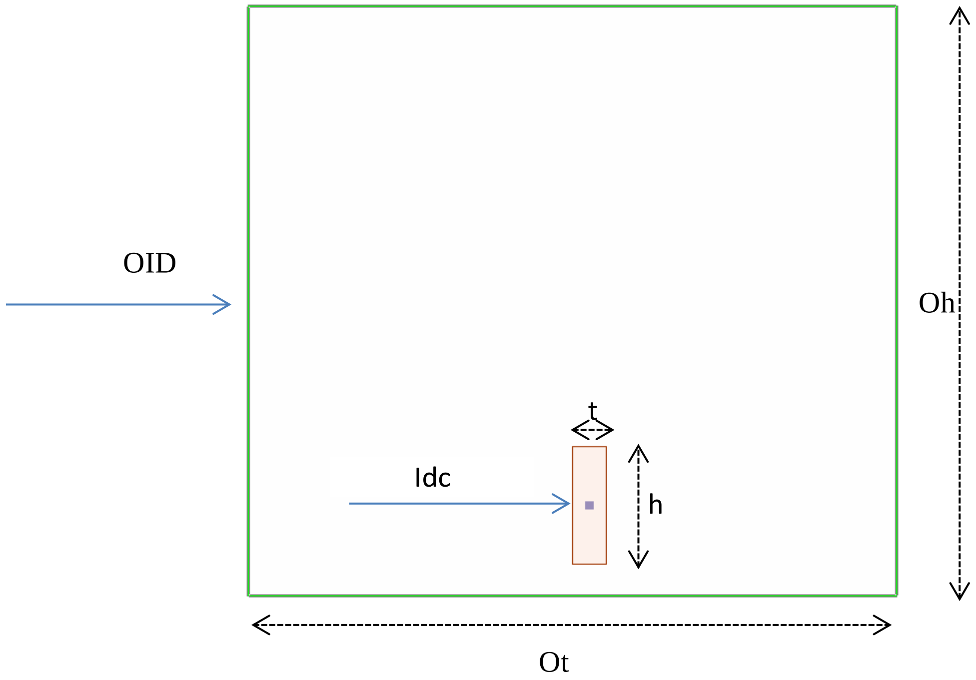

OID	Ot	Oh	t	h	Idc	Odc	Centroid
417.5	52	50.5	2	10.1	443.85	445.85	444.85
			2.3	10.1	443.70	446	444.85
			2.5	10.1	443.60	446.1	444.85
			2.7	10.1	443.50	446.2	444.85
			3	10.1	443.35	446.35	444.85
			4	10.1	442.85	446.85	444.85
			7	10.1	441.35	448.35	444.85
			10	10.1	439.85	449.85	444.85

Note: All dimensions are in mm

Single conductor model mesh

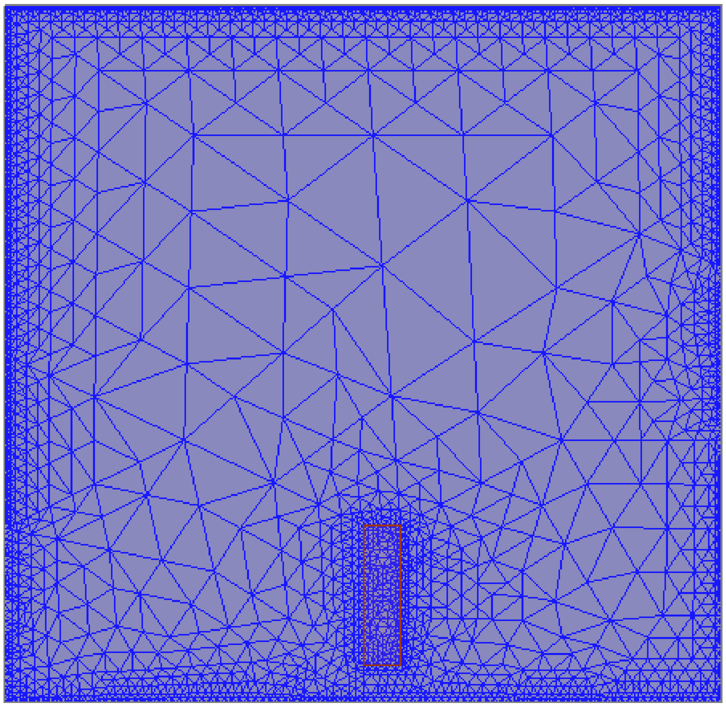

Boundary condition assignment

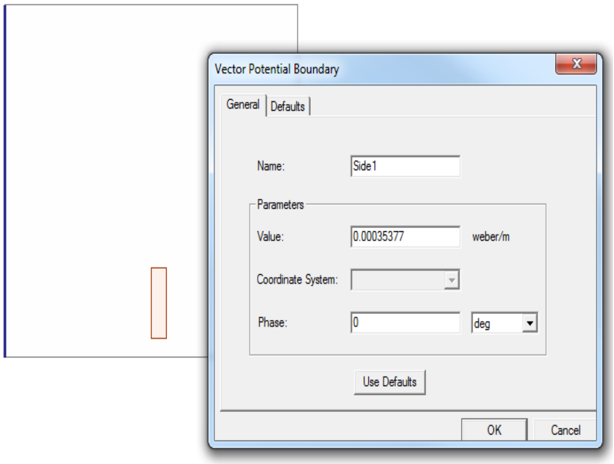

Name: Side1

Parameters

Value: 0.00035377 weber/m

Coordinate System:

Phase: 0 deg

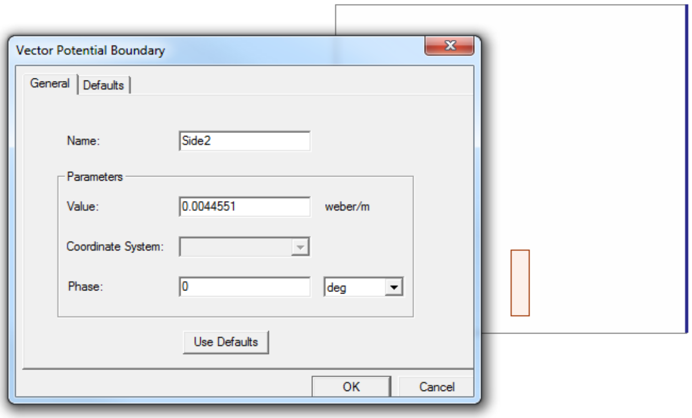
Vector Potential Boundary

Name: Side2

Value: 0.0044551 weber/m

Coordinate System:

Phase: 0 deg

Results: Field distribution

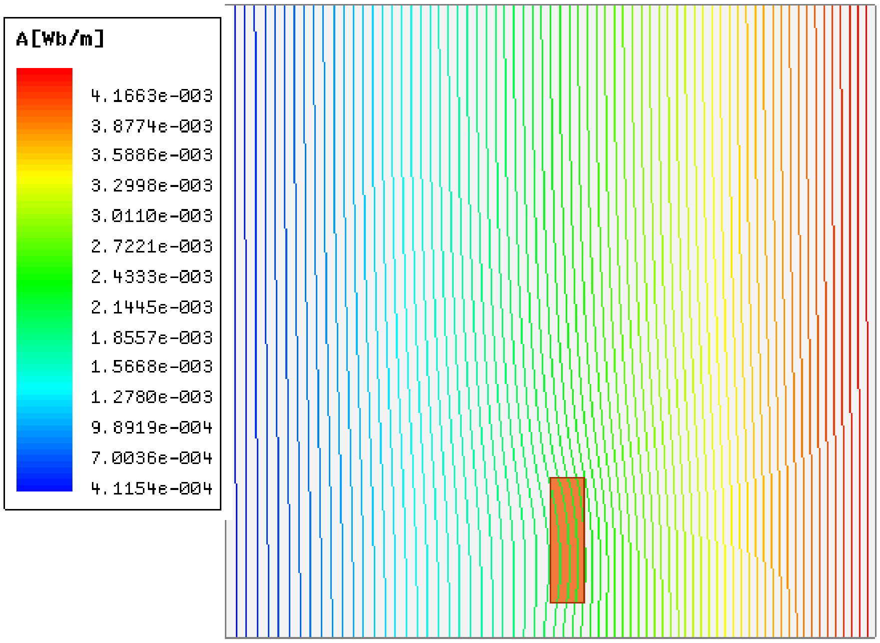

Results: Current distribution

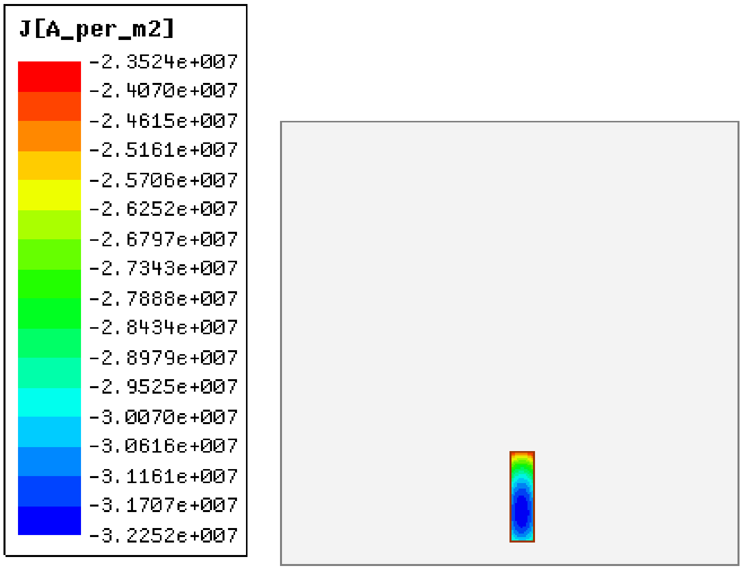

Appendix B

Transformer geometry of the 105MVA transformer

- Power: 105MVA
- Voltage: 330/11kV
- Connection: YNd1
- Winding arrangement: LV and HV

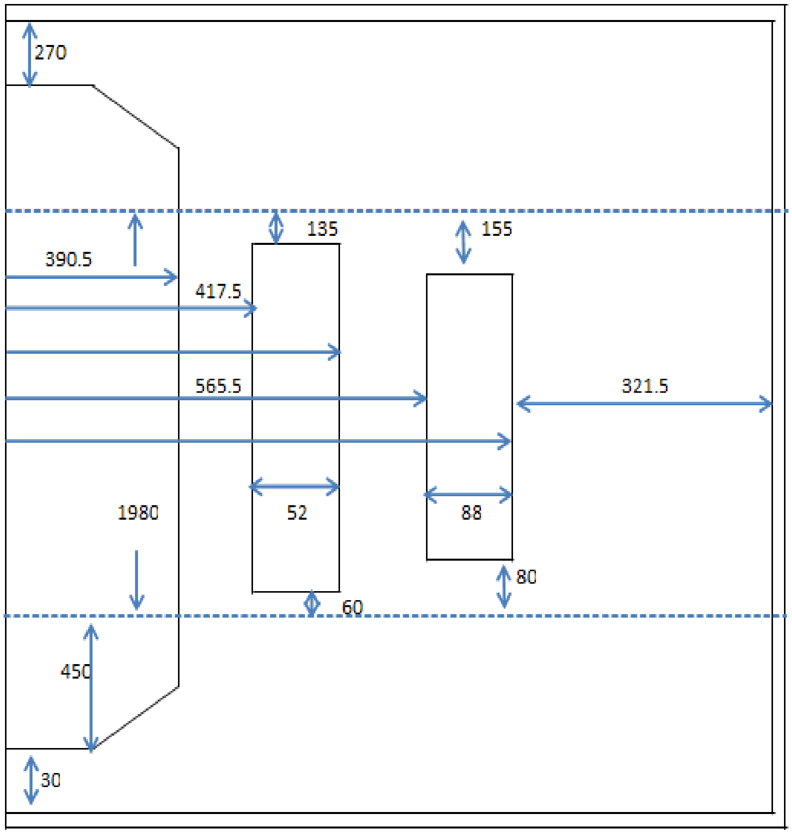

Table A 4.14: Transformer loading data

	LV	HV(Centre entry)
Connected Turns	63	1160
Current (A)	-3180	91.85

```
(*Common data*)
NDP =40;
nmax=70;
L=Rationalize[1.98];
mu=Rationalize[4*Pi*10^-7];
p=Rationalize[Pi ];
m=n*p/L;
z1=Rationalize[0.0405];
z2=Rationalize[1864.5/1000];
z=Rationalize[Import["J:\\MSc Studies\\Masters doc\\Dissertation\\Regular submissions\\Chapter
4\\Unreviewed\\Material\\Zcoordinate.xlsx"]];
(*Winding A*)
J1=Rationalize[-3.502*10^6];
rc=Rationalize[0.3905];
r1=Rationalize[0.4175];
r2=Rationalize[0.4695];
r=Rationalize[(r1+r2)/2];
```

```
x1=Rationalize[m*r1];
x2=Rationalize[m*r2];
xc=Rationalize[m*rc];
Joa=Rationalize[J1*(z2-z1)/L ];
Jn1 =Rationalize[2*J1/m*(Sin[m*z2*180/Pi Degree]-Sin[m*z1*180/Pi Degree]) ];

(*Computation of constants for B*)
En =Rationalize[Integrate[t*BesselK[1,t],{t,0,x2}]];
Kn=Rationalize[BesselI[1,xc]/BesselK[1,xc]];
K1x1x2= Rationalize[Integrate[t*BesselK[1,t],{t,x1,x2}]];
I1x1=Rationalize[Integrate[t*BesselI[1,t],{t,0,x1}] ];
Fn=Rationalize[Kn*K1x1x2-I1x1];

(*Winding B*)
J2=Rationalize[3.502*10^6];
r3=Rationalize[0.5655];
r4 =Rationalize[0.6535];
x3=Rationalize[m*r3];
x4=Rationalize[m*r4];
(*Computation of constants for B*)
Cn=Rationalize[Integrate[t*BesselK[1,t],{t,x3,x4}]];
Dn=Rationalize[Kn*Cn ];
Job=Rationalize[J2*(z2-z1)/L ];
Jn2 =Rationalize[2*J2/m*(Sin[m*z2*180/Pi Degree]-Sin[m*z1*180/Pi Degree])];

Brr= N[mu*Sum[1/m*(Jn1*(En*BesselI[1,m*r] + Fn*BesselK[1, m*r] - (Pi/2)*StruveL[1,
m*r])+Jn2*(Cn*BesselI[1,m*r] + Dn*BesselK[1, m*r] ))* Sin[m*z*(180/Pi)*Degree],{n,1,nmax}],NDP ];
Brr//TableForm;

Export["J:\\MSc Studies\\Masters doc\\Dissertation\\Regular submissions\\Chapter
4\\Unreviewed\\Material\\Brr.xls",Brr,"XLS"];
Bzz=N[mu*Joa*(r2-r)+mu*Sum[1/m(Jn1*(En*BesselI[0,m*r] - Fn*BesselK[0, m*r] - (Pi/2)*StruveL[0,
m*r])+Jn2*(Cn*BesselI[0,m*r] - Dn*BesselK[0, m*r] ))* Cos[m*z*(180/Pi)*Degree],{n,1,nmax}],NDP ];

Bzz//TableForm;
Export["J:\\MSc Studies\\Masters doc\\Dissertation\\Regular submissions\\Chapter
4\\Unreviewed\\Material\\Bzz.xls",Bzz,"XLS"];
```

Appendix C

Geometry Modelling Data of the 40 MVA, 132/11kV transformer

Item	Dimension(mm)
Core diameter	506
Limb height	1808
Yoke height	480
WA BYDistance	80
WB BYDistance	120
WC BYDistance	121
WA InnerDiameter	545
WA RadialW	73
WindingA Height	1602
WB InnerDiameter	747
WB RadialW	15
WindingB Height	1522
WC InnerDiameter	857
WC RadialW	93
WindingC Height	1520
Limb pitch	1102
RHS LV side	451
LHS LV side	248
Half yoke length	1564.5
Clamp thickness	30
Core clamp	15
Clamp height	390
BY Centre	-240
TY Centre	2048
Core cover	205
Core base	30
LV tank	285
HV tank	444
Flitch plate width	60
Core to flitch	1
Flitch thickness	12
Flitch plate to flitch plate	4
Centre to flitch plate	2

Winding design data of the 40MVA, 132/11kV transformer

	Space factor	*h* (mm)	WH(mm)	RW(mm)	*t* (mm)	n_r	n_a
Winding A	0.4794	6.2	1602	73	2.4	24	163
Winding B	0.522	5.25	1522	15	1.6	6	224
Winding C	0.4832	10.8	1520	93	2	33	98

Example: Maxwell field calculator

Implementation of the calculation of winding eddy losses using Equation (5.1)

```
Scl : 95.2449557686371

Scl : *(*(*(Integrate(Volume(PCW1), Pow(Br, 2)), 3.844E-005), 0.4794), k)

Scl : 83.9546747922373

Scl : *(*(*(Integrate(Volume(PBW1), Pow(Br, 2)), 3.844E-005), 0.4794), k)

Scl : 355.949294055326

Scl : *(*(*(Integrate(Volume(PAW1), Pow(Br, 2)), 3.844E-005), 0.4794), k)
```

Appendix D

Load loss test reports

Transformer 1 of Table 6.1

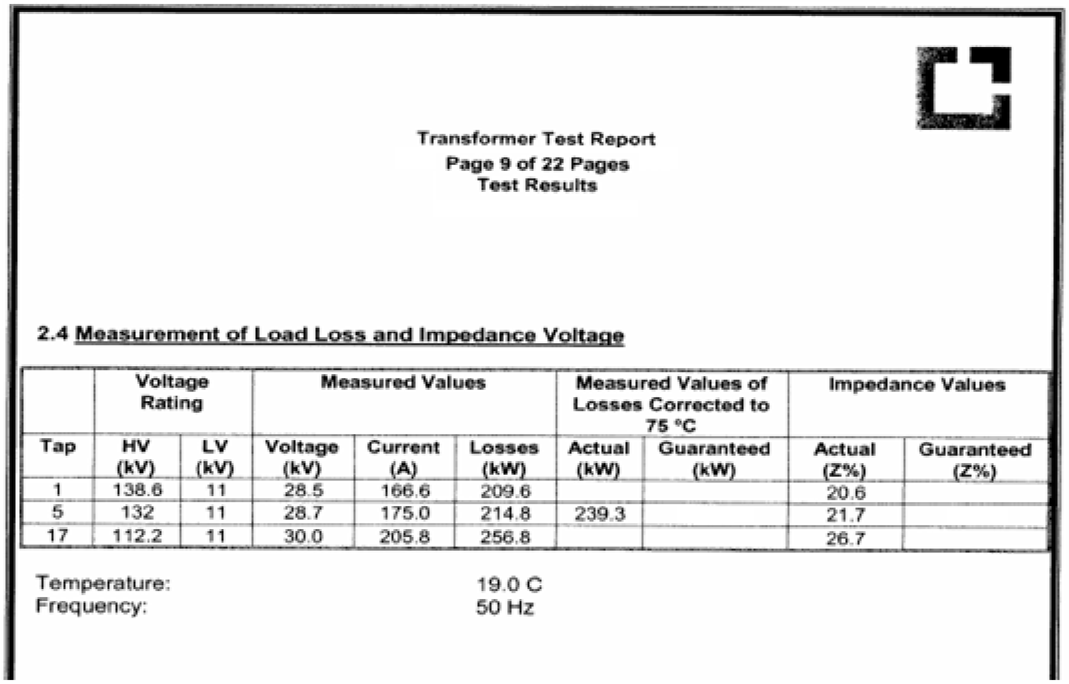

Transformer Test Report
Page 9 of 22 Pages
Test Results

2.4 Measurement of Load Loss and Impedance Voltage

	Voltage Rating		Measured Values			Measured Values of Losses Corrected to 75 °C		Impedance Values	
Tap	HV (kV)	LV (kV)	Voltage (kV)	Current (A)	Losses (kW)	Actual (kW)	Guaranteed (kW)	Actual (Z%)	Guaranteed (Z%)
1	138.6	11	28.5	166.6	209.6			20.6	
5	132	11	28.7	175.0	214.8	239.3		21.7	
17	112.2	11	30.0	205.8	256.8			26.7	

Temperature: 19.0 C
Frequency: 50 Hz

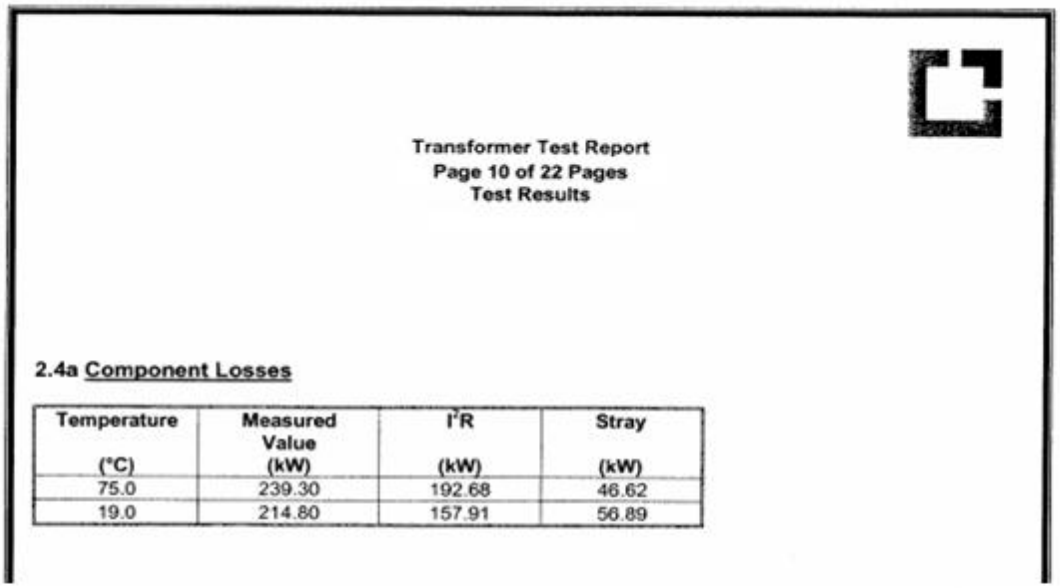

Transformer Test Report
Page 10 of 22 Pages
Test Results

2.4a Component Losses

Temperature (°C)	Measured Value (kW)	I^2R (kW)	Stray (kW)
75.0	239.30	192.68	46.62
19.0	214.80	157.91	56.89

Courtesy of Powertech Transformers

Transformer 9 of Table 6.1

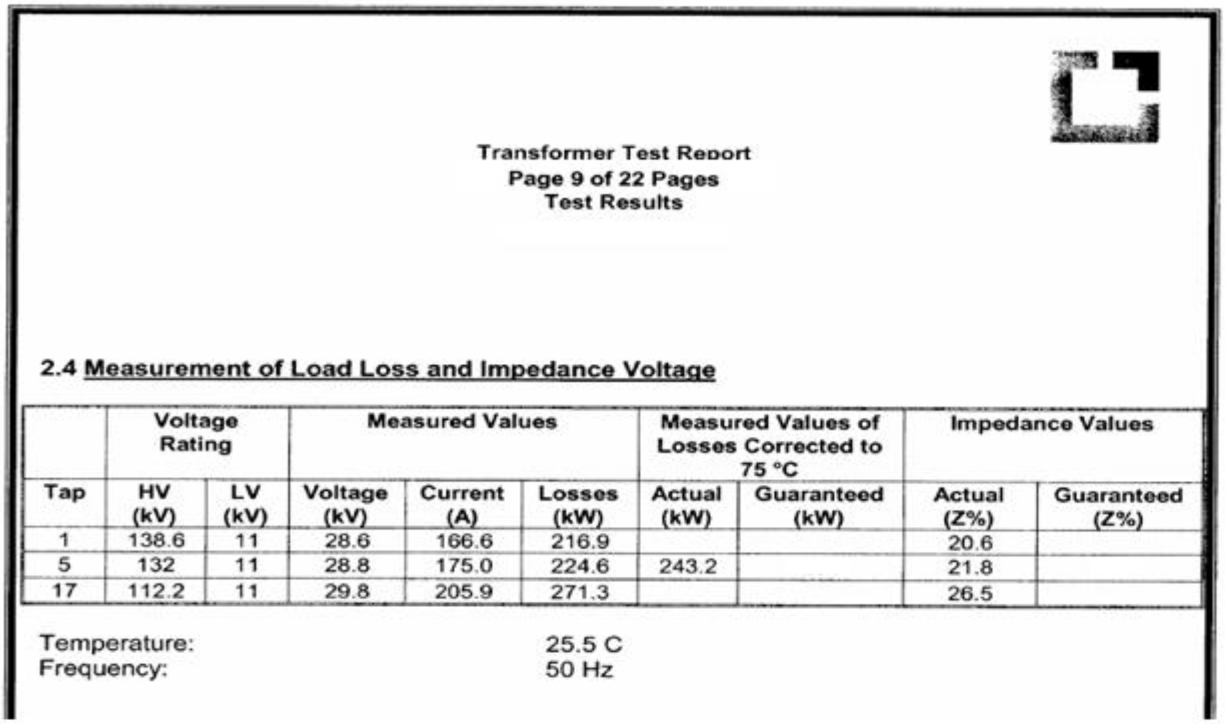

Transformer Test Report
Page 9 of 22 Pages
Test Results

2.4 Measurement of Load Loss and Impedance Voltage

	Voltage Rating		Measured Values			Measured Values of Losses Corrected to 75 °C		Impedance Values	
Tap	HV (kV)	LV (kV)	Voltage (kV)	Current (A)	Losses (kW)	Actual (kW)	Guaranteed (kW)	Actual (Z%)	Guaranteed (Z%)
1	138.6	11	28.6	166.6	216.9			20.6	
5	132	11	28.8	175.0	224.6	243.2		21.8	
17	112.2	11	29.8	205.9	271.3			26.5	

Temperature: 25.5 C
Frequency: 50 Hz

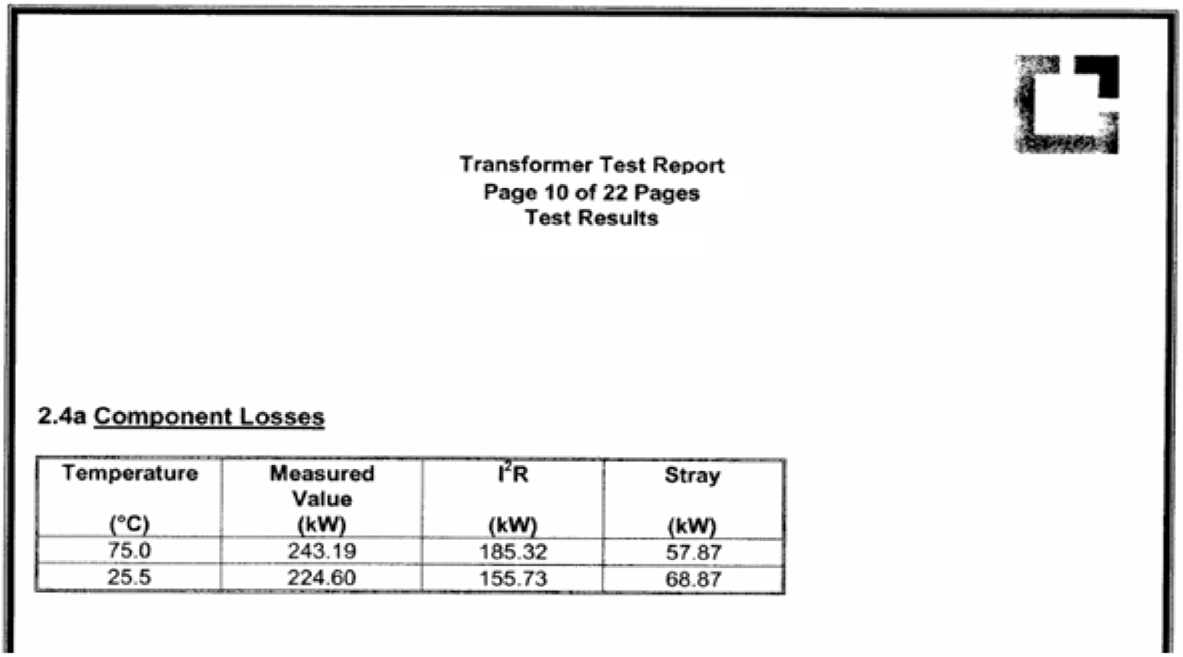

Transformer Test Report
Page 10 of 22 Pages
Test Results

2.4a Component Losses

Temperature (°C)	Measured Value (kW)	I^2R (kW)	Stray (kW)
75.0	243.19	185.32	57.87
25.5	224.60	155.73	68.87

Courtesy of Powertech Transformers